AGN FUELLING: BRIDGING LARGE AND SMALL SCALES

OVERLAPPING INFLOWS AS CATALYSTS OF ACCRETION

Juan Manuel Carmona-Loaiza

Doctor Philosophiæ(Ph.D.)
Astrophysics Sector
SISSA | Scuola Internazionale Superiore di Studi Avanzati

26th of May, 2015

Juan Manuel Carmona-Loaiza:
AGN fuelling: Bridging large and small scales – Overlapping inflows as catalysts of accretion.

SUPERVISORS:
Riccardo Valdarnini, Monica Colpi & Massimo Dotti

SISSA | Scuola Internazionale Superiore di Studi Avanzati,
Trieste, Italy; 26th of May, 2015

To Sebastián
and Valentina.

ABSTRACT

One of the biggest challenges in understanding the fuelling of supermassive black holes in active galactic nuclei (AGN) is not on accounting for the source of fuel, as a galaxy can comfortably supply the required mass budget, but on its actual delivery. While a clear picture has been developed for the large scale ($\sim$ kpc) down to the intermediate one ($\lesssim 100$ pc), and for the smallest scales ($\lesssim 0.1$ pc) where an accretion disc likely forms, a bridge that has proven difficult to build is that between ~ 100 pc and ~ 0.1 pc. It is feared that gas at these scales might still retain enough angular momentum and settle into a larger scale disc with very low or no inflow to form or replenish the inner accretion disc (on ~ 0.01 pc scales). In this Thesis, we present numerical simulations in which a rotating gaseous shell flows towards a SMBH because of its lack of rotational support. As inflow proceeds, gas from the shell impacts an already present nuclear ($\sim$ 10pc) disc. The cancellation of angular momentum and redistribution of gas, due to the misalignment between the angular momentum of the shell and that of the disc, is studied in this scenario. The underlying hypothesis is that even if *transport* of angular momentum at these scales may be inefficient, the interaction of an inflow with a nuclear disc would still provide a mechanism to bring mass inwards because of the *cancellation* of angular momentum. We quantify the amount of gas such a cancellation would bring to the central parsec under different circumstances: Co- and counter-rotation between the disc and the shell and the presence or absence of an initial turbulent kick; we also discuss the impact of self gravity in our simulations. The scenario we study is highly idealized and designed to capture the specific outcomes produced by the mechanism proposed. We find that angular momentum cancellation and redistribution via hydrodynamical shocks leads to sub-pc inflows enhanced by more than 2-3 orders of magnitude. In all of our simulations, the gas inflow rate across the inner parsec is higher than in the absence of the interaction. Gas mixing changes the orientation of the nuclear disc as the interaction proceeds until warped discs or nested misaligned rings form as relic structures. The amount of inflow depends mainly on the spin orientation of the shell relative to the disc, while the relic warped disc structure depends mostly on the turbulent kick given to the gaseous shell in the initial conditions.

The main conclusion of this Thesis is that actual cancellation of angular momentum within galactic nuclei can have a significant impact on feeding super massive black holes. Such cancellation by inflow-disc interactions would leave warped $10-20$ pc discs as remnants.

And if you listen very hard
The tune will come to you at last.
When all are one and one is all
To be a rock and not to roll.

–J. Page and R. Plant

GRAZIE

I must say that I am a lucky person, there is no doubt about that. If I were a religious person I would be thanking, first of all, some random god of some random religion for letting me joyfully live and complete the work you have in your hands or in the screen of some electronic device. Is it unfortunate, then, that I am not a religious person because then I lack an entity to whom express the thankfulness I feel? On the contrary, as I see it, not being a religious person allows me to appreciate what people around myself has actually done for the development of this work, directly or indirectly, without attributing their actions to the mystical machinery of some incomprehensible entity.

There are three people that substantially contributed to the development of this Thesis. The first person that must be acknowledged and to whom I am deeply grateful, not just for all the things I learned from her, but also for the immense patience she demonstrated at my mistakes during these years, is my dear PhD supervisor Monica Colpi, a real mentor. My knowledge of astrophysics was dramatically enriched by her. I'm also thankful to Riccardo Valdarnini for introducing me to the world of Turbulence, Fast Fourier Transforms (of the West), Parallel Programming, super-computers, and some other computer secrets and Fourier analysis I didn't know about. To complete the *trio*, the last person to whom I am grateful for the substantial impact he made on the quality of this Thesis, is Massimo Dotti. He was always ready to listen and read carefully the ideas I proposed. Most of the times, he would confute them with very simple arguments, pointing me afterwards to very interesting readings. Once in a while, the ideas I proposed seemed interesting to him, he would then suggest precise ways to test their validity, *just the way of science*.

I am also thankful to John Miller, who, from the time of my arrival to Trieste took care of helping me finding the best PhD thesis project for me. From then on he remained closely following the development of my work, reading carefully my manuscripts and making enlightening comments.

There's another *trio* to which I must express my gratitude. Giuseppe Murante, Laura Silva and Pierluigi Monaco: three really passionate scientists who shared that passion with me during times in which

mine was not at the top. Taking lunch and coffee together with them was always like reading a good book. On top of that, during times of very tough technical problems with GADGET, Giuseppe shared with me patiently his vast experience and knowledge, helping me out of any trouble.

As a PhD student I was usually not asking questions to the *grown-ups*, fearing they would find out how ignorant I am. Fortunately there were Sandra Raimundo, Emilio Tejeda, Alessandro Lupi and Xiaoting Fu: colleagues around my *academic-age* who were so happy to discuss science, and not only that, but they really knew *a whole lotta stuff* and shared their time with me.

During my PhD I also acquired some experience in communicating, experience that for sure had an impact on the final form of this Thesis and the way it is written. Thanks to Simona Cerrato and SISSA medialab for putting me on the front lines whenever there were *outsiders* wanting to know about science and what people like me were doing in SISSA.

Such a smooth development of things was certainly possible due to the efforts made by all SISSA staff. As an example, during my PhD, I often heard people in Trieste saying: "SISSA is not Italy". I am sure that two of the people to *blame* for this saying is Riccardo Iancer and Federica Tuniz. Bureaucracy was basically non-existent for me thanks to them. If you have lived in Italy, you surely understand what a help they and all SISSA-Staff were!

And finally we arrive to them. I don't know if one day we, intelligent beings with the ability of introspection and the awareness of being embedded in an external universe, will be able to develop artificial beings able to make decisions and logical deductions. Such beings would certainly be able to answer in a systematic way questions posed by us, humans. In that scenario, the yearn for posing questions is what would ultimately distinguish us from them, but, where does this yearn comes from in the first place? For me at least, it comes from interacting with other people like me that I call friends. More precisely when, in the middle of a conversation, you realise that there is something that no one knows and you still would like to know. I want to thank my friends Diana Carmona-Loaiza (my sister), Emilio Tejeda, Yabebal Tadesse-Fantaye, Iga Nowak and Angus Prain, Silvia Pozzetto, Airam Marcos-Caballero, Valentina Stocca, Eli, Isidro Munive, Andrés Hernández, Maria D'Errico and Elena Xerxa for stimulating my brain with interesting conversations, following my constant digressions and laughing at me whenever they found loopholes in my arguments. I want to thank them for being there with me, giving a lot of sense to the nonsense of posing questions, inherent to the human condition.

All of this work, however, would not have been possible at all, not even my arrival to Trieste, hadn't my parents been always supporting me all along my life. Gracias a mis padres, Carina y Juan Manuel, a su apoyo y a su búsqueda de responder las preguntas que hacía desde pequeño, y a la presión que ejercieron en su debido momento para que tomara un libro entre mis manos –cualquier libro, y lo leyera, es que descubrí la pasión por conocer más y por formular y responder preguntas, i.e. por hacer ciencia.

This section would not be complete if I didn't mention Antonella, *Kiffel*. Her generous help during these last months allowed me to forget about everything else and focus just on the writing. *Graciaskiffel! te son stada ssai coccola!*

I have left the warmest thank you of all for the last. I'm infinitely proud and joyful of having shared this experience with Valentina and Sebastián, the binary system that keeps me alive and that gave me all the thrust I needed during the writing. Sometimes I wonder, because I do wonder a lot about a lot of things, if this Thesis would be richer had they were not in my life these last year(s). Then I remember how life was without them, and the answer rises as an absolute and undeniable truth: "No".

Juan Manuel Carmona-Loaiza
Trieste, Italia - 4th of June of 2015

CONTENTS

Part I

INTRODUCTION

1

AGN FEEDING: SMBH GROWTH AND THE ANGULAR MOMENTUM BARRIER

According to the black hole paradigm, Active Galactic Nuclei (AGN) host super massive black holes accreting gas from their surroundings. Observations indicate that these black holes have grown over cosmic time mostly by radiative efficient accretion around $z \sim 3$ (Marconi et al. 2004; Merloni 2004), and that some of them were able to grow even faster, as revealed by the recent observations of $\gtrsim 10^9 M_\odot$ black holes at $z \sim 6-7$ (see, e.g. Mortlock et al. 2011). The tight correlation between the black hole mass M_{BH} and the stellar velocity dispersion σ of the galaxy's host, observed in the local universe, further indicates that the accretion history of black holes is closely linked with the evolution of the galaxies which they inhabit (Ferrarese & Ford 2005). Understanding super massive black hole (SMBH) accretion, from galactic scales down to the vicinity of the horizon of SMBHs, is therefore critical in understanding and inferring the origin of the SMBH population and for determining their relation with the evolution of their hosts galaxies across cosmic ages (Soltan 1982; Salucci et al. 1999; Ferrarese & Merritt 2000; Gebhardt et al. 2000; Shankar et al. 2004; Hopkins et al. 2006b; Kormendy & Ho 2013).

1.1 THE CENTRAL ENGINE OF ACTIVE GALACTIC NUCLEI

Active galactic nuclei are among the most interesting objects for modern astrophysics. Seyfert (1943) was the first to notice this kind of objects by studying 6 galaxies characterized by a bright stellar-like nucleus (as bright as the whole galaxy in some cases), blue, and presenting all broad emission lines, some being of high excitation. He attributed the widths of the lines to Doppler motions, which could be as high as $8500\,\mathrm{km\,s^{-1}}$, but it was not until the discovery of quasars (Hazard et al. 1963; Schmidt 1963; Oke 1963; Greenstein 1963; Sandage 1965) that the systematic study of AGN begun.

It is now widely accepted that the central engine of these sources are super massive black holes (SMBH;Salpeter 1964; Zel'dovich 1965; Lynden-Bell 1969; Rees 1978) with masses around $10^{6-10} M_\odot$. The observed luminosity in this picture is produced by accretion of gas surrounding the SMBH in a disc. Within this disc, the gravitational energy of the gas is converted into heat and radiation with an efficiency corresponding to $\varepsilon \dot{m} c^2 \simeq 0.05 - 0.42 \dot{m} c^2$, depending on the spin of the black hole; e.g. Shapiro & Teukolsky 1983). A huge amount

of energy can thus be liberated during accretion, yielding large luminosities from comparatively modest mass-accretion rates:

$$L_{bol} = \left(\frac{\dot{M}_{BH}}{0.15\,M_\odot\,yr^{-1}}\right)\left(\frac{\varepsilon}{0.1}\right)10^{45}erg\,s^{-1}, \tag{1}$$

where L_{bol} is the bolometric luminosity of the AGN, $\dot{M}_{BH}$ is the mass accretion rate of the black hole, and ε is the mass-energy conversion efficiency, typically estimated to lie close to 0.1 (e.g. Marconi et al. 2004; Merloni 2004).

The luminosity emitted by steady accretion is bound by the Eddington luminosity,

$$L_{Edd} = \frac{4\pi\,G\,M_{BH}\,m_p\,c}{\sigma_T} = 1.3\times10^{46}\left(\frac{M_{BH}}{10^8M_\odot}\right)erg\,s^{-1}, \tag{2}$$

where G is the gravitational constant, m_p is the proton mass, c is the speed of light and σ_T is the Thompson cross section of the electron. This luminosity that scales with the mass of the SMBH is achieved when the outward radiation pressure equals the inwards gravitational force. If the luminosity exceeds the Eddington luminosity the gas is expelled.

Within the accretion disc, magnetic fields and turbulence transport angular momentum outwards and mass inwards down to the innermost stable circular orbit of the black hole, beyond which the material plunges into the event horizon of the black hole, located at the Schwarzschild radius for a non-rotating black hole,

$$R_S = \frac{2\,G\,M_{BH}}{c^2} \simeq 10^{-5}\frac{M_{BH}}{10^8M_\odot}\ pc. \tag{3}$$

Although the details of the angular momentum transport mechanism are not yet fully understood, they can be modelled as an effective viscosity described by a single parameter, giving rise to the so-called Shakura & Sunyaev (1973) α-disc model (see also e.g. Pringle 1981; Balbus & Hawley 1998). This model describes optically thick and geometrically thin discs. The gas at each radius of such a disc is predicted to radiate with a black body spectrum profile corresponding to an effective Temperature

$$T_{eff} \simeq 6.2\times10^5\left(\frac{\lambda}{\varepsilon_{0.1}\,M_8}\right)^{1/4}\left(\frac{r}{R_S}\right)^{-3/4}K, \tag{4}$$

where $\varepsilon_{0.1}$ is the radiative efficiency in units of 0.1, M_8 is the mass of the black hole in units of $10^8M_\odot$ and $\lambda = L_{bol}/L_{Edd}$. The emitted radiation spans a wide range of wavelengths, with most of the power peaking in the optical, ultra-violet (UV) and X-rays.

The kind of discs just described are able to transport gas down to the event horizon of the black hole only if the gas is already located at $r \lesssim 0.1$ pc, as further out the viscous time scale grows larger than the Hubble time and the self-gravity of the gas could become important enough to disrupt the disc and form stars (e.g. Goodman 2003; King & Pringle 2007; King 2008). This radius is approximately (e.g. Pringle 1981):

$$r_{sg} \simeq 0.01 \left(\frac{\alpha}{0.3}\right)^{14/27} \left(\frac{\epsilon}{0.1}\right)^{8/27} \left(\frac{L}{0.1 L_{Edd}}\right)^{-8/27} \left(\frac{M_{BH}}{10^8 M_\odot}\right)^{1/27} \text{pc}, \tag{5}$$

where α is the Shakura & Sunyaev (1973) viscosity parameter.

1.2 THE GROWTH OF MASSIVE BLACK HOLES

Some years before black hole measurements were available, Soltan (1982) had already established that, by integrating the energy output we observe from AGN across cosmic time, and assuming that the main source of fuel of quasars is gas accretion, we should observe the relics of quasars as quiescent black holes in the local universe. He calculated the black hole mass density in the local universe as:

$$\rho_{BH} = \frac{1-\varepsilon}{\varepsilon\, c^2} \int_0^z \frac{dt}{d\zeta} d\zeta \int \frac{\partial \phi(L_{bol}, z)}{\partial \log L_{bol}} dL, \tag{6}$$

where $\phi(L_{bol}, z)$ is the (comoving) number density of quasars with luminosity L_{bol} at redshift z. ϵ, c and t have their usual meanings: accretion efficiency, speed of light and (cosmic) time.

At the present time it is widely accepted that SMBH are ubiquitous in the centres of galaxies in the local universe (Kormendy & Richstone 1995; Kormendy & Gebhardt 2001; Kormendy & Ho 2013). By measuring a significant sample of BH masses in the local universe, a BH mass distribution can be extracted (Magorrian et al. 1998; Salucci et al. 1999; Marconi et al. 2004; Shankar et al. 2004; Schulze & Wisotzki 2010; Goulding et al. 2010). Integrating this distribution one can obtain the total local mass density of black holes, $\rho_{BH} \sim (3-5) \times 10^5 M_\odot$ Mpc^{-3}. By comparing this observed mass density with the one expected by the *Soltan argument*, it is possible to estimate the average accretion efficiency. The estimated average values lie between 10 and 15 percent, implying that black holes are rotating in general (e.g. Fabian & Iwasawa 1999; Elvis et al. 2002).

Assuming an initial distribution of small black holes at high redshift (seeds), one can follow the mass growth of the black holes due to mass accretion inferred from the luminosity function at each redshift. The black hole mass distribution obtained at redshift $z = 0$

should match the observed local mass function (e.g. Small & Blandford 1992; Chokshi & Turner 1992; Salucci et al. 1999; Marconi et al. 2004; Merloni 2004; Cao 2007; Shankar et al. 2009).

Although the models used to follow the BH mass evolution depend on several parameters (luminosity function, local black hole mass distribution, bolometric correction, fraction of missed obscured objects, accretion efficiency and Eddington ratio), there is a sound consensus that the growth of black holes proceeds by radiative efficient accretion at an average efficiency of $\varepsilon \simeq 0.1$ and Eddingon-limited accretion, $\lambda < 1$. Regarding the actual mass history of the BH population, some clear trends have emerged from a broad range of different approaches, ranging from simple analytical/synthetic models to more detailed semianalytical models and N-body/hydrodynamical simulations (Marconi et al. 2004; Merloni 2004; Shankar et al. 2004, 2009; Hopkins et al. 2006a, 2008; Malbon et al. 2007; Di Matteo et al. 2008; Somerville et al. 2008; Fanidakis et al. 2012; Sesana et al. 2014): (1) the average Eddington ratio for BHs decreases with redshift, from rapidly growing systems at $z > 2-3$ to comparatively slow growing systems at $z < 1$, and (2) the characteristic "active" BH mass decreases with redshift. However, there are significant differences between some studies in terms of the build-up of the BH mass function with redshift. For example, in the semianalytical model of Fanidakis et al. (2012), the lower mass end of the BH mass function ($M_{BH} < 10^8 M_\odot$) is essentially in place by $z \sim 2$ while the high-mass end is predominantly built by BH mergers of lower-mass BHs and modest mass accretion rates through to the present day. By comparison, in the AGN synthesis models of Marconi et al. (2004) and Merloni & Heinz (2008) the lower-mass end of the BH mass function is only in place by $z < 0.1-0.6$. These different models serve to illustrate some of the uncertainties that remain in modelling the evolution of the BH mass function.

1.3 CO-EVOLUTION OF BLACK HOLES AND GALAXIES

One of the greatest astronomical discoveries made at the beginning of this century is the finding of tight correlations between SMBHs and their host galaxies. From the earlier results of Dressler & Richstone (1988); Dressler (1989) in which the masses of a small sample of two and five SMBHs were shown to be proportional to the luminosities of their host spheroids ($M_{BH} \propto L_{bulge}$), it was already evident that a deeper relationship could exist. Based on seven galaxies, Kormendy (1993)[1] proposed an explicit relationship between the mass of the black hole and the mass of the host bulge: $\langle M_{BH}/M_{bulge} \rangle \simeq 0.0022$ ($M_{bulge} = \Upsilon L_{bulge}$; with Υ the mass to light ratio). Even if at that time the correlation could have just been the upper envelope of a distri-

1 see Kormendy & Ho (2013), p. 47

bution that extended to lower M_{BH}, it was consistent with values reported in the avalanche of literature that followed on the subject (e.g. Magorrian et al. 1998; Ho 1999; Merritt & Ferrarese 2001; Kormendy & Gebhardt 2001; McLure & Dunlop 2002; Marconi & Hunt 2003; Häring & Rix 2004; Ferrarese & Ford 2005; Graham 2007; Gültekin et al. 2009; Sani et al. 2011; Beifiori et al. 2012; McConnell & Ma 2013).

From this $M_{bulge} - M_{BH}$ relation alone it was already suspicious that galaxy and BH growth affect each other. However, the event that ignited the research on BH-galaxy co-evolution was the discovery of the tighter correlation between M_{BH} and σ, the host galaxy velocity dispersion, by Ferrarese & Merritt (2000) and Gebhardt et al. (2000). The importance of the $M_{BH} - \sigma$ relation resided in having only 0.3 dex of scatter over almost 3 orders of magnitude in M_{BH}, and most of it was due to observational errors. This correlation has not just been important at a fundamental level, but also has a practical value, as it allows accurate predictions of M_{BH} from easy-to-make measurements and because it implies that BH growth and bulge formation are closely linked.

It was later suggested that all these correlations are just signs of a more fundamental relation between the SMBHs and their host galaxies. In fact, correlations between M_{BH} and two of R_{bulge}, M_{bulge}, and σ are found to be tighter than correlations between M_{BH} and any one of these variables alone (Aller & Richstone 2007; Hopkins et al. 2007a,b). These correlations are commonly referred to as the BH fundamental plane (BHFP) [2]. Burkert & Tremaine (2010) recently discovered that BH masses also correlate with the total number of globular clusters of the host galaxies, N_{GC}, and suggested that major mergers could provide the connection between the smallest and the largest scales in galaxies. Snyder et al. (2011), however, argued that the tight $M_{BH} - N_{GC}$ correlation does not imply any direct connection between globular clusters and BHs. Rather, they argue that M_{BH} and N_{GC} both correlate primarily with galaxy binding energy, $\propto M_* \sigma^2$ (i.e. the BHFP).

The existence of these tight correlations, and in particular of the BHFP, were the first hints at a symbiotic connection between the formation and growth of SMBHs and galaxy spheroids, creating with their discovery a concrete goal in black hole growth calculations –the one of reproducing them by invoking galaxy/AGN interaction. In a comprehensive review, Kormendy & Ho (2013) conclude that the relations just described are tight enough to imply SMBH co-evolution with the properties of classical bulges and elliptical galaxies and with no other galaxy components such as discs and pseudo-bulges of disc galaxies. Identifying the physical drivers behind these relationships

2 Not to be confused with a correlation between M_{BH} and the X-ray and radio luminosities of AGNs (Merloni et al. 2003), which has the same name.

is one of the major challenges of extragalactic astrophysics and cosmology.

1.4 AGN FEEDBACK

The luminosity generated by AGN is in some cases comparable or even larger than the luminosity generated by the stars of the whole host galaxy. This fact, together with the relations described in section 1.3 suggest that SMBHs are not just playing a passive role in structure formation. The idea of SMBH playing a central role in the shaping their host galaxy and regulating their own growth was already in the air by the late 1990's. Silk & Rees (1998), Fabian (1999) and King (2003) explore scenarios in which strong winds coming from the BH couple to the surrounding gas and regulate both the growth of the BH and star formation in the host galaxy, giving rise to the observed $M_{BH} - M_{bulge}$ relation.

Direct observational evidence of AGN feedback in the form of high velocity winds has been found in local Seyferts showing outflowing gas on scales of $\sim 10 - 100$ pc (e.g. Storchi-Bergmann et al. 2007; Davies et al. 2009; Storchi-Bergmann et al. 2010; Schnorr Müller et al. 2011), or a low redshift quasar in which Young et al. (2007) observed a high velocity outflow of $\sim 4,000\,\mathrm{km\,s^{-1}}$. Even faster winds of $v \simeq 0.1 - 0.3c$ have been inferred by the presence of highly blue-shifted absorption and emission lines in a number of quasars and Seyferts (Pounds et al. 2003; Reeves et al. 2003; Tombesi et al. 2010; Lobban et al. 2011; Gofford et al. 2011). Further statistical studies of large numbers of AGN have also shown evidence for these kind of winds by measuring the blue-shift of the emission line $[O_{III}]$ (e.g. Boroson 2005; Mullaney et al. 2013). The magnitude of this shift is found to be correlated with a number of properties, including the width of the emission line itself and the Eddington ratio λ, consistent with a quasar expelling its surrounding material due to the radiative output generated by the SMBH. Another kind of feedback comes in the forms of jets: relativistic outflows with narrow opening outflows that are launched directly from the accretion flow itself. These relativistic jets are commonly observed to influence gas on scales well beyond the host galaxy ($\gtrsim$ kpc) and their impact was already evident since the early work by Scheuer (1974), who suggested that these jets heat their surrounding gas by strong shocks. However, thirty years later, *Chandra* observations made it clear that most of the mechanical energy from the jets was transferred to the environment in the form of PdV work by the inflating bubbles (e.g. Dunn et al. 2005; Bîrzan et al. 2008; Cavagnolo et al. 2010), with only a handful of cases showing clear signs of large-scale shocks (e.g. Forman et al. 2007; Croston et al. 2009).

In recent years, high-resolution cosmological hydrodynamical simulations have been available do to the huge technological advances (e.g. Springel et al. 2005b; Di Matteo et al. 2008; Vogelsberger et al. 2014; Hirschmann et al. 2014). However, due to the finiteness of resolution it will (likely) always be necessary to adopt sub-resolution prescriptions to model the effects that AGN and star formation produce on their environment (i.e. Springel et al. 2005a; Di Matteo et al. 2005; Booth & Schaye 2009; Teyssier et al. 2011). It may seem clear now that AGN feedback is of great importance not only to reproduce the observed M_{BH}—host spheroid relations by significantly decreasing the overall star formation, but also to reproduce the properties of galaxy clusters and groups, such as temperature, entropy and pressure radial profiles and intra cluster medium (ICM) chemical enrichment (e.g. Fabjan et al. 2010; Ragone-Figueroa et al. 2013; Barai et al. 2014; Planelles et al. 2014; Taylor & Kobayashi 2015; Steinborn et al. 2015). It has also been shown that the heating from the AGN and the radiative cooling are often in relatively close balance (Rafferty et al. 2008), suggesting a limit cycle in which the cooling of hot gas onto the nucleus of the galaxy fuels intermittent AGN outbursts, the gas then heats again and the accretion slows down or stops (e.g. Best et al. 2005; Pope 2011). This scenario represents feedback in the true sense of the term, in that the energy output by the AGN has a direct impact on its own fuel supply.

In 2012, a comparison project was carried out with the aim of testing several different hydrodynamical codes and sub-grid prescriptions for AGN feedback and star-formation (The Aquila comparison project; Scannapieco et al. 2012). Each simulation of the project had the task of forming a galaxy from the same initial conditions (common halo assembly history). The large code-to-code variations observed in the stellar mass, size, morphology and gas content of the galaxy at $z = 0$ were mainly due to the different implementations of star formation and AGN feedback. In general, models that were more effective at limiting the baryonic mass of the galaxy were better at reproducing the observed galaxy scaling laws, but not so on achieving a realistic galactic disc. The lesson learned was that the discrepancies due to the different numerical techniques used were small when compared to the variations induced by different feedback prescriptions. As for the day of writing, developing universal feedback algorithms that can effectively reproduce all the observed properties of a galaxy and its environment at once remains a challenge.

It must be said, however, that there are other ways of getting the BHs-spheroid relationships in which feedback plays just a secondary role. For instance, Booth & Schaye (2010) suggests that BHs grow until they are massive enough to unbind gas not only from their host galaxies, but from their entire surrounding haloes. At this point they stop growing and the observed BH-spheroid correlations are set. In

this scenario the galaxy is not shaped by feedback from the BH but the BH is shaped by the binding energy of the dark matter halo. Yet another scenario is that in which the observed relations are just a consequence of the hierarchical growth of structure (e.g. Peng 2007; Jahnke & Macciò 2011): Mergers of BHs following mergers of galaxies would tend to drive the resulting galaxies toward the observed relations even if in the parent smaller galaxies such relations were absent.

The shortcoming of numerical simulations is the lack of understanding of the driving mechanisms triggering AGN phenomena and BH growth. Generally it is assumed that a fraction of the interstellar medium (ISM) is flowing into the central $\sim$ kpc, under the rather simplified conditions studied by Bondi (1952), and is finally accreted by the BH at a rate

$$\dot{M}_{BH} = f(\gamma) 4\pi (G M_{BH})^2 \frac{\rho_\infty}{c_{s\,\infty}^3} \tag{7}$$

where $f(\gamma)$ is a proportionality factor of order unity depending on the adiabatic index γ and the subscript ∞ means to evaluate the quantities far away from the BH. This prescription is broadly valid if the transport of gas from $\sim$ kpc scales (the resolution limit) down to the BH is indeed efficient. In the same fashion, feedback is modelled by transferring a fraction of the calculated radiative output of the BH to the thermal energy of the surrounding gas, without describing the outflow in detail, as the complexity of the real accretion-feedback process makes it impossible to make predictions analytically. In the last decade, a lot of research have been devoted to quantify the deviations from this simplistic scenario, using numerical (e.g. Pen et al. 2003; Proga & Begelman 2003; Krumholz et al. 2005, 2006b; Igumenshchev 2006) or semi-analytical approaches (e.g. Quataert & Narayan 2000; King & Pringle 2006; Soker 2006; Nayakshin et al. 2007; Pizzolato & Soker 2010; Narayan & Fabian 2011; Hobbs et al. 2012; Mathews & Guo 2012). In particular, Gaspari et al. (2013) used three-dimensional adaptive mesh refinement (AMR) simulations to link the behaviour of gas at small sub-Bondi spatial scales to that at large $\sim$ 50 kpc scales. They showed that the mode of accretion is *cold and chaotic*, leading to a boost of the accretion rate of up to 100 times the Bondi rate, with the important implication of linking the accretion rate of the BH to the cooling time of the gas. This in turn leads to a more natural sub-resolution prescription of BH accretion and feedback for cosmological simulations. In the same spirit, Carmona-Loaiza et al. (2014) have shown that two uncorrelated inflows of gas at different times and with different angular momentum direction can substantially increase the accretion rate towards the central parsec of a galaxy, suggesting that a sub-resolution prescription for BH accretion should

take into account the angular momentum history of the gas at the resolution scale.

1.5 INFLOW OF GAS AT DIFFERENT SCALES

As we have seen in the previous sections, SMBHs can exert a substantial role on shaping their environment. However, for an SMBH to shine as an AGN, mass has to be supplied at a rate of $10^{-4} - 10 M_\odot\,\mathrm{yr}^{-1}$ (see section 1.1). The amount of gas in a typical Seyfert galaxy is well in excess of what is needed to power the AGN, for instance, assuming an accretion rate of $10^{-2} M_\odot\,\mathrm{yr}^{-1}$ and a duty cycle of 10^8yr, a single gas cloud of $10^6 M_\odot$ may provide enough fuel. Such clouds are certainly common within the inner 200 pc radius of spiral galaxies, but the physical processes able to remove more than 99.99% of it's angular momentum are yet to be understood (e.g. Jogee 2006; Alexander & Hickox 2012).

At galactic scales the presence of the black hole is negligible. Indeed, the black hole is just $\sim 1/1000$ as massive as the bulge of a galaxy, which means that gas has to be driven down to the sphere of influence of the BH,

$$r_{SI} = \frac{G M_{BH}}{\sigma^2}, \tag{8}$$

to start being influenced by its presence. Assuming typical values of $M_{BH} \simeq 10^8 M_\odot$ and $\sigma \simeq 200\,\mathrm{km\,s^{-1}}$, $r_{SI} \simeq 10$ pc. Even at these scales, there is still a long way to cover before reaching the accretion disc of the BH. All in all, from galactic ~ 10 kpc scales to the event horizon of the BH, gas has to travel a long way spanning 5-6 orders of magnitude of length-scale to reach the BH accretion disc, where it will be ultimately funnelled inside the event horizon.

1.5.1 *The accretion disc*

The transport of angular momentum within a gaseous disc circling around a gravitating point-like mass, requires the action of dissipative processes which spread the disc out, allowing the inner parts to move in and the outer parts to move out, due to conservation of angular momentum. Angular momentum transport was well understood by the 1920's in the context of the evolution of the early solar nebula (Jeffreys 1924) [3], and turbulence was already recognized as a suitable mechanism for accomplishing this task in the 1940's (e.g. Peek 1942;

3 Coincidentally, also in the decade of the 1920's, Edwin Hubble (19 February 1924) wrote a letter to Harlow Shapley in which he showed the curve of luminosity of the first Cepheid variable star discovered by him in the Andromeda Nebula, M31. Using this information he could determine Andromeda's distance, and for the first time it was recognized as an object located outside and far away from our galaxy.

von Weizsäcker 1943, 1948; Lüst 1952), by acting as an effective viscosity. Following the discovery of quasars (Schmidt 1963) and X-ray binaries (Prendergast & Burbidge 1968), a strong link between angular momentum transport in accretion discs and the radiation they emit was forged (Shakura & Sunyaev 1973). While it has been possible to confront the accretion disc theory with observations in the case of X-ray binaries, some technical problems arise when trying to do the same exercise for AGN accretion discs, the main problems being that, as AGN lay outside Our Galaxy and thus significantly further away than X-ray binaries, the signal to noise ratio is low despite their power. Another issue is the fact that almost all the AGN radiation is emitted in the UV band, which is mostly absorbed by the ISM of Our Galaxy, making AGN accretion discs a subject of great theoretical speculation (See e.g. Li et al. 2013).

The common belief is that AGN accretion discs must be continuously or episodically replenished, as a large disc would fragment due to gravitational instabilities (e.g. Shlosman et al. 1990; Goodman 2003). For thin accretion discs, with aspect ratio $H/R \simeq 10^{-3}$, gravitational instabilities start being important at a distance of the order of $10^3 R_S$, which, for a black hole of $M_{BH} = 10^8 M_\odot$, is equivalent to 0.01 pc. On the other hand, such gravitational instabilities could lead instead to the development of (transient) spiral patterns, avoiding fragmentation (e.g. Lodato 2012).

The parameter that tilts the balance to either of these scenarios is the cooling time. Indeed, for a disc to be stable against self-gravity, the Toomre (1964) parameter,

$$Q = \frac{c_s \kappa}{\pi G \Sigma}, \tag{9}$$

must be greater than unity, with marginal stability occurring at $Q = 1$. When the cooling time-scale of the gas, t_{cool}, is greater than the dynamical time-scale of the disc, t_{dyn}, an initially hot disc ($Q > 1$) will slowly cool until the marginal instability stage is reached ($Q = 1$). During this process, the disc has had enough time to respond, forming from local gravitational perturbations a global spiral structure that in turn heats the gas through shocks and pdV work, preventing the disc to go into the fragmenting regime ($Q < 1$). Thus, the interplay between local self-gravity (governed by t_{dyn}) and the cooling of the gas (governed by t_{cool}) will dictate the evolution of the disc. In the scenario just described ($t_{cool} > t_{dyn}$), the spiral structure role is twofold: i) it acts as a thermostat, maintaining the gas always at marginal stability and ii) it transports angular momentum due to non axisymmetric gravitational torques and shocks. On the other side of the balance, if $t_{dyn} > t_{cool}$, as the disc cools faster than the time

Viscous-like discs would be recognized a fundamental part of these *island universes* some decades later in the study of AGN.

it needs to respond and develop a spiral structure, the disc breaks into clumps (for a more detailed discussion of these processes see e.g. Lodato 2007). What happens in a real AGN accretion disc is still unsure. Even if the cooling time at the scales where self-gravity becomes important is too short, turbulence could help stabilizing the disc against fragmentation (e.g. Begelman & Shlosman 2009), and, even if fragmentation did occur it is not clear whether the formation of clumps would preclude accretion.

1.5.2 *Within the sphere of influence and beyond*

The presence of Keplerian or quasi-Keplerian gaseous discs in the self-gravitating regime at parsec scales has been revealed through observations of maser emission around nearby AGN (Miyoshi et al. 1995; Greenhill et al. 2003; Kondratko et al. 2005; Kuo et al. 2011); at the same time, the nuclear stellar disc around Sgr A* indicates that fragmentation and star formation do effectively take place (Genzel et al. 2003; Levin & Beloborodov 2003; Ghez et al. 2005; Nayakshin & Cuadra 2005; Paumard et al. 2006; Genzel et al. 2010; See also Nayakshin et al. 2006; Levin 2007), making it even more difficult to account for black hole fuelling.

The transport of angular momentum from galactic scales down to the black hole horizon has been a long standing problem since the late 1980's. In fact, Shlosman et al. (1989) and Shlosman et al. (1990) envisioned that a system of nested bars (i.e. smaller bar instabilities with a shorter dynamical time and higher densities decoupled from within larger scale bars with longer dynamical times and lower densities) at ~ 1 kpc scales should be able to carry on the transport angular momentum as the torques exerted by the large scale ~ 10 kpc bars became weaker. More recently, in a series of SPH zoom-in resimulations, Hopkins & Quataert (2010a) have given more than a proof-of-concept for the *bars-within-bars* scenario. They have found that the *bars-within-bars* are going all the way down to the regions where the black hole potential dominates the dynamics, and possibly even down to where the AGN accretion disc forms. In their simulations they not only found bars but also spirals, rings, clumps and lopsided discs: generic non-axisymmetric features have the ability to torque the gas and make it inflow. Moreover, from the same set of resimulations, Hopkins & Quataert (2011) describe a possible scenario for accommodating black hole fuelling together with disc fragmentation, concluding that even if at scales between 1 and 10 parsecs the potential of the black hole still dominates, the self gravity of the gas plays a fundamental role: the interaction between stars formed *in situ* and gas can actually aid the developments of non-axisymmetric modes on the gas. The mode growth is faster in the stellar distribution, thus, as gas streams move through the lopsided stellar distribution they are

torqued, losing angular momentum and energy through orbit crossing (see also Chang et al. 2007).

At the largest scales of a galaxy, ~ 10 kpc, features can be readily observed with current telescopes and a dialogue between theory and observations can be immediately established. At these scales it has been shown that bars, galaxy mergers and interactions between galaxies have the potential of producing important inflows (Shlosman et al. 1989, 1990; Barnes & Hernquist 1992, 1996; Mihos & Hernquist 1996; Bournaud & Combes 2002; García-Burillo et al. 2005); AGN could be naively thought to be found preferentially in galaxies displaying the aforementioned features. However, observations tell us that there is at least a marginal relationship between the presence of AGN activity and galaxy bars (e.g. Mulchaey et al. 1997; Knapen et al. 2000; Martini et al. 2003; Simões Lopes et al. 2007) or systems undergoing a major merger (Darg et al. 2010; Lintott et al. 2011; although see also Colpi & Dotti 2009; Tueller et al. 2010; Koss et al. 2010; Schawinski et al. 2010; Liu et al. 2011) in the local Universe. The same conclusion held at smaller ~ 100 pc scales as no substantial differences were found between the circumnuclear morphologies of AGN and late-type quiescent galaxies: nuclear bars, spirals, discs and circumnuclear dust were equally likely to be found in all late-type systems (Laine et al. 2002; Pogge & Martini 2002; Martini et al. 2003; Hunt & Malkan 2004). Even if, while studying the circumnuclear regions of early type galaxies, Simões Lopes et al. (2007) found that AGN were only present in dusty environments, no unique signature has been found at these scales that reveals the ultimate triggers of AGN activity. The reason may lie in the (quite obvious, in hindsight) fact that the mechanisms leading to gas inflow act on different time-scales, producing a delay between their operation and the actual fuelling. This delay is expected to be as large as $\sim 10^8$ yr, comparable to or even longer than the duration of the AGN phase (e.g. Martini et al. 2003; Davies et al. 2007; Schawinski et al. 2009; Wild et al. 2010). It is inside the sphere of influence of the BH, at ~ 10 pc scales, where the real fuelling must be happening, in most of the cases hidden from our current telescopes.

1.5.3 *Triggers of AGN*

The current view is that a linked series of processes that remove the gas angular momentum is required in order to bring the gas to the BH, each of which on its own may not correlate with the presence of an AGN. At ~ 10 pc scales we largely rely on theoretical and numerical models to explore the triggers of inflow and AGN activity, as large columns of gas and dust obscure these regions ($N_H > 10^{22-25} cm^{-2}$, with absorbing column changes on $\lesssim 1$ yr timescales; e.g. Antonucci 1993; Risaliti et al. 1999; Willott et al. 2000; Guainazzi et al. 2005; Cappi 2006; although see also Tozzi et al. 2006; Raimundo et al. 2010;

Alexander et al. 2011; Merloni et al. 2014). BH growth and star formation within the spheroid of a galaxy are both expected to be driven by a cold gas supply. One must bear in mind, however, that BH growth not only requires cold gas but also low angular momentum gas. If the angular momentum of the gas is high, gas will pile up at some distance from the BH, reaching high densities and becoming unstable. It could then collapse and form stars (e.g. Toomre 1964; Thompson et al. 2005; McKee & Ostriker 2007; Lada et al. 2010), leading to a starburst and quenching BH fuelling; it could develop global non-axisymmetric modes, leading to further inflow (e.g. Hopkins & Quataert 2010a, 2011); or it could, if the mass is low enough, stay quiescently in orbit at a distance from the BH without triggering any star-burst nor BH fuelling. Nevertheless, this quiesent remnant structure could be of fundamental importance for catalysing BH fuelling if a later inflow were to interact with it (e.g. Carmona-Loaiza et al. 2014).

1.5.3.1 *Starbursts*

Using Adaptive Optics observations with resolutions of ~ 10 pc, Davies et al. (2007) provided compelling evidence that starbursts of ages of < 50 Myr were associated with lower Eddington ratios, finding at the same time that high accretion rates were only achieved in galaxies where the most recent burst of star formation was $50 - 100$ Myr old (See also Schawinski et al. 2009; Wild et al. 2010; González Delgado et al. 2001). The envisioned scenario that accounts for these observations is that, at very young ages, outflows from OB stars and Type II supernovae inject too much energy to the ISM, making it highly turbulent and ultimately expelling the gas. After 50-100 Myr, these phase ends and slower outflows from AGB stars take over, kinetic energy is not enough to expell the gas anymore and turbulence, rather than expelling the gas, cancels its angular momentum, making it available for accretion. This interpretation is in line with models by Vollmer et al. (2008) and Schartmann et al. (2009, 2010), who, motivated by the stochastic nature of gas inflow at large scales, suggested a model in which the star formation and dusty torus properties were also time dependent in the same fashion (See also King & Pringle 2007; Nayakshin et al. 2009). These models linked the properties of a star forming cluster on scales of 10-50 pc with those of more compact structures on scales of 0.1-1 pc. Incidentally, Cuadra et al. (2006) and Cuadra et al. (2008) showed through hydrodynamical simulations that, in the inner 0.5 pc of the Galactic Centre, fast stellar winds and the angular momentum of the parent stars inhibit accretion to smaller scales, and Chang et al. (2007) suggested that mass lost from older red stars in the central 2 pc of M31 could be replenishing a compact gravitationally unstable gas disc of $\sim 10^5 M_\odot$ every 0.1 - 1.0 Gyr.

On tackling the same problem, analytical models and numerical simulations performed by Kawakatu & Wada (2008); Wada et al. (2009); Hobbs et al. (2011) suggest that BH fuelling should increase when turbulence is injected by supernovae to the ISM. Kawakatu & Wada (2008) show that star formation in the disc dominates over the growth of the BH with increasing fuel supply, decreasing the fractional amount of gas accreted by the BH. Wada et al. (2009) continues to explore this scenario, arguing that stellar winds and supernovae are able to puff up the optically and geometrically thick molecular torus and enhance the BH accretion rate by injecting turbulence into the ISM. Indeed, the presence of nuclear stellar rings close to the BH in nearby quiescent galaxies provide indirect evidence in support of this hypothesis (e.g. Nayakshin & Sunyaev 2005; Bender et al. 2005; Paumard et al. 2006; Schödel et al. 2007; Hopkins & Quataert 2010b). Hobbs et al. (2011) instead, argue that the increase of accretion due to turbulence can be understood based on the notion of 'ballistic' accretion, whereby dense filaments, created by convergent turbulent flows, travel through the ambient gas largely unaffected by hydrodynamical drag, impacting the inner boundary of their simulation directly. In addition to it, turbulence sets gas in wider angular momentum distribution, increasing the gas fraction that circularizes inside their accretion radius.

All these scenarios rely on the role played by stellar outflows in driving gas to smaller scales. The difference between them is whether gas inflow is synchronous with or subsequent to the star formation episode. The complex interplay between AGN activity, star formation and the consequent feedback depends mainly on the assumed stellar outflows and accretion timescales.

1.5.3.2 *Non axi-symmetric modes*

Integral Field Spectroscopy observations have been started to reveal nuclear $\sim$ 10 pc gas inflows of around $60\,\mathrm{km\,s^{-1}}$ in nearby AGN (Fathi et al. 2006; Storchi-Bergmann et al. 2007; Riffel et al. 2008; Davies et al. 2009; Schnorr Müller et al. 2011) in form of streams along nuclear spirals. Although these observations have been useful as a proof-of-concept for some theoretical models that predict gas inflows due to torques produced by non-axisymmetric potentials in the nuclear regions, they are only feasible for low-luminous AGN, as in higher luminosity AGN the gas kinematics are dominated by gas outflow signatures (e.g. Storchi-Bergmann et al. 2010; Hicks et al. 2013), and one must resort to spectropolarimetry, which can help distinguishing between inflows and outflows, revealing inflows in some galaxies of up to $900\,\mathrm{km\,s^{-1}}$ (Young 2000; Smith et al. 2004). Although AGN can be triggered by starbursts as well as by non axisymmetric potentials, some differences arise between these two scenarios. Assuming that in the former case the stellar-mass loss is dominated by AGB stars, the BH accretion–star formation ratio would be

$\sim 10^{-2} - 10^{-3}$ (e.g. Jungwiert et al. 2001). By contrast, on the basis of their multi-scale hydrodynamical simulation, Hopkins & Quataert (2010a) finds that the rate of BH accretion and star formation within the central 10 pc is approximately equal, and therefore 2-3 orders of magnitude larger than that predicted from stellar-mass loss. Volonteri et al. (2015) have recently studied through high time-, spatial- and mass-resolution hydrodynamical simulations the evolution of star formation and black hole fuelling during mergers. They find that BH accretion and nuclear (< 100 pc) star formation are correlated, with similar variability.

Although the precise mechanisms underlying BH fuelling and star formation in the nuclear regions of galaxies (and the existent relations between them) remain uncovered, it has become increasingly evident that the properties of gas at 10 pc scales, i.e. the obscuring torus, are directly coupled to star formation and that the torus is a rather complex dynamical entity, revealing different observational features (e.g. Elitzur 2008). That dusty tori and starbursts appear on similar scales is unlikely to be a coincidence–the dense gaseous and dusty structure is potentially both the outer regions of the BH fuel supply and a stellar nursery (Tristram et al. 2007, 2009; Raban et al. 2009; Kishimoto et al. 2011), exerting a less passive role than originally postulated in the unified AGN model (e.g. Antonucci 1993).

1.5.3.3 *Misaligned interacting inflows*

One of the salient aspects of the complexity of gas inflow is the discovery of little or no correlation between the angular momentum axis of material accreting on to the BH and the axis of the host galaxy disc (Keel 1980; Ulvestad & Wilson 1984; Schmitt et al. 1997; Kinney et al. 2000; Gallimore et al. 2006; See also Natarajan & Pringle 1998), which is not trivially expected. This misalignment can result in i) large covering factors of obscuration even if the discs are thin (e.g. Fruscione et al. 2005; Nayakshin 2005), and ii) lower BH spins: if BH accreted gas which angular momentum points always in the same direction, the BH spin would grow until the maximal value (Volonteri et al. 2005; Volonteri & Rees 2005; Berti & Volonteri 2008); on the other hand, if gas orbits get somehow randomized before being accreted, then the spin of the BH is kept low (Moderski & Sikora 1996; King & Pringle 2006, 2007), which has implications for AGN feedback (Blandford & Znajek 1977; Begelman et al. 1984 but see also Livio et al. 1999). Hopkins et al. (2012) showed that the instabilities which drive inflows naturally lead to large misalignments of the nuclear disc with respect to the disc of the host galaxy. The misalignments they find are mainly due to fragmentation of gas patterns (e.g. a spiral arm) on large scales (Nayakshin & King 2007; King et al. 2008; Levine et al. 2010) and secondary bars that, in the presence of dissipative processes, decouple their angular momentum and orbit plane

from the primary bars at larger scales (Heller et al. 2001 and references therein). It must be stressed that such misalignments arise due to the gravitational torquing between the gaseous and stellar components and thus are not expected to be reproduced in simulations for which 'live' stellar potentials are not included.

Integral Field Spectroscopy has proven to be a key tool to determine the dynamics of gas and stars in nearby systems. There have been found clear differences between the gas and stellar kinematics on $<$ kpc scales in nearby AGN, with the gas velocity fields showing significant departures from the regular circular orbits traced by the stars (e.g. Dumas et al. 2007; Stoklasová et al. 2009; Rodríguez-Zaurín et al. 2011). A broad range of features such as warps, counter-rotating discs, and motions out of the galactic plane, likely due to gas inflow and outflow, has been revealed (see e.g. Raimundo et al. 2013; Corsini 2014). These kind of features are present in both quiescent and AGN-host galaxies. On the theoretical side, Carmona-Loaiza et al. (2014) have recently carried out a suite of hydrodynamical simulations in which a stalled nuclear ($\sim$ 10 pc) gaseous ring acts as an obstacle for a secondary global inflow. In our simulations, the nuclear ring is formed after a global 100 pc inflow. As self-gravity is neglected the disc does not fragment in stars and remains in quiescent orbits at $\sim$ 10 pc from the BH supplying a negligible amount of fuel. When a secondary uncorrelated inflow is set, replica of the former one from which the ring was generated, the interaction between it and the disc can increase the accretion by as much as three orders of magnitude, provided that a strong misalignment exist between the two. The remnants of such *overlapping inflows* interactions, are nested warped nuclear discs at scales of 1-20 pc. Whether such interactions are important triggers for star formation has not yet been addressed, but we argue that angular momentum cancellation (as opposed to transport) within the central $\sim$ 100 pc of a galaxy plays an important role in producing large inflows, and that the evolution of the angular momentum direction is an important tracer of BH fuelling.

Misalignment and overlap between inflows can potentially have an impact in the field of cosmological and galaxy formation simulations. It has been known for some time that subgrid recipes for modelling AGN feedback and BH growth are not quite physically motivated, as they usually model accretion through Bondi-Hoyle method, which was developed under the rather restrictive conditions of an adiabatic, spherically symmetric, unperturbed and steady flow, leaving angular-momentum, radiative cooling, heating and turbulence out of the picture. In addition to it, this method is used even when the region of influence of the BH, its Bondi radius, is not resolved (e.g. Di Matteo et al. 2005; Springel et al. 2005a; Booth & Schaye 2009). All of this facts add up to wrong estimations of the accretion rate. Gas inflow is complex and most probably cannot be easily prescribed by

a simple equation. However, progress has been made on improving the Bondi-Hoyle model. For instance, by modelling the BH and its accretion disc as a sink particle (e.g. Bate et al. 1995; Bate & Bonnell 2005; Cuadra et al. 2006), Power et al. (2011) have produced a physically self-consistent BH accretion model that naturally accounts for the angular momentum of the gas. They have shown that, while the Bondi-Hoyle method predicts almost continuous high mass accretion rates in gas-rich systems, a sizeable fraction of the gas in the sink-particle model collapses to form stars and the mass accretion rate onto the BH is comparatively negligible. In the same spirit, Gaspari et al. (2013) focus on relaxing the assumptions made by the Bondi-Hoyle model and find that, by including cooling, turbulence and heating, non-linear growth of thermal instabilities develop and lead to the condensation of cold clouds and filaments when the cooling time is low enough. The recurrent collisions and tidal forces between clouds, filaments and the central clumpy torus promote angular momentum cancellation. The accretion proceeds in a *cold and chaotic* fashion and the accretion rate is boosted up to two orders of magnitude as compared with the Bondi prediction. They suggest that a good approximation to the accretion rate is the cooling rate. In a forthcoming work, Carmona-Loaiza et al. (2015), we show that the presence of a nuclear disc can trigger accretion of inflows that would otherwise settle quiescently in stable orbits far away from the BH, implying that not only the angular momentum with which gas infalls towards the black hole is an important measure of the accretion but also its interaction with already present structures.

2

SUPERSONIC TURBULENCE IN ASTROPHYSICS

Turbulence in astrophysics has been found to be a key ingredient for describing the interstellar medium (ISM), intracluster medium (ICM) and intergalactic medium (IGM), as well as for star formation (McKee & Ostriker 2007). In fact, already in 1949, Chandrasekhar chose turbulence –a new theory at that time, as the subject for his Henry Norris Russell prize lecture, envisioning the importance it had for the future development of astrophysics. However, even today, more than 60 years later, turbulence remains elusive even in the incompressible regime. Apart from the phenomenology provided by Kolmogorov (1941), one has to turn to numerical simulations to gain some insight. Turbulence is a universal phenomenon that arises as a result of the non-linear terms in the Navier-Stokes equation. Despite its universality, it is one of the least understood problems in classical physics. A self-consistent mathematical treatment does not exist and analytical research is constrained to finding appropriate closure equations that capture the bulk behaviour of a fluid (See e.g. Frisch 1995; Lesieur 1997).

As a matter of fact, numerical simulations play an ever more important role in describing astrophysical fluids, as they are often the only available tool to compute accurate theoretical predictions in the highly non-linear regime of gravitational dynamics and hydrodynamics. This is particularly true for the description of the interstellar medium with its inherently complex geometry and three-dimensional dynamics. For the development of the research presented in this Thesis, we used Smoothed Particle Hydrodynamics (SPH for short, Lucy 1977; Gingold & Monaghan 1977), a Lagrangian particle method for solving the equations of hydrodynamics. In contrast to grid-based (Eulerian) methods, in which quantities and derivatives are calculated at a fixed point in space, in the Lagrangian description they are evaluated in a coordinate system attached to each moving fluid element, i.e. to each moving sph particle. The Lagrangian nature of the SPH method offers high spatial adaptivity and allows for a better and more natural treatment of the complicated and dynamically changing flow geometries, often occurring in the absence of fixed boundaries. In addition, the coupling of the fluid to its own gravity can be easily included (Springel 2005). We also employ a time-dependent artificial viscosity scheme (Morris & Monaghan 1997) to reduce artificial dissipation. All these features make SPH a highly suitable method for the treatment of the problems tackled.

2.1 GAS DYNAMICS

A vast amount of literature has been written in which the derivation of the equations of fluid dynamics can be followed (See e.g. Choudhuri 1998; Rosswog & Brüggen 2007; Clarke & Carswell 2007 for texts with an astrophysical flavour). This section will be limited to give a short description of the most relevant equations that arise when studying astrophysical phenomena.

By applying Newton's second law to a fluid, one can obtain the Navier-Stokes equation,

$$\begin{aligned}\rho\left(\frac{\partial v_i}{\partial t}+v_j\frac{\partial v_i}{x_j}\right) = &-\frac{\partial p}{x_i}\\ &+\frac{\partial}{x_j}\left[\eta\left(\frac{\partial v_i}{x_j}+\frac{\partial v_j}{x_i}-\frac{2}{3}\delta_{ij}\frac{\partial v_k}{\partial x_k}\right)\right]\\ &+\frac{\partial}{\partial x_i}\left(\zeta\frac{\partial v_k}{x_k}\right)-\rho\frac{\partial\phi}{\partial x_i},\end{aligned} \tag{10}$$

where η and ζ are the shear and bulk viscosity coefficients respectively and summation over repeated indices is implied. ρ, $\vec{v}$, p and ϕ have their usual meaning: density, velocity, pressure and gravitational potential. This equation represents the most general description of fluid flows under the action of viscous stresses and, even if it is widely used in several branches of physics and engineering, as for today, the existence of its solutions and their smoothness has not been proved.

In most astrophysical applications, ζ can be regarded as zero and η is approximately constant (if not zero). In this case the Navier-Stokes equation takes the simplified form

$$\frac{\partial\vec{v}}{\partial t}+\vec{v}\cdot\nabla(\vec{v}) = -\frac{1}{\rho}\nabla p+\frac{\eta}{\rho}\left[\nabla^2\vec{v}+\frac{1}{3}\nabla\left(\nabla\cdot\vec{v}\right)\right]-\nabla\phi. \tag{11}$$

Since η appears always in the combination η/ρ, it is convenient to define $\tilde{\nu}=\eta/\rho$, the *kinematic viscosity* [1].

The Navier-Stokes equation together with the equation of mass conservation,

$$\frac{\partial\rho}{\partial t}+\nabla\cdot(\rho\vec{v}) = 0, \tag{12}$$

and a suitable equation of state,

$$p = p(\rho, T), \tag{13}$$

1 The kinematic viscosity is generally represented by the Greek letter ν –*nu*. Unfortunately, this notation can be a source of confusion due to its similarity with the Latin letter v used to designate the velocity, thus, we keep the letter ν to designate the velocity and refer to the kinematic viscosity by $\tilde{\nu}$.

should allow us to predict the state of a fluid flow at any given time if we know the properties of the fluid at some previous time. In astrophysics one is usually able to treat fluids as ideal gases and write a relation of the form $T = T(\rho)$, so that the equation of state simplifies to $p = p(\rho)$. Equations of state in which pressure is only function of density are called *barotropic*. Barotropic equations of state are usually written as $p = K\rho^{\gamma}$, where K is a constant depending on the entropy and γ is the specific heat ratio, $\gamma = C_p/C_v$. In the idealized case in which the exchange of heat between the flow and its surroundings is immediate, the flow can be described as isothermal and the equation of state becomes $p = c_s^2\rho$, where c_s is the speed of sound of the fluid.

Any flow, in general, can be described by two dimensionless parameters: the Mach number,

$$\mathcal{M} \equiv v/c_s, \tag{14}$$

and the Reynolds number,

$$\mathcal{R}e \equiv v\,L/\tilde{\nu}, \tag{15}$$

where L is a typical length-scale (Stokes 1851; Reynolds 1883). These parameters quantify the relative importance of each term in the Navier-Stokes equations. $\mathcal{M}$ specifies the ratio of the inertial term, $\vec{v}\cdot\nabla\vec{v}$, to the pressure term, $\nabla P/\rho$, and $\mathcal{R}e$ specifies the ratio of the inertial term to the viscous term, $\tilde{\nu}\nabla^2\vec{v}$. While there is no theorem relating the Reynolds number to turbulence, laboratory experiments suggest that flows at $\mathcal{R}e \gtrsim 3000$ are typically (but not necessarily) turbulent. On the other hand, flows at low Reynolds numbers usually remain laminar. In a similar fashion, for $\mathcal{M} \lesssim 0.3$ a flow can be safely approximated as compressible, and flows with $\mathcal{M} > 1$ become supersonic and thus highly compressible.

Describing a medium as a fluid is possible if we can define physical quantities such as density or velocity at a particular point in space at a given moment. For a meaningful definition of a 'fluid velocity' we must average over a large number of the particles conforming the fluid. In other words, fluid dynamical quantities are well defined only on a scale much greater than a typical particle mean free path. At the same time, in order to have a local description of a fluid, the scales in which the fluid is described must be much smaller than the typical macroscopic length scales on which fluid properties vary. Two situations of interest, in which the macroscopic behaviour of the fluid is dictated by the micro-physics wrapped into the viscosity coefficients, η and ζ, are found in turbulence and shocks.

In shock fronts, it is the existence of a decelerating term in the direction of the flow, proportional to the large local velocity gradient, that

causes the flow to pass from supersonic to subsonic, largely dissipating its bulk kinetic energy into thermal energy and heating the gas. The precise behaviour of the gas at crossing the shock is dictated by ζ. However, most of the times we are just interested in the properties of the flow on either side of the shock and we do not need to know anything about the viscosity. We can just treat the shock as a discontinuity subject to jump conditions imposed by the inviscid fluid equations. In turbulence, shear chaotic flows at all scales are established. The presence of shear viscosity, η (or equivalently $\tilde{\nu}$), triggers the energy flux from large scales to smaller scales. This cascade of energy flux ultimately culminates with the dissipation of the energy into heat at scales much smaller than the relevant scales in which the fluid is described. For instance, when numerically simulating fluid flows, the resolution scale is usually much bigger than the scales at which viscosity dissipates kinetic energy into heat and its effects are just included as a phenomenological sub-grid model.

2.2 SHOCKS

2.2.1 *Adiabatic Shocks*

When the speed of a fluid changes by more than the speed of sound, sound waves travelling against the flow reach a region where they cannot travel any further upstream and the pressure progressively builds there. A high pressure shock wave of infinitesimal thickness is formed. A way of easily seeing this is by introducing an obstacle within a fluid flow. If the flow is subsonic ($\mathcal{M} < 1$), pressure sound waves are able to communicate the presence of the obstacle to the surrounding fluid, both *upstream* and *downstream*, so fluid approaching the obstacle can gently avoid it from a distance and the flow remains smooth around it. On the other hand, if the obstacle is immersed in a supersonic flow ($\mathcal{M} > 1$), as pressure waves are slower than the fluid, they are not able to communicate the presence of the obstacle to the upstream part of the fluid. It is only on reaching the obstacle that the approaching fluid notices its presence and a steep velocity gradient develops, the upstream part being supersonic (with respect to the obstacle) and the downstream part being subsonic. The shockwave is the surface that separates these two regions of the flow, with a thickness comparable to the mean free path of the molecules that conform the fluid. Within this region, kinetic energy is dissipated by increasing the temperature and entropy of the fluid.

Mass, momentum and energy conservation across a shock wave are expressed by the Rankine-Hugoniot relations,

$$\rho_1 v_{1\perp} = \rho_2 v_{2\perp}, \tag{16a}$$

$$\rho_1 u_1^2 + p_1 = \rho_2 v_2^2 + p_2, \tag{16b}$$

$$\frac{1}{2}v_1^2 + e_1 + \frac{p_1}{\rho_1} = \frac{1}{2}v_2^2 + e_2 + \frac{p_2}{\rho_2}. \tag{16c}$$

These relations hold in the reference frame in which the shock front is at rest. Sub-indices $[1, 2]$ tag the pre-shocked and post-shocked regions of the fluid respectively, while the symbol $\perp$ tags the component of the velocity field perpendicular to the shock. The components of the velocity parallel to the shock, $\vec{v}_{\parallel}$, are the same on either side of the shock ($\vec{v}_{1\parallel} = \vec{v}_{2\parallel}$).

The first Rankine-Hugoniot relation expresses simply mass conservation, the second expresses the fact that ram pressure is being converted to thermal pressure and the third relation expresses the conversion of kinetic energy into enthalpy. With some algebraic manipulation, these relations can be cast into a very convenient way relating the jumps of the density, pressure and velocity (we drop the sub-indices $\perp$ for the velocities):

$$\frac{\rho_2}{\rho_1} = \frac{(\gamma+1)p_2 + (\gamma-1)p_1}{(\gamma+1)p_1 + (\gamma-1)p_2} = \frac{v_1}{v_2}, \tag{17}$$

which becomes, in the limit of strong shocks ($p_2 >> p_1$):

$$\frac{\rho_2}{\rho_1} \simeq \frac{\gamma+1}{\gamma-1}. \tag{18}$$

Viscosity renders the process of shock-heating an irreversible one. Indeed, the relation $p/\rho^\gamma = K = \text{constant}$, valid for reversible processes, breaks down on shock-crossing and the gas jumps to a higher adiabat, even if heat is not being introduced nor extracted from the gas. Gas increases its entropy on crossing the shock, nevertheless Rankine-Hugoniot relations does not take that fact into account. This is because Rankine-Hugoniot relations deal with two regions of a perfectly inviscid fluid, yet, the existence of these relations is a direct consequence of viscosity. This shouldn't be a matter of concern, as we are usually interested only in the pre- and post- shock properties of the fluid. However, correctly accounting for the macroscopic effects of viscosity is of paramount importance when numerically modelling shocks, as the scales at which viscosity acts are usually unresolved, yet, significantly affect the macroscopic behaviour of the flow. For instance, as in astrophysical flows viscosity can be completely neglected ($\zeta = \tilde{\nu} = 0$), numerically modelling them requires the introduction of

an *artificial viscosity* term to treat shocks. Otherwise one risks ending up with regions in which the properties of the fluid are multivariate. We will discuss this in chapter 3.

2.2.2 *Isothermal Shocks*

It is likely that the flow will cool after having passed the shock front, possibly reaching its pre-shock temperature after some time. If the distance traveled by the flow during that time is very short compared to the length-scales of interest, we can regard the cooling region, together with the shock, as infinitesimal. If this is the case, we can go further with the abstraction and assume an *isothermal shock*. In this case, the third Rankine-Hugoniot condition (Equation 16c) is replaced by the simple condition that the flow as returned to its original temperature:

$$T_1 = T_2. \tag{19}$$

This condition, together with the first two Rankine-Hugoniot conditions (Equations 16a and 16b), can be used to relate the pre-shock Mach number to the compression ratio of the shock:

$$\frac{\rho_2}{\rho_1} = \frac{v_1}{v_2} = \left(\frac{v_1}{c_s}\right)^2 = \mathcal{M}^2. \tag{20}$$

Comparing this compression ratio with that given by the adiabatic shock (Equation 18), we notice the important difference that, while for adiabatic shocks the compression ratio is a finite number ($= 4$ for $\gamma = 5/3$), for isothermal shocks the compression ratio can be large without bounds, taking arbitrary high values for highly supersonic flows ($\mathcal{M} >> 1$).

The strong radiative cooling processes of the ISM make its equation-of-state approximately isothermal, such that very strong shocks and high compression ratios are associated with the supersonic gas motions. The relevant equation of state for the highly turbulent and compressible ISM is thus isothermal (e.g. Mac Low & Klessen 2004). We will work with such an equation of state throughout this Thesis. Let us now turn to another important feature of astrophysical fluids.

2.3 TURBULENCE

If we were on a plane, the sound of this word would immediately push us to fasten our seatbelts and sit tight. It would tell us that some forces are going to be exerted on the plane shaking it up and down with an unpredictable frequency. Although turbulence is an irregular state of motion of a fluid, characterized by chaotic property changes

such as rapid variations of pressure and flow velocity in space and time, an underlying statistical order nevertheless persists. In a non-turbulent flow there is a strong correlation between some property of the flow (e.g. the velocity $\vec{v}$) at a given point $\vec{v}(\vec{x})$ and that at another point $\vec{v}(\vec{x}+\vec{r})$: The flow proceeds along well defined streamlines. When a flow becomes turbulent, the situation changes and unsteady vortices appear on many scales, making the strong correlation between the velocities to disappear. However, scale-dependent spatial correlations still prevail, assuring us that however unpredictable turbulence is, our plane will still continue flying.

2.3.1 *The energy spectrum*

In the first attempt at forecasting the weather numerically –and in this context numerically means solving differential equations *by hand*, Richardson (1922) described turbulence in a rhyming verse:

> *Big whirls have little whirls that feed on their velocity,*
> *and little whirls have lesser whirls and so on to viscosity.*

This verse correctly conveyed the idea of turbulence being conformed by eddies of different sizes, with unstable larger eddies breaking up into smaller ones. In this way, the turbulent energy was passed from large scales to smaller scales in a turbulent cascade until it was dissipated by molecular viscosity at a sufficiently small length scale. Two important length scales are to be noted in this description: The scale at which turbulence is being stirred –the *energy containing scale*, l_s, and the scale at which it is dissipated by viscosity –the *dissipation scale*, l_d. With these ideas in mind, Kolmogorov (1941) first hypothesized that, for sufficiently high Reynolds numbers, energy was transported between scales as a spectral cascade and that the properties of the stirring mechanisms at l_s were lost so that at much smaller scales the motion became locally homogeneous and isotropic. On reaching l_d, energy should then be dissipated at a constant rate ϵ_0 depending only on the viscosity of the fluid, $\tilde{\nu}$.

Mathematically, the hypothesis of Kolmogorov reads: $\dot{e} = \text{constant} = \epsilon_0$ at all scales, i.e. the (specific) energy flows, from eddies of size $l + dl$ to eddies of size l, with l in the inertial range ($l_d << l << l_s$), at a constant rate equal to the energy dissipation rate by viscosity, ϵ_0, at l_d. This implies that a stationary situation exists in which energy is distributed in some specific way among eddies of different sizes l.

The *energy spectrum* is a measure of the kinetic energy contained in eddies of size $l \sim 2\pi/k$. It is related to the velocity field randomness and its autocorrelation at different scales (See Appendix A), and its dependence on k can be easily obtained by using the Kolmogorov

hypothesis that the energy dissipation is the same at all scales and that a stationary situation prevails. Dimensional analysis gives:

$$E(k) \propto \epsilon_0^{\alpha} k^{\beta} \propto \left[\frac{v^2}{t^3}\right]^{\alpha} \left[\frac{1}{l}\right]^{\beta} = \frac{l^3}{t^2}. \tag{21}$$

In this elegant phenomenological way Kolmogorov reached the conclusion that, within the *inertial range* (i.e. wave-numbers contained in scales l such that $l_d << l << l_s$), energy was distributed among the different wave numbers in the following way:

$$E(k) = C\, \epsilon_0^{2/3} k^{-5/3}, \tag{22}$$

where C is a dimensionless constant. This is the famous *Kolmogorov 5/3 law*, a first quantitative description of turbulence. This relation is of fundamental importance, as an homogeneous and isotropic turbulent flow is completely described by it. We similarly define the *power spectrum* of the velocity field $\vec{v}$ as:

$$P[v](k) \equiv \frac{E(k)}{2\pi k^2}. \tag{23}$$

For a deeper discussion see Appendix A.

2.3.2 *Turbulence in Astrophysics*

Gas dynamics in the ISM is typically characterized by very high Reynolds numbers, due to the low gas densities and physical viscosities encountered in these environments. We hence expect turbulent cascades over large dynamic ranges to prevail, provided the existence of a driving mechanism. Indeed, emission lines in molecular clouds have been observed to be wider than implied by the excitation temperature of the molecules, a fact that has been interpreted as the results of turbulent motions (e.g. Mac Low & Klessen 2004 and references therein).

Within the interstellar medium, good turbulence drivers are supernova explosions and expanding ionizing shells from previous star formation cycles (McKee 1989; Balsara et al. 2004; Krumholz et al. 2006a; Breitschwerdt et al. 2009; Goldbaum et al. 2011; Lee et al. 2012), gravitational collapse and accretion (Vázquez-Semadeni et al. 1998; Elmegreen & Burkert 2010; Klessen & Hennebelle 2010; Choi et al. 2013), shock compression in galactic spiral arms (Dobbs & Bonnell 2008), magneto-rotational instability (Piontek & Ostriker 2007; Tamburro et al. 2009), winds, jets and outflows from young stellar objects on smaller scales (Norman & Silk 1980; Banerjee et al. 2007; Cunningham et al. 2009; Carroll et al. 2010; Moraghan et al. 2013), and the

collapse of primordial haloes and feedback from first stars at high redshifts (Greif et al. 2008; Green et al. 2010; Latif et al. 2013).

Interstellar turbulence must be highly supersonic (thus compressible), due to the low densities and viscosities present (Elmegreen & Scalo 2004; Mac Low & Klessen 2004; McKee & Ostriker 2007), and its study is of paramount importance in modern astrophysics, as it not only controls the rate of star formation triggered by gas compression in shocks (Krumholz & McKee 2005; Hennebelle & Chabrier 2011; Padoan & Nordlund 2011; Federrath & Klessen 2012), affects the star formation efficiency (Elmegreen 2008; Federrath & Klessen 2013; Kainulainen et al. 2013) and determines the mass distribution of stars when they are born (Padoan & Nordlund 2002; Hennebelle & Chabrier 2008; Hopkins 2013), but also regulates the gravitational instability on galactic discs (Romeo et al. 2010; Hoffmann & Romeo 2012). Even the early Universe was likely dominated by supersonic turbulence. (Abel et al. 2002; Greif et al. 2008; Wise et al. 2008; Schleicher et al. 2010).

Since turbulence has always been an elusive subject, the early attempts to understand the compressible-supersonic turbulence of the ISM by von Weizsäcker (1943, 1951) and Chandrasekhar (1949) were based on insights drawn from the only theory of turbulence available at the moment: incompressible Kolmogorov (1941) turbulence. A first attempt to analytically derive the density spectrum and resulting gravitational collapse criterion was first made by Chandrasekhar (1951a,b). These studies were followed by several papers, which culminated in a work by Sasao (1973) on the density fluctuations in self-gravitating media. Later steps were taken on the subject by Larson (1981), who qualitatively applied the basic idea of density fluctuations driven by supersonic turbulence to the problem of star formation, Bonazzola et al. (1992), who used a re-normalization group technique to examine how the slope of the turbulent velocity spectrum could influence gravitational collapse, and by Panis & Pérault (1998), who combined this approach with numerical models to derive an effective adiabatic index for compressible-subsonic turbulence.

A fundamental idea for the scaling of supersonic turbulence was proposed by Lighthill (1955) and later refined by Henriksen (1991), Fleck (1996) and Kritsuk et al. (2007). This idea departed from the dimensional analysis by Kolmogorov with the only difference that, being a compressible medium, the relevant quantity to be cascaded from the large to the small eddies was the energy density ($\propto \rho v^2$), rather than the specific energy ($\propto v^2$). Under these assumptions it was shown that the Kolmogorov scaling for the ESD was preserved even for highly compressible turbulence, if the velocity v were substituted by the density weighted velocity, $\rho^{1/3}v$. In these case, $P[\rho^{1/3}v] \propto k^{-5/3}$. Early numerical studies (Porter et al. 1994; Frisch 1995) indicated that compressible turbulence may indeed exhibit a turbulent ve-

locity spectrum very similar to the one found by Kolmogorov (1941). The resolution of these early simulations, however, did not allow to follow the fluid over a significant inertial range, and the turbulence was only mildly compressible ($\mathcal{M} \lesssim 1$).

An exact relation for the scaling of compressible isothermal turbulence which predicts instead $P[\rho^{1/3}v] \propto k^{-19/9} \simeq k^{-2.1}$ was derived by Galtier & Banerjee (2011). Their model applies for turbulence with a very strong compressive ($\nabla \cdot \vec{v}$) component. Only at $\mathcal{M} \sim 1$ the spectrum approaches $P[\rho^{1/3}v] \propto k^{-5/3}$. The reason for this change on the slope is an adittional scale-dependent dissipation due to shocks, in contrast to the Kolmogorov turbulence, for which the scale of dissipation is fixed at the dissipation scale at which viscosity dissipates energy and ϵ = const. over the inertial range. In the supersonic case, a better mathematical approximation to the turbulence developed is Burgers turbulence (Burgers 1948), which consists of a network of discontinuities (shocks) that form due to the supersonic nature of the flows. What Galtier & Banerjee (2011) showed is that, if $\epsilon_{\rm eff}(r) = \epsilon + S(r)$, the additonal term $S(r)$ leads to a modified slope of the power spectrum. They also say that one may expect a scaling $\epsilon_{\rm eff} \propto S(r) \propto r^{2/3}$ for turbulence with a strong compressive component, in which case $P[\rho^{1/3}v] \propto k^{-19/9}$.

The key difference between Kolmogorov (incompressible) turbulence and supersonic (compressive) turbulence is that, while Kolmogorov turbulence has a purely solenoidal velocity field, supersonic turbulence velocity field exhibits in addition a highly compressive component[2]. While the existence of an inertial range was well established for incompressible turbulence (Frisch 1995), this may have not been the case for supersonic turbulence. It was only recently that Aluie (2011, 2013) rigorously proved the existence of an inertial range for highly compressible turbulence produced by any type of driving mechanism, solenoidal or compressive.

With the advent of supercomputers combining thousands of compute cores in one large-scale parallel application, the spectral scaling of supersonic turbulence has been measured with improved precision (Kritsuk et al. 2007; Federrath et al. 2010), indicating values of $P[v] \propto k^{-2}$. However, the studies by Kritsuk et al. (2007) and Federrath et al. (2010) were limited in resolution, which did not allow for accommodating a sufficiently large inertial range. Kritsuk et al. (2009) performed the highest resolution simulation of supersonic turbulence until then, with $\mathcal{M} = 6$. This Mach number is clearly in the supersonic regime, however, typical molecular clouds in the Milky Way are observed to have Mach numbers ranging from about $\mathcal{M} = 5 - 20$, and

2 The two extremes of a purely solenoidal field and a purely compressive field are characterized by: $\nabla \cdot \vec{v} = 0$ and $\nabla \times \vec{v} = 0$ respectively. Real flows exhibit in general a mixture of these idealized velocity fields.

sizes in the range 1–50 pc (e.g. Roman-Duval et al. 2010), which make them significantly more compressible.

Only very recently the computing power allowed Federrath (2013) to set up extremely high resolution hydrodynamical simulations of supersonic turbulent flows with a sizeable $\mathcal{M} = 17$. He compared the behaviour of turbulence under the two distinct driving mechanisms: purely solenoidal and purely compressive, finding a power spectrum for the velocity close to Burgers, $P[v] \propto k^{-2}$, for both driving modes. However, on analysing the density-weighted velocity, he didn't find the universal expected scaling ($P[\rho^{1/3}v] \propto k^{-5/3}$). What he found instead, was a dichotomy of behaviour for the two driving mechanisms: while the solenoidal component presented only a moderately steeper slope in its power spectrum with respect to the expected slope, $P[\rho^{1/3}v] \propto k^{-1.74}$, the compressive component power spectrum presented a substantially steeper slope, $P[\rho^{1/3}v] \propto k^{-2.1}$, confirming numerically the theoretical model of Galtier & Banerjee (2011), $P[\rho^{1/3}v] \propto k^{-19/9}$.

In the context of AGN feeding and super-massive black hole growth, it has been recognized by several authors that turbulence plays an important role, as i) together with magnetic fields, it is the mechanism believed to be behind α-viscosity in accretion discs (see Section 1.5.1), ii) it adds to the thermal pressure to stabilize self-gravitating AGN accretion discs against fragmentation (see Section 1.5.1), iii) driven by stellar winds, it is a suitable mechanism for the cancellation of angular momentum in nuclear discs (see Section 1.5.3.1), iv) it broadens the distribution of angular momentum in nuclear and circum-nuclear discs (see Section 1.5.3.1) and vi) it could create high density filaments travelling in ballistic trajectories towards the black hole, triggering chaotic accretion (see Section 1.5.3.1). In this Thesis, the main role of turbulence is that of broadening the distribution of angular momentum within a nuclear disc. We hypothesize that, under such circumstances, the broad disc is able to cancel out an important fraction of the angular momentum of a secondary misaligned inflow, promoting a subsequent increase of accreted mass.

To test our hypothesis, we study the disc formation process from gaseous shells rotating around a SMBH and a nuclear gaseous disc. As the gas dynamics of such systems is complex, we resort to numerical modelling, more precisely to smoothed particle hydrodynamics. The remainder of this chapter will be devoted to a short description of the method and the most relevant features implemented for the development of this Thesis.

3

NUMERICAL MODELLING: SPH

Interstellar densities are so low (10^{-4} molecules per $cm^3 - 10^6$ ions per cm^3)[1] and temperatures so comparatively high ($10 - 10^7$K) that the mean free path between the particles conforming the gas are extremely large, rendering viscous forces extremely small. When dealing with most of astrophysical flows, then, the viscous terms in the Navier-Stokes equation (eq. 10) are negligibly small. In the limit $\eta = \zeta = 0$, the Navier-Stokes equation reduces to the Euler equation:

$$\rho\left(\frac{\partial v_i}{\partial t} + v_j\frac{\partial v_i}{x_j}\right) = -\frac{\partial p}{x_i} - \rho\frac{\partial \phi}{\partial x_i}. \tag{24}$$

This is the equation that is solved numerically by most of the hydrodynamical codes available to treat astrophysical problems. However, one disadvantage of such an inviscid equation is that, as discussed in chapter 2, viscosity is indeed relevant for the existence of shocks and turbulence: Two dissipative processes that are highly relevant to the physics of interstellar as well as intergalactic medium. On top of it, even if the desire for solving the full Navier-Stokes equation existed, the scales at which viscosity operates are unreachable by any numerical scheme, as the resolution scales lag several orders of magnitude above them. What is done in SPH to model the macroscopic impact of these microscopic processes is that one introduces an artificial viscosity: A viscous-like term that acts only in the presence of convergent flows, as in shocks. Ideally, this viscosity term is negligible in the presence of shearing flows but some residual is always present. This residual shear artificial viscosity is responsible for dissipating turbulent motions usually at larger scales and shorter timescales than those in which molecular viscosity would act.

In this chapter we describe the SPH numerical scheme for solving the Euler equation (eq. 24), focusing on the implementation of a time dependent artificial viscosity in which a viscous-like term grows in the presence of shocks and decays to small values elsewhere.

1 Compare this with a number density of roughly 10^{19} molecules per cm^3 for air, and 10^{10} molecules per cm^3 for a laboratory high-vacuum chamber.

3.1 SPH EQUATIONS OF MOTION

Consider a set of N SPH particles (i.e. mass elements of fluids) of mass m_i at positions $\vec{r}_i$. The density associated to each of them is calculated according to:

$$\rho_i = \sum_{j=1}^{N_{ngb}} m_j \, W(|\vec{r}_i - \vec{r}_j|, h_i), \tag{25}$$

where $W(r, h)$ is the SPH kernel, a gaussian-like function that drops to zero at $r = h$. The smoothing length, h, is an adaptive quantity and varies in order to keep a constant mass inside the kernel. Each SPH particle has also an internal energy u_i related to its density and its entropy, s_i, by:

$$u_i = \frac{A(s_i)}{\gamma - 1} \rho_i^{\gamma - 1}, \tag{26}$$

where $A(s)$ is the entropic function and can be used to describe the fluid instead of the internal energy or the entropy (Springel & Hernquist 2002). With these quantities we can build a suitable SPH Lagrangian from which to derive the equations of motion:

$$L = \frac{1}{2} \sum_{i=1}^{N} m_i \, |\dot{\vec{r}}_i|^2 - \frac{1}{\gamma - 1} \sum_{i=1}^{N} m_i \, A_i \, \rho_i^{\gamma - 1}. \tag{27}$$

Taking $\vec{r}_i$ and h_i as the independent variables, A_i as constants, the thermal energy as the potential generating the motion of the SPH particles, and asking that the quantity $(4\pi/3) \, h_i \, \rho_i = M_{SPH}$ to be a constant, we obtain the equations of motion of the SPH particles:

$$\frac{d\vec{v}_i}{dt} = - \sum_{j=1}^{N_{sph}} m_j \left[f_i \frac{P_i}{\rho_i^2} \nabla_i W_{ij}(h_i) + f_j \frac{P_j}{\rho_j^2} \nabla_i W_{ij}(h_j) \right], \tag{28}$$

where $P_i = A_i \rho_i^{\gamma}$ is the pressure felt by particle i and the coefficients f_i are defined as:

$$f_i = \left(1 + \frac{h_i}{3\rho_i} \frac{\partial \rho_i}{\partial h_i} \right)^{-1}. \tag{29}$$

3.2 ARTIFICIAL VISCOSITY

The disadvantage of any numerical scheme, and in particular SPH, is that, given the finite resolution, it is a hard task to resolve regions of

the flow in which the thermodynamic quantities of the fluid change in length scales comparable to the mean free path of the fluid (physical) particles, such as shocks. These length scales are unresolvable at the macroscopic scales represented by the sph (computational) particles and one needs to rely on artificial dissipation recipes to treat shocks (Vonneumann & Richtmyer 1950; Caramana et al. 1998; see also reviews by Rosswog 2009 and Price 2012a).

Grid-based codes for supersonic flows are often based on finite volume Riemann-solvers using the Godunov scheme (see e.g. Toro 1997). By their conservative nature, these codes maintain correct shock speeds, and, because of the Riemann-solver approach in calculating fluxes, they maintain very sharp discontinuities across a shock (typically within a few zones). In contrast, most of the astrophysical SPH implementations follow the so called artificial viscosity (AV) scheme in order to overcome this problem.

In an attempt to asses the applicability of different numerical schemes to the modelling of supersonic turbulent flows, Kitsionas et al. (2009) compares the numerical dissipation among several hydro-codes, both particle- (GADGET, PHANTOM, VINE) and grid-based (ENZO, FLASH, ZEUS). They focus on the astrophysical context, studying situations in which he turbulence is purely hydrodynamic (no magnetic fields) and isothermal. In order to do this, they follow the dissipation of kinetic energy within a full developed turbulent flow due to the numerical viscosity, intrinsic to any numerical scheme. The turbulent velocity field is characterized by using volume- and density-weighted velocity power spectra (see discussion in Section 2.3.2). The importance of such a comparison lays in quantifying the importance of artificial viscosity on dissipating kinetic energy at the smallest resolved scales (smallest eddies resolved), rather than to its applicability in modelling shocks –which nowadays is a routine test before even start using a code. What they find is that it is rather a question of resolution than a question of the specific properties of the hydrodynamical code implementation that determines the accuracy on reproducing turbulence scaling relations. By using a similar number of resolution elements, the results thrown by grid- and particle-based codes are in comforting agreement. However, at scales below some resolution elements (they claim 32) important differences arise between implementations. Furthermore, they do find that a time varying artificial viscosity (Morris & Monaghan 1997) in particle-based codes can result in less dissipation. This is important, as we must remind that in supersonic turbulence energy is not only dissipated by viscosity (either numerical or physical) on the smallest scale eddies, but also in shocks. In a similar fashion, Price & Federrath (2010a) compared the statistics of driven, supersonic turbulence at a high Mach number using FLASH and PHANTOM. They find SPH to be more dissipative at comparable numbers of computational elements in statistics of the velocity field, but cor-

respondingly less dissipative than the grid code in the statistics of density-weighted quantities.

On the other hand, in the sub-sonic turbulence regime, Bauer & Springel (2012) argue that the widely employed standard formulation of SPH yields problematic results. Instead of building up a Kolmogorov-like turbulent cascade, large-scale eddies are quickly damped close to the driving scale and decay into small-scale velocity noise. This problematic behaviour is also studied by Price (2012b), who affirms that accounting for the Reynolds number is critical in numerical simulations of turbulence, particularly for subsonic flow. They show that, for smoothed particle hydrodynamics with constant artificial viscosity coefficient α, the effective Reynolds number in the absence of explicit physical viscosity terms scales linearly with the Mach number –in contrast to mesh schemes, where the effective Reynolds number is largely independent of the flow velocity. By employing standard methods for reducing α away from shocks, they manage to recover a turbulent flow with a Kolmogorov spectrum. Both authors agree that SPH's performance is much better for supersonic turbulence, as here the flow is kinetically dominated and characterized by a network of strong shocks, which can be adequately captured by the SPH method.

Artificial dissipation in SPH is implemented by introducing a viscous term to the equations of motion of the form:

$$\left.\frac{d\vec{v}_i}{dt}\right|_{AV} = -\sum_{j=1}^{N_{sph}} m_j \Pi_{ij} \nabla_i \overline{W}_{ij}, \tag{30}$$

where m_k and $\vec{v}_k$ denote the mass and velocity of the k-th sph particle, $\overline{W}_{ij}$ is the arithmetic mean of the two kernels $W_{ij}(h_i)$ and $W_{ij}(h_j)$, h_k is the smoothing length of particle k, and the quantity $\Pi_{ij} \geqslant 0$ must be non zero only when particles approach each other. Ideally, the viscosity should only be present in a hydrodynamic shock, but otherwise it should be negligibly small. For instance, AV should be absent in rigid and shockless differential rotation and, in particular, it should distinguish uniform compression from a shock. These requirements are of particular importance when dealing with (supersonic) turbulence. In such a situation all the aforementioned spurious effects would amount to a poor treatment of the turbulence down to the smallest resolved scales, shortening the decay time-scale by excessive numerical dissipation.

The most popular form of Π_{ij} is the Monaghan-Balsara parametrization (Monaghan & Gingold 1983; Balsara 1995). In GADGET-2 (Springel 2005), a variant of this parametrization is used, based on an anal-

ogy with Riemann solutions of compresible gas dynamics (Monaghan 1997):

$$\Pi_{ij} = \begin{cases} -\frac{\alpha\,\mu_{ij}}{2\,\rho_{ij}}\left(2\,c_{ij} - 3\,\mu_{ij}\right)\,f_{ij}, & \text{if } \vec{v}_{ij}\cdot\vec{r}_{ij} < 0, \\ 0, & \text{otherwise,} \end{cases} \tag{31}$$

with

$$\mu_{ij} = \frac{\vec{v}_{ij}\cdot\vec{r}_{ij}}{|\vec{r}_{ij}|}, \tag{32}$$

c_{ij} and ρ_{ij} the arithmetic means of the sound speed and density between particles i and j, and $\vec{v}_{ij}$ and $\vec{r}_{ij}$ are the relative velocities and separations between those same particles. The strength of the AV is regulated by the parameter $\alpha \sim 1$. To suppress viscosity locally in regions of strong shear flows, the Balsara (1995) viscosity limiter $f_{ij} = (f_i + f_j)/2$ is also included:

$$f_i = \frac{|\langle\nabla\cdot\vec{v}\rangle_i|}{|\langle\nabla\times\vec{v}\rangle_i| + |\langle\nabla\cdot\vec{v}\rangle_i| + \sigma_i}, \tag{33}$$

where $\sigma_i = 0.0001 c_i/h_i$. This viscosity limiter is useful to avoid spurious transport of angular momentum and vorticity, but finds its limitations if shocks develop in shearing environments, such as accretion discs.

In order to reduce α away from shocks, Morris & Monaghan (1997) suggested the use of time-dependent artificial viscosity parameters, a scheme which has been also implemented by e.g. Dolag et al. (2005) and Valdarnini (2011). The main idea is to raise α at non-negligible levels only where it is needed (i.e. a shock), and make it almost zero for the rest of the fluid. Each particle is assigned its own AV parameter, α_i, and let it evolve according to the differential equation:

$$\frac{d\alpha_i}{dt} = -\frac{\alpha_i - \alpha_{min}}{\tau_i} + S_i. \tag{34}$$

Thus, α_i always decays to α_{min} with e-folding time τ, while the source term S_i will make its value raise rapidly when approaching a shock. When dealing with isothermal equations of state, $P = c_s^2\rho$, the decay time-scale is given by (Price & Federrath 2010b):

$$\tau_i = \frac{h_i}{\sigma c_i}, \tag{35}$$

where σ is a non-dimensional free parameter which determines on how many information crossing times the viscosity decays. The source term is implemented as

$$S_i = S_0 \, f_i \max(0, -\nabla \cdot \vec{v}_i), \tag{36}$$

where S_0 is another free parameter [2]. A maximum value for the viscosity parameter is also introduced to keep the viscosity bounded between $\alpha_{min} = 0.02$ and $\alpha_{max} = 1.0$. Whenever we made use of the time dependent artificial viscosity scheme, we set $\sigma = 0.1$, $S_0 = 1.0$.

3.3 GRAVITATIONAL FORCES AND RESOLUTION LIMIT

The equations of SPH are intrinsically fully adaptive, increasing the resolution in areas where density is greater, allowing us to, in principle, resolve arbitrarily high densities. However when the SPH equations are coupled to gravity, resolving higher densities means resolving smaller Jeans masses (i.e. resolving the collapse of smaller regions under their own gravity),

$$M_J = \frac{c_s^3}{\sqrt{G^3 \rho}}, \tag{37}$$

dropping factors ~ 1. Evidently, as SPH particles do not represent point particles but generic parcels of fluid, a minimum number of them must be contained in a given volume in order to speak of the properties of the fluid inside that volume. This number is given by the number of neighbours in the SPH method, $N_{min} = N_{ngb}$. In the same way, for resolving the Jeans mass of some clump of fluid, that clump must be formed by at least N_{ngb} particles. This sets the smallest Jeans mass that can be resolved, given by the minimum number of particles needed to characterize the given region of the fluid multiplied by the mass of the particles. Thus, if we want to resolve a given Jeans mass, M_J, we must reach a mass resolution M_{res} such that:

$$M_J = \frac{c_s^3}{\sqrt{G^3 \rho}} > M_{res} = N_{ngb} \, m_{sph}. \tag{38}$$

Given a mass resolution M_{res}, we will not be able to resolve the collapse of regions with a smaller Jeans mass. This sets a maximum density resolution:

$$\rho_{max} = \frac{c_s^6}{G^3 \, M_{res}^2}. \tag{39}$$

2 One of the happy moments of studying the implementation of the time varying α on P-GADGET was the discovery of a bug in calculating the value S_0. Some months later I had the opportunity to communicate it personally to Klaus Dolag. He appreciated, as he had actually been looking for it.

This in turn sets a volume resolution limit as we must be sure that at any given time the resolved mass M_{res} is contained in a volume not smaller than

$$V_{min} \sim h_{min}^3 = \varepsilon_{min}^3 \sim M_{res}/\rho_{max}, \tag{40}$$

where h_{min} and ε are the minimum hydro-smoothing and gravitational softening lengths to be set in order to avoid spurious effects.

In our simulations, the total number of particles is $N_{sph} \simeq 0.5 - 1 \times 10^6$, $N_{ngb} \simeq 50$ and $c_s \simeq 3\,km\,s^{-1}$ (Corresponding to a temperature $T \simeq 10^3 K$). The mass and length resolution will depend on the mass of the inflow, but in all cases we have $\varepsilon_{min} = h_{min} \leqslant 0.1$ pc.

3.4 IMPLEMENTATION

All the calculations of this Thesis were performed by running GADGET-2 and P-GADGET in the supercomputers SP6 and PLX at CINECA-Bologna, and the HG1 cluster and ULYSSES at SISSA. Both massively parallel TreeSPH codes are capable of following a collisionless fluid with the N-body method, and an ideal gas by means of SPH. The implementation of SPH manifestly conserves energy and entropy in regions free of dissipation, while allowing for fully adaptive smoothing lengths. Gravitational forces are computed with a hierarchical multipole expansion, which can optionally be applied in the form of a TreePM algorithm, where only short-range forces are computed with the 'tree' method while long-range forces are determined with Fourier techniques. Time integration is based on a quasi-symplectic scheme where long-range and short-range forces can be integrated with different time-steps. Individual and adaptive short-range time-steps may also be employed. The domain decomposition used in the parallelization algorithm is based on a space-filling curve, resulting in high flexibility and tree force errors that do not depend on the way the domains are cut. The codes are efficient in terms of memory consumption and required communication bandwidth. For a deeper discussion on the algorithms and their implementation see the GADGET-2 paper by Springel (2005).

Part II

ANGULAR MOMENTUM CANCELLATION WITHIN GALACTIC NUCLEI

4

OVERLAPPING INFLOWS AS CATALYSTS OF SMBH GROWTH

In this chapter, numerical simulations are presented in which a rotating gaseous shell flows towards an SMBH because of its lack of rotational support. As inflow proceeds, gas from the shell impacts an already present circumnuclear disc. The cancellation of angular momentum and redistribution of gas is studied in this scenario. The work presented in this chapter has been published by Carmona-Loaiza et al. (2014).

4.1 INITIAL CONDITIONS

The physical system under study consists of a gaseous disc rotating around a central black hole and a gaseous shell initially surrounding both the black hole and the disc. The whole system is embedded in a spherical bulge. We follow the hydrodynamics of the gas using the three dimensional SPH/N-body code developed by Springel (2005), GADGET-2. We use $N_{disc} = N_{shell} = 0.5 \times 10^6$ SPH particles of mass $m_{part} = 100 M_\odot$ for modelling the disc and shell respectively (i.e. the total number of SPH particles is $N_{tot} = 10^6$). The smoothing lengths are fully adaptive, giving a smallest resolvable scale of $h_{min} = 2.8 \times 10^{-2}$ pc. The number of SPH neighbours was fixed at $N_{neigh} = 40$.

The black hole, at the relevant scales for our study, can be safely modelled as a Keplerian potential. We follow Hobbs11 for setting up the scenario in which the gas evolves. The background potential is fixed to be that of an isothermal non-singular sphere with core radius r_{core}. Superimposed is the Keplerian potential of a central black hole of mass M_{BH}. For this model, the mass enclosed within radius r is given by:

$$M(r) = M_{BH} + \begin{cases} M_{core}(r/r_{core})^3, & r < r_{core} \\ M_{bulge}(r/r_{bulge}), & r \geqslant r_{core}, \end{cases} \tag{41}$$

with $r_{bulge} = 1$ kpc and $M_{bulge} = 10^{10} M_\odot$ being the characteristic length and mass scale for the spherical bulge. We use these as the units for our code. Accordingly, $M_{core} = 2 \times 10^{-2}$, $M_{BH} = 10^{-2}$; $r_{core} = 2 \times 10^{-2}$. The unit of time is defined as $T_u = (r_{bulge}^3 / G M_{bulge})^{1/2} \simeq 5$ Myr, and the velocity is in units of $V_u \simeq 208\,\mathrm{km\,s^{-1}}$. In these units the minimum smoothing length of the SPH particles $h_{min} = 2.8 \times 10^{-5}$ and the gravitational constant is automatically set $G = 1$.

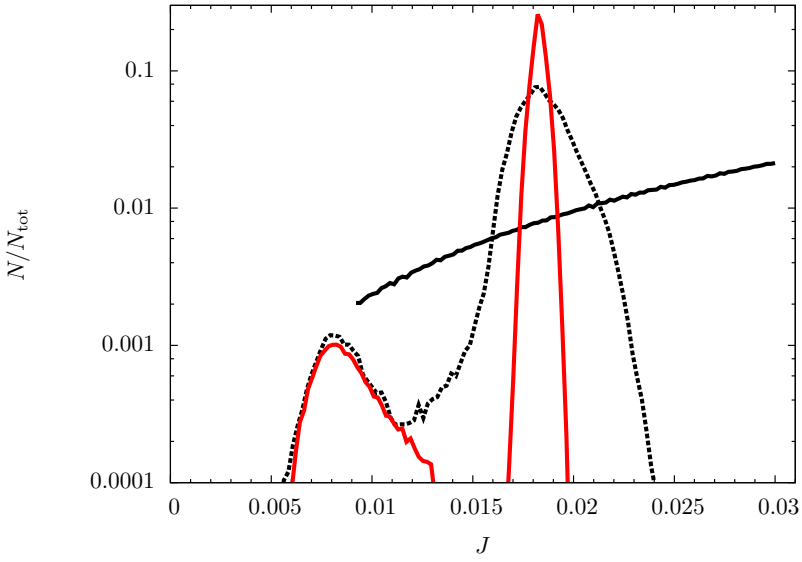

Figure 1: Evolution of the distribution of the specific angular momentum moduli of the shell particles which will evolve into the primitive disc. The initial condition (solid black line) being that of a uniform shell rotating around the z axis. The black dotted line and the red line correspond to $t = 0.15$ and $t = 0.5$ respectively.

The mass of the black hole, together with the mass distribution given by equation (41) are not active components of the simulation in the sense that they just set the background potential in which the gas is moving and do not change in time.

The self-gravity of the gas is neglected, so that the interaction among gas particles is purely hydrodynamical. Cooling has been modelled with an isothermal equation of state as we expect the cooling time scale to be much shorter than the dynamical time scale of the simulations (e.g. Hopkins & Quataert 2010a; Thompson et al. 2005). We also set up an accretion radius, r_{acc}, such that every particle that comes inside that radius with low enough orbital energy and angular momentum is regarded as *eventually accreted* and is immediately removed from the simulation. The accretion radius is, in code units, $r_{acc} = 10^{-3}$, corresponding to one parsec in physical units. This accretion radius approach is often implemented for sink particles in star formation simulations (see Bate et al. 1995). Gas particles forming the shell are distinguished from particles forming the disc by adding a different tag to each set of particles, and we keep a record of the number of accreted particles to compute the accretion rate and make a comparison among the different simulations.

The system under study consists of a primitive gaseous disc of size ~ 16 pc around the central black hole, plus a spherical shell gas cloud

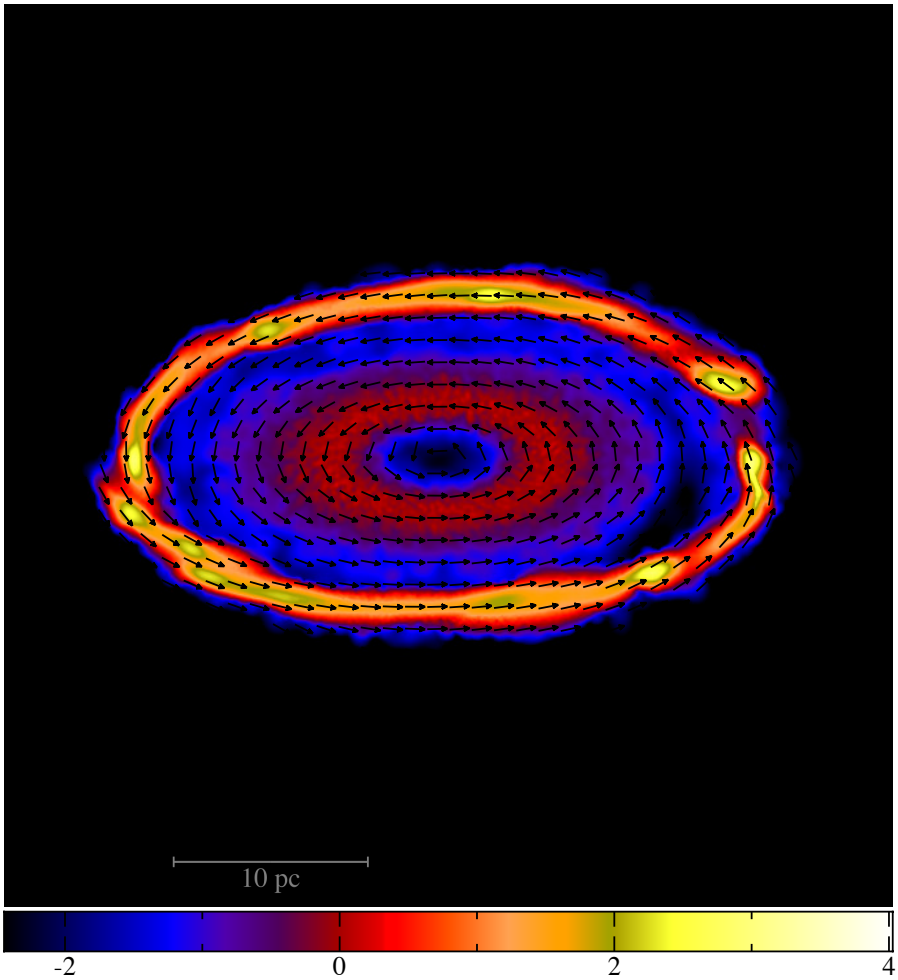

Figure 2: Disc that forms after $t = 0.5$ of the evolution of a rotating homogeneous gaseous shell. This disc is the inner primitive disc used for the initial conditions in all our simulations. The colour map shows $\log \Sigma$ in code units, where Σ is the projected column density. The arrows are not representative of the velocity profile, they just illustrate the flow direction.

of size ~ 100 pc centred also at the black hole, the two immersed in the galactic bulge + BH potential of equation (41). The inner disc is rotating in a stable configuration, while the shell is initially set into rotation with a cylindrical velocity profile, not in virial equilibrium. The shell will start collapsing toward the central black hole due to the action of gravity and will interact with the disc.

The primitive disc is generated following Hobbs11, simulating the collapse of an initially rotating spherical gaseous shell to mimic the evolution and outcome of an earlier accretion event (hereafter we relax the meaning of "accretion" to a generic inflow of gas towards r_{acc}). We carve a spherical shell of 0.5×10^6 SPH particles from a cube of glass-like distributed particles, as this reduces the noise in the pressure force in SPH particles (see e.g. Diehl et al. 2012; Price 2012b). The mass of the shell, $M_{shell} = 5.1 \times 10^{-3}$, is distributed homogeneously from $r_{in} = 0.03$ to $r_{out} = 0.1$ and is set into rotation around the z axis with a cylindrical velocity profile $v_{rot} = 0.3$.

The unstable shell is allowed to evolve under the gravitational influence of the potential described in equation (41). We stress that the velocity profile, together with the density profile are idealized in order to capture the physics of the problem and to avoid unnecessary computational expense.

The rotating gas shell, falling towards the centre, evolves into a disc-like structure. In the first stages, the angular momentum has a quite flat distribution (Figure 1). As the gas starts mixing, angular momentum is transported among the particles and, due to the symmetry of the problem, the x and y angular momentum components cancel out. At $t = 0.5$, the gas has already settled into a stable disc-like structure rotating around the centre of the potential. As angular momentum is conserved, $\mathbf{J}_{disc}$ points in the z direction, with a modulus $J_{disc} = 0.018$ (in code units). Figure 2 shows the state of the gas at this time, in circular orbits at a radius $r_{circ} \simeq 0.016$ (16 pc in physical units). The gas has undergone an *angular momentum redistribution shock* (in agreement with figures 1 and 5 from Hobbs11). The final configuration, as noted by Hobbs11, is closer to a ring rather than a disc. For simplicity we will refer to this structure as primitive disc.

Once the disc is formed in the first place, we superimpose a new gaseous shell, replica of the pristine shell, this time adding a tilt to it and varying its initial v_{rot}. This shell mimics a second accretion event, uncorrelated with the first one. Hereafter, v_{rot} will denote the initial rotational velocity of the second shell infalling toward the central black hole, and θ_{tilt} the initial angle between the disc and shell total angular momentum vectors, denoted as $\mathbf{L}_{disc}$ and $\mathbf{L}_{shell}$ respectively.

We explore six different cases, resulting from scenarios in which the infalling shell has a smaller, equal and greater angular momentum than that of the disc combined with its two possible senses of rotation

(co- or counter-rotation) with respect to the disc. We build each of these scenarios by setting the initial shell $\nu_{rot} = 0.2, 0.3, 0.7$ and a tilt angle $\theta_{tilt} = 60°, 150°$. This will enable us to asses the impact of the sense of rotation and angular momentum on the dynamics of the composite system. The simulations are run for more than 10 dynamical times measured at $r = r_{core}$, and throughout them, the accreted mass is $M_{acc} < 0.1 M_{sys}$ even for the most active event, so we will regard M_{disc}, M_{shell} and the total mass of the system M_{sys} as constants.

In the following we introduce the specific angular momentum of each SPH-particle, $\mathbf{j}_i = \mathbf{r}_i \wedge \mathbf{v}_i$, and the total specific angular momentum of the disc,

$$\mathbf{J}_{disc} = \frac{1}{N_{disc}} \sum_{i=0}^{N_{disc}} \mathbf{j}_{i,disc} \, , \tag{42}$$

with modulus J_{disc}. We remark that initially the primitive disc has $J_{disc} = 0.018$ (in code units) in all simulations. Similar notation is used to distinguish and describe the shell particles.

In addition we introduce the mean angular momentum,

$$\langle j_{disc} \rangle = \frac{1}{N_{disc}} \sum_{i=0}^{N_{disc}} j_{i,disc} \, , \tag{43}$$

for the disc particles, with an equivalent definition for the shell particles describing the angular momentum content of each component of the system in terms of the moduli $j_i = |\mathbf{j}_i|$.

4.2 THE SIMULATIONS

Figures 3, 4 and 5 show four different stages in the evolution of the disc+shell simulated systems, from the beginning to the new final state of equilibrium after interaction has subsided. In all the six cases, the shell is initially collapsing to form a disc from the inside out, as particles with lower angular momentum (i.e. smaller circularization radius) fall first. These particles will be the first to interact with the primitive disc. Mixing of shell and disc particles occurs with different strength depending on ν_{rot} and θ_{tilt}. We describe the final fate of each system separately in the following subsections. For sake of clarity, we take $t = 0$ as the time the second shell starts falling towards the previously formed disc. In all the cases, the shell particles are exterior to the primitive disc, at the time of initial infall [1].

1 Videos of the simulations can be found at http://people.sissa.it/~jcarmona/my_videos.php. The snapshots shown in the paper are made using SPLASH (Price 2007).

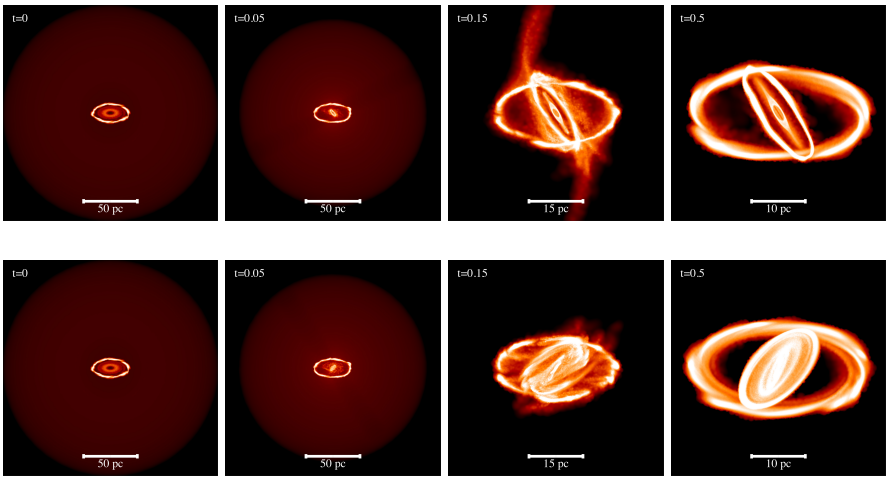

Figure 3: Evolution of nested accretion events with $J_{shell} < J_{disc}$, corresponding to $\nu_{rot} = 0.2$. The upper and lower rows correspond to shell initial tilt angles of $\theta_{tilt} = 60°$ and $150°$, respectively. From left to right, the time at which snapshots are taken are $t = 0, 0.05, 0.15, 0.5$. See text for details. Note the change of scale between the different snapshots: 50 pc in the first two, 15 pc and 10 pc in the last two.

4.2.1 *Smaller angular momentum event:* $J_{shell} < J_{disc}$

We first consider a shell with $\nu_{rot} = 0.2$, corresponding to $J_{shell} = 0.012 < J_{disc}$. Under these initial conditions the shell has less rotational support against gravity than the shell that gave rise to the primitive disc. If the primitive disc were not present, the outcome of these two simulations would be a tilted copy of the primitive disc, this time with tighter orbits. We next describe the evolution for the shell having $\theta_{tilt} = 60°$ and $\theta_{tilt} = 150°$.

4.2.1.1 *Co-rotating shell,* $\theta_{tilt} = 60°$

Figure 3 shows the evolution of the system into a configuration of nested discs. First the shell stops falling and two arms develop due to the shell particles impinging on the primitive disc at an angle. We notice that these arms do not develop in the other simulations, meaning that they form due to the high density flows from the shell that impact the lower density inner regions of the primitive disc, kicking the gas in wider orbits that are observed as arms. However, this is just a transient signature, as the arms completely disappear after less than two orbits, leaving two tilted discs with a ring like structure each, the innermost one rotating in the sense of the shell.

4.2.1.2 *Counter-rotating shell,* $\theta_{tilt} = 150°$

In the counter-rotating case depicted in Figure 3, the shell starts falling toward the centre and very rapidly forms an inner tiny dense disc.

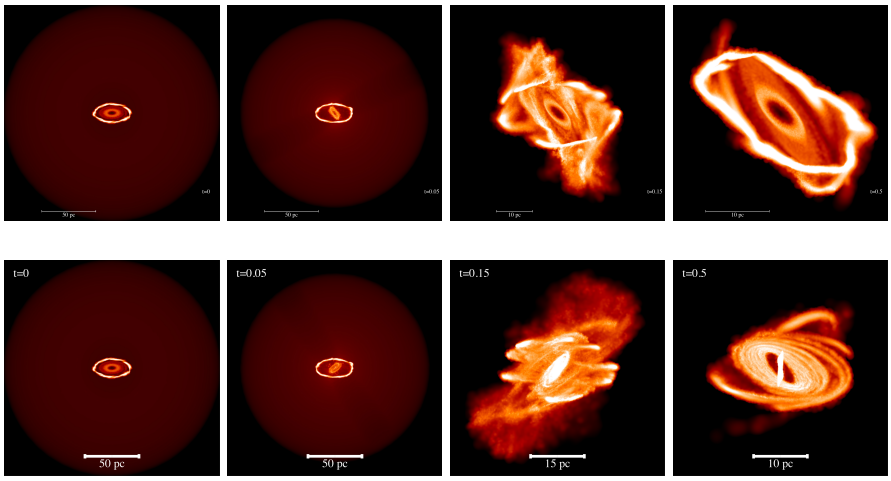

Figure 4: Evolution of nested accretion events with $J_{shell} = J_{disc}$, corresponding to $v_{rot} = 0.3$. The upper and lower rows correspond to shell initial tilt angles of $\theta_{tilt} = 60°$ and $150°$, respectively. From left to right, the time at which snapshots are taken are $t = 0, 0.05, 0.15, 0.5$. See text for details. Note the change of scale between the different snapshots: 50 pc in the first two, 15 pc and 10 pc in the last two.

The shell drags in its way some gas from the primitive disc. After that, the tiny disc starts twisting and soon a very tight spiral pattern develops, forming a wider disc that extends from the centre to some region inside the primitive disc. This disc develops a wider structure (as opposed to the two ring-structure formed in the previous case) due to the interaction of opposite flows. As gas from the shell was falling, it started breaking via shocks with gas from the disc, giving to the particles a wide spectrum of angular momenta and thus, making them able to form an inner counter-rotating disc and a ring-like outer disc comprising most of the particles of the primitive disc.

4.2.2 *Equal angular momentum event:* $J_{shell} = J_{disc}$

We now consider the case of an outer shell with an initial velocity $v_{rot} = 0.3$ (Figure 4), corresponding to a total angular momentum per unit mass $J_{shell} = J_{disc} = 0.018$. Under these conditions, the shell interacts with the pristine disc that, before forming, had the same initial angular momentum distribution and mass content.

4.2.2.1 *Co-rotating shell,* $\theta_{tilt} = 60°$

The first row of Figure 4 shows the evolution of the system in which the shell co-rotates relative to the disc with $\theta_{tilt} = 60°$. Shell particles crossing the plane orthogonal to $\mathbf{L}_{shell}$ from above interact via shocks with shell particles crossing from below, simultaneously interacting with the disc formed in the first accretion event. Those particles that

lost angular momentum via shocks would flow toward the centre of the potential. However, the interaction with the primitive disc favours the formation of an inner tilted disc that would not have formed otherwise. This occurs at about a time $t = 0.05$. As the shell continues to infall, the innermost recently formed disc remains unaffected. The remaining shell particles start forming a new disc that would evolve into a copy of the primitive disc if the latter were not present. At $t = 0.15$, the shell stops infalling and forms a disc-like structure tilted at $\sim 60°$ with respect to the primitive disc. The interaction at this point becomes very violent, the gas from both accretion events is shock-mixed and starts oscillating around a plane tilted at $30°$ with respect to the $x - y$ plane of the primitive disc, until a state of equilibrium is reached at around $t = 0.5$. The gas now settles quietly into a disc-like configuration of radius ~ 10 pc with an angular momentum distribution peaked at around 30°, as described in section 4.3.2.1. Memory is lost of the previous orientations of the disc and shell.

4.2.2.2 *Counter-rotating shell,* $\theta_{tilt} = 150°$

Consider now the case of a shell with rotation axis tilted by $\theta_{tilt} = 150°$ relative to $\mathbf{J}_{disc}$. The interaction between the two flows soon develops an inner dense disc rotating in the sense of rotation of the shell. Contrary to the co-rotating equal-angular-momentum case, at $t = 0.05$, this inner disc continues growing until $t \sim 0.15$. This is due to the cancellation of angular momentum between the events: shell particles that would otherwise remain on larger orbits (in absence of the primitive disc) are braked into tighter orbits, adding mass to the inner disc. This example is considerably more violent than the previous one, and the outcome is a complex structure: a very tight and dense disc orbiting the black hole in an orbit almost coplanar with the $y - z$ plane (i.e. tilted $\sim 90°$ relative to $\mathbf{J}_{disc}$), a larger disc mainly formed by particles from the primitive disc and a tail of shell particles counter-rotating and tilted (relative to $\mathbf{L}_{disc}$) by $\sim 140°$. In addition we note the presence of a spiral pattern in the bigger disc rotating around the z axis.

4.2.3 *Larger angular momentum event:* $J_{shell} > J_{disc}$

To build this case, we set an initial $v_{rot} = 0.7$ for the shell corresponding to an angular momentum per unit mass $J_{shell} = 0.042 > J_{disc}$. If the primitive disc were not present, the outcome of these two simulations would be a tilted copy of the primitive disc with wider orbits (with an averaged circularization radius $r_{circ} \sim 0.04$).The evolution of these cases is shown in Figure 5.

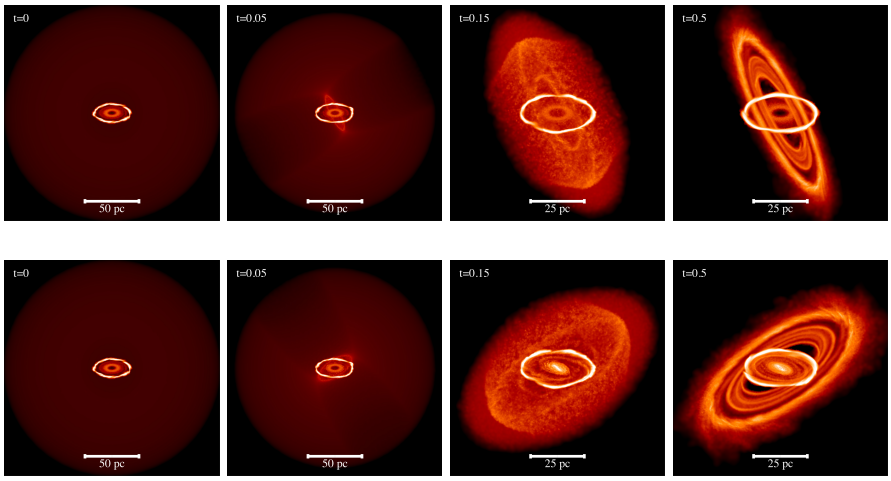

Figure 5: Evolution of nested accretion events with $J_{shell} > J_{disc}$, corresponding to $v_{rot} = 0.7$. The upper and lower rows correspond to shell initial tilt angles of $\theta_{tilt} = 60°$ and 150°, respectively. From left to right, the time at which snapshots are taken are $t = 0, 0.05, 0.15, 0.5$. See text for details.Note the change of scale between the different snapshots: 50 pc in the first two and 25 pc in the last two.

4.2.3.1 *Co-rotating shell*, $\theta_{tilt} = 60°$

The evolution of this larger angular momentum shell with $v_{rot} = 0.7$ and tilted at $\theta_{tilt} = 60°$ is rather simple. The angular momentum of almost all of the gas forming the shell is large enough for particles to remain in wide orbits and leave the primitive disc unaffected. The final configuration is the superposition of the primitive disc and a larger co-rotating disc formed from shell particles and tilted at the same tilt angle that the shell initially had. The evolution is illustrated in Figure 5.

4.2.3.2 *Counter-rotating shell*, $\theta_{tilt} = 150°$

Under these conditions, the shell carries a larger angular momentum than the primitive disc and is counter-rotating. One would expect to observe in this case an evolution similar to the previous case, i.e. the formation of an outer, counter- rotating disc misaligned relative to the inner, unperturbed disc. However, Figure 5 shows a different evolution. As the disc forms from the inside out, the infalling shell particles with lower angular momentum try to form a counter-rotating disc of size comparable to that of the primitive disc. Cancellation of angular momentum causes these particles to move further inwards changing also their sense of rotation. An inner denser disc in co-rotation forms that can be identified as a density enhancement at the centre of the last two snapshots shown in the bottom right panels of Figure 5. The shell particles with larger angular momentum settle into a larger, counter-rotating disc which surrounds the inner co-rotating disc.

In the next section we explore the evolution of the angular momentum of the gas particles in a quantitative way, to explain the observed outcomes more thoroughly.

4.3 ANGULAR MOMENTUM EVOLUTION

In the previous section we showed how the infalling shell perturbs the primitive disc, and how the system settles into a new stationary state after a violent interaction. To assess the reciprocal influence of the two flows it is necessary to have a quantitative understanding of the evolution of the angular momentum of the composite system and for each component separately. To this purpose, we keep track of the specific angular momentum distribution of the gas during the simulations, as this allows us to compare the rotational support of each component of the system against the potential in which it is immersed.

In the analysis of the simulated data, we observe angular momentum cancellation in some fraction of the gas for the cases in which the second accretion event is in counter-rotation, a change in the flow direction for the equal angular momentum co-rotating case and an almost null impact for the larger angular momentum co-rotating case. As shown in Figures 3, 4 and 5, there are some cases in which, after mixing, the flows merge into a single disc, some others in which the equilibrium state is formed by nested disc-like structures and some others in which less regular structures develop. To better understand the structures formed by the gas we compute a quantity which will give us information about the sense of rotation of each part of the flow,

$$S(\theta) = \frac{1}{N_{\text{part}}} \sum_{i=1}^{N_{\text{part}}} \Theta(\hat{l}_i \cdot \hat{u}_\theta), \tag{44}$$

where $\hat{l}_i$ points in the direction of the angular momentum of the particle i, $\hat{u}_\theta = \sin(\theta)\,\hat{\mathbf{i}} + \cos(\theta)\,\hat{\mathbf{k}}$ is a unit vector pointing in the direction given by the θ angle in the zx plane and the function $\Theta(\hat{l}_i \cdot \hat{u}_\theta) = 1$ when $\hat{l}_i$ is within one degree of $\hat{u}_\theta$ and $\Theta(\hat{l}_i \cdot \hat{u}_\theta) = 0$ otherwise. Thus $S(\theta)$ is the fraction of gas whose angular momentum points within one degree of the direction of θ.

A narrow peak in the function $S(\theta)$ corresponds to a well defined plane of rotation for the gas. Thus, if a sizeable fraction of gas particles clusters around a specific value of $S(\theta)$ and the distribution of the angular momentum moduli is relatively broad, the configuration corresponds to a *planar disc*. A broad $S(\theta)$ refers instead to a broad distribution of the angular momentum orientation and the configuration can be referred to as a *warped disc*. In this case, the distribution of angular momenta is expected to be wide. A *ring* would correspond to

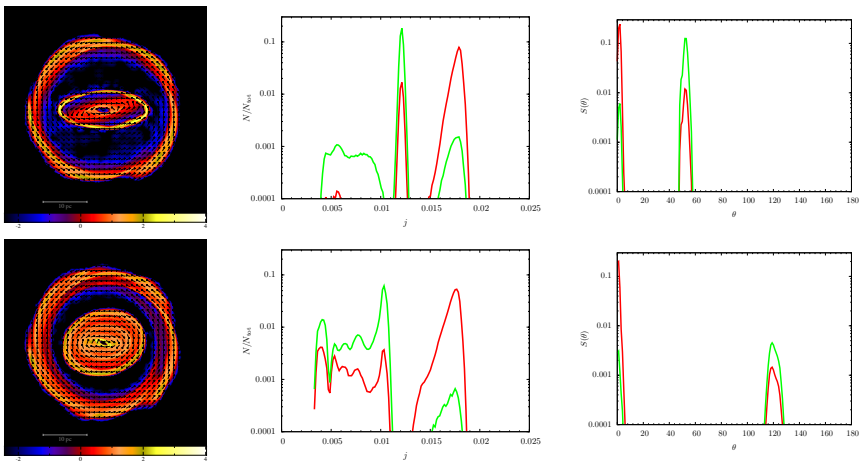

Figure 6: Final state of the nested accretion events with $J_{shell} < J_{disc}$, corresponding to $\nu_{rot} = 0.2$. The upper and lower rows correspond to shell initial tilt angles of $\theta_{tilt} = 60°$ and 150°, respectively. The left column shows colour coded maps of $\log \Sigma$ in code units, where Σ is the projected column density, with arrows indicating the sense of rotation of the flow. The middle column shows the distributions of the angular momentum moduli for the disc (red lines) and shell (green lines) particles, while the right column shows plots of $S(\theta)$ for the disc (red) and shell (green) particles. The scale length bar in the left panels is 10 pc size.

a narrow distribution for j (i.e. the specific angular momentum modulus) with the function $S(\theta)$ peaking around a particular angle. The analysis of the equilibrium states is illustrated in Figures 6, 7 and 8, where we give the colour coded density map of the final structure (viewed at angles chosen to appreciate the details), the distribution of the specific angular momentum moduli of disc (red) and shell (green) particles, and the function $S(\theta)$ again for disc and shell particles.

4.3.1 *Lower angular momentum event:* $J_{shell} < J_{disc}$

In this case, gas particles belonging to the shell pass through the ring before reaching their circularization radius, interacting with the disc and and then leaving it. This leads to the redistribution of the angular momentum depicted in Figure 6.

4.3.1.1 *Co-rotating shell,* $\theta_{tilt} = 60°$

The upper central panel of Figure 6 shows the specific angular momentum distribution among disc and shell particles after the interaction, at $t = 0.5$. We observe two peaks and one broader region in the distribution. The first peak lies at $j = J_{disc} = 0.018$, and is formed by disc particles and by some smaller amount of shell particles which have been captured during the interaction; the second peak lies at

$j = J_{shell} = 0.012$ and is predominantly formed by shell particles, although there is also a non-negligible amount of disc particles. These disc particles were not there before the interaction, which means that they have been dragged there by the infalling shell particles. The third interesting region is located between $j \simeq 0.005$ and $j \simeq 0.009$ and is broader and less dense. It is formed by shell particles that have exchanged angular momentum with disc particles that experience an outward drag, rather than an inward one. From the angular momentum distribution, we describe the structure as a lower density disc surrounded by two ring-like structures.

The top right panel of Figure 6 for $S(\theta)$ highlights the presence of two well defined peaks, meaning that the structures that result from the interaction are planar. One is rotating in the plane of the primitive disc, and the other one is rotating at $\theta \simeq 50°$, and comprises the inner ring and innermost disc. The two peaks have almost equal height and inverted proportions of the mix between disc and shell particles.

4.3.1.2 *Counter-rotating shell,* $\theta_{tilt} = 150°$

This case is shown in the lower row of Figure 6. The distribution shown is the result of a rather violent interaction in which a significant amount of gas from both the shell and the disc is dragged all the way down to the accretion radius. We observe two populated regions: The first one, a broad inner region extending from $j \simeq 0.004$ to $j \simeq 0.01$, is a mix between disc particles and a greater amount of shell particles. The outer peak, even if still at $j = J_{disc} = 0.018$, has widened, and is composed by a mix of particles belonging to the two components of the system with a greater proportion of disc particles. The lower right panel shows $S(\theta)$ displaying two peaks, the first one at $\theta \simeq 0°$ and the second, shorter and broader, at $\theta \simeq 120°$. The first peak has a major proportion of disc particles, while the opposite is true for the second peak. The tilted shell shifts to a lower tilt angle and a significant amount of disc particles end in the inner disc which is counter-rotating relative to the primitive disc, being dragged by the interaction with shell particles.

4.3.2 *Equal angular momentum event:* $J_{shell} = J_{disc}$

In this accretion event the orbits of shell particles will circularize at a radius equal to the radius of the primitive disc, thus, it is expected that gas belonging to the shell will strongly interact with the primitive disc.

4.3.2.1 *Co-rotating shell,* $\theta_{tilt} = 60°$

The upper row of Figure 7 shows the angular momentum distribution and $S(\theta)$ at $t = 0.5$, when the system has reached a state of station-

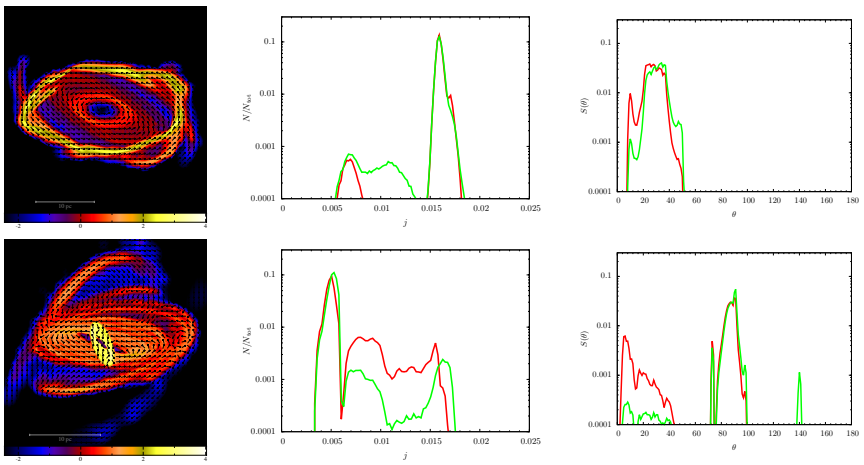

Figure 7: Final state of the nested accretion events with $J_{shell} = J_{disc}$, corresponding to $\nu_{rot} = 0.3$. The upper and lower rows correspond to shell initial tilt angles of $\theta_{tilt} = 60°$ and 150°, respectively. The left column shows colour coded maps of $\log \Sigma$ in code units, where Σ is the projected column density, with arrows indicating the sense of rotation of the flow. The middle column shows the distributions of the angular momentum moduli for the disc (red lines) and shell (green lines) particles, while the right column shows plots of $S(\theta)$ for the disc (red) and shell (green) particles. The scale length bar in the left panels is 10 pc size.

ary equilibrium. The disc particle distribution now peaks at $j \sim 0.016$, implying that $\sim$ 10% of the specific angular momentum content has been cancelled during the interaction. Although the angular momentum distribution has not been severely affected, the gas mixing have changed the original plane of rotation: After the shell started infalling, shell particles tried to settle into circular orbits at the radius where the primitive disc was located. These particles kicked the disc particles at an angle $\theta_{tilt} = 60°$ with a speed roughly equal to the speed the disc particles had, killing in the interaction the normal component of their relative velocity while preserving the parallel component, tilted in this case at $\theta_{tilt}/2 = 30°$ with respect to the z axis. Thus, what we observe in the end is a disc tilted at $\theta_{tilt} = 30°$. The surface density distribution (upper left panel) is non homogeneous through this disc-like structure that shows some degree of warping.

4.3.2.2 *Counter-rotating shell*, $\theta_{tilt} = 150°$

The angular momentum loss in this case is greater than in the previous one. Particles from the shell start falling toward the disc, trying to settle into circular orbits at the same radius of the disc, but contrary to the previous case, the second accretion event is now in counter-rotation, leading to an almost head-on collision between the flows and cancelling out a large amount of their angular momentum. The final distribution of angular momentum, shown in the lower mid

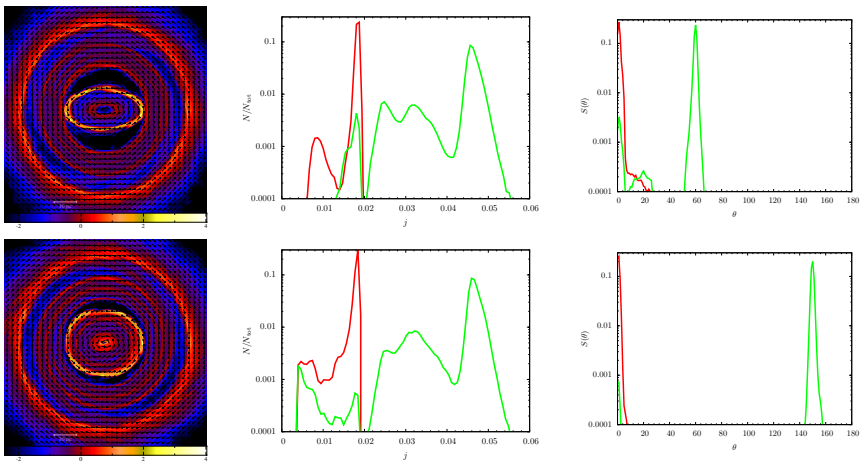

Figure 8: Final state of the nested accretion events with $J_{shell} > J_{disc}$, corresponding to $\nu_{rot} = 0.3$. The upper and lower rows correspond to shell initial tilt angles of $\theta_{tilt} = 60°$ and $150°$, respectively. The left column shows colour coded maps of $\log \Sigma$ in code units, where Σ is the projected column density, with arrows indicating the sense of rotation of the flow. The middle column shows the distributions of the angular momentum moduli for the disc (red lines) and shell (green lines) particles, while the right column shows plots of $S(\theta)$ for the disc (red) and shell (green) particles.The scale length bar in the left panels is 10 pc size.

panel of Figure 7, is broad and extends down to the accretion radius, implying a complete mixing of the two flows. The peak of the angular momentum of disc particles has decreased from $j = 0.018$ to $j = 0.005$, which means that there has been a huge net cancellation of angular momentum.

The lower right panel of Figure 7 shows three main planes of rotation: one at $\sim 90°$, corresponding to gas that has interacted the most, forming in the end a dense disc in tight orbits around the centre (see figure 4). This disc contains gas from both components of the system in almost equal proportions. The second plane of rotation, at $\sim 140°$, corresponds to gas initially belonging to the shell that presumably fell last, when the major part of the interaction had already happened and most of the gas had already gone into smaller orbits. This gas is observed in the left lower panel as an irregular tail orbiting the black hole. The last structure rotates between 0 and $\sim 40°$ and is mainly composed of particles initially belonging to the primitive disc.

4.3.3 *Larger angular momentum event:* $J_{shell} > J_{disc}$

In this case, shell particles have a bigger circularization radius than the radius of the primitive disc, thus we expect a less violent mixing, as shown in figure 8.

4.3.3.1 *Co-rotating shell*, $\theta_{\rm tilt} = 60°$

The top row of Figure 8 shows the result for this case in which very low amount of mixing occurs. The primitive disc is barely affected. It acts as an obstacle for low angular momentum shell particles, trapping and assimilating some fraction of them as part of the original disc. As illustrated in the top right panel, the main planes of rotation of both flows remain practically unaffected.

4.3.3.2 *Counter-rotating shell*, $\theta_{\rm tilt} = 150°$

In this case, the interaction of shell particles with the primitive disc during the inside out formation of the secondary disc causes a fraction of shell particles to co-rotate with the disc, as illustrated in the bottom central and right panels of Figure 8. There exist a region of particles populated at low j indicating that an inflow is present across the inner boundary. The angular momentum orientation highlights the presence of two clear orbital planes: one tilted by 150° and one at 0°, corresponding to the primitive disc with a small amount of shell particles.

In summary, we have seen that all second accretion events with equal or smaller angular momentum content than the first one are capable of altering the angular momentum distribution of the system significantly. In the other hand, the interaction between the disc and higher angular momentum shells leaves the angular momentum distribution of each constituent of the system basically unaltered.

4.4 ANGULAR MOMENTUM CONSERVATION

In the last section it was shown that events in counter-rotation modify the angular momentum distribution of the system more than events in co-rotation, in particular when the angular momentum of the shell and of the primitive disc are comparable, initially. In table 1 we assess this behaviour quantitatively by computing the angular momentum loss in each case for the disc, the shell, and the disc+shell composite system. We observe that counter-rotating infalling shells can cancel out up to 75% of the angular momentum in each component of the system, thus catalysing significantly the inflow towards the accretion radius. Co-rotating events are not as effective, as they can just induce an angular momentum cancellation of less than 15%. If the angular momentum content of the shell is large compared to that of the disc, the amount of gas mixing between the shell and the disc is so small that the angular momentum loss is of less than 6%.

The angular momentum loss of the system as a whole is due to the loss of mass through the accretion radius, that is higher for the equal angular momentum counter-rotating events.

Table 1: Angular momentum lost, L_{lost}, after the interaction of the shell with the primitive disc. v_{rot} denotes the rotational velocity of the shell, and θ_{tilt} the tilt angle between $\mathbf{L}_{disc}$ and $\mathbf{L}_{shell}$. L_{lost} for the system should be zero, however, in our simulations a net mass loss is present due to inflow.

v_{rot}	θ_{tilt}	flow	% L_{lost}
0.2	60°	disc	7.7
0.2	150°	disc	31
0.3	60°	disc	13
0.3	150°	disc	75
0.7	60°	disc	1.1
0.7	150°	disc	5.5
0.2	60°	shell	2.9
0.2	150°	shell	47
0.3	60°	shell	14
0.3	150°	shell	74
0.7	60°	shell	0.77
0.7	150°	shell	2.4
0.2	60°	system	0.28
0.2	150°	system	1.1
0.3	60°	system	< 0.1
0.3	150°	system	4.6
0.7	60°	system	< 0.1
0.7	150°	system	< 0.1

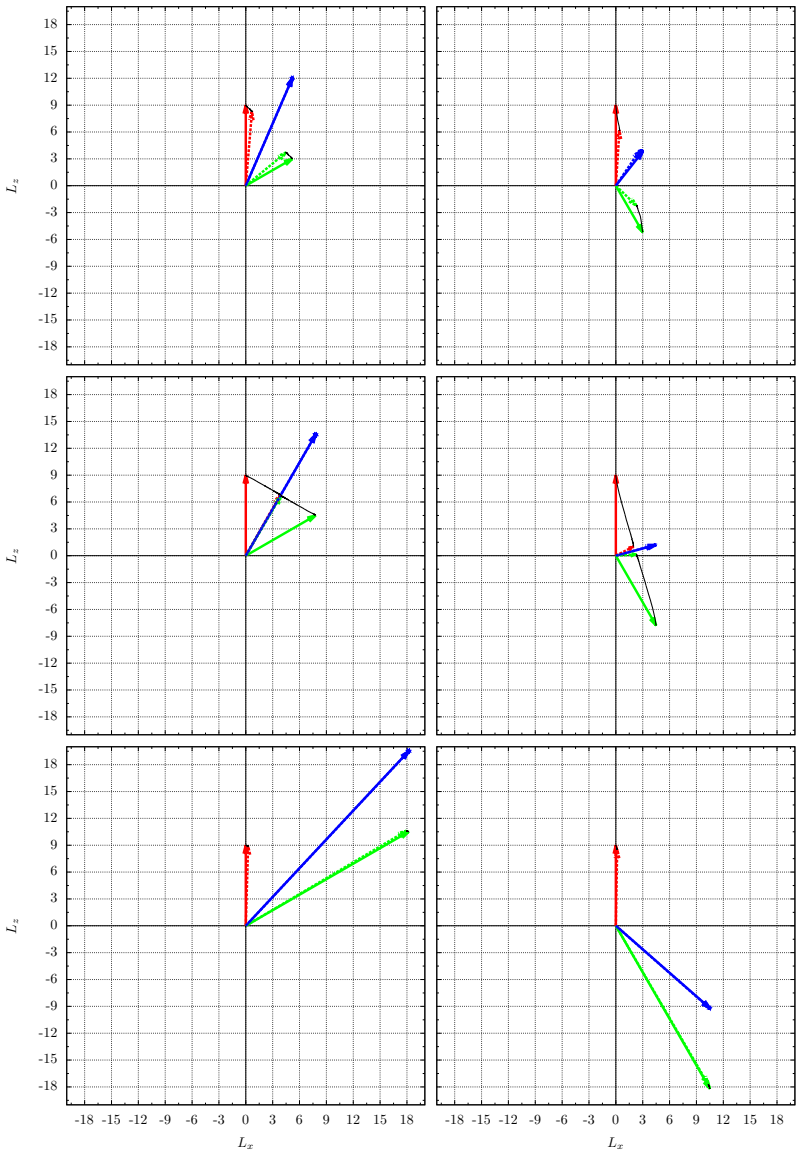

Figure 9: Initial (continuous arrows) and final (dashed arrows) states of the angular momentum for each component of the system: Disc (red arrows) and Shell (green arrows). The total angular momentum of the system is also shown (blue arrows). Each row corresponds to different shell angular momentum content, from top to bottom, $v_{rot} = 0.2, 0.3, 0.7$, while the left and right columns correspond to the shell tilt angle $\theta_{tilt} = 60^\circ$ and 150° respectively. In al cases $L_y = 0$. L_x and L_z are in units of $2.08 \times 10^7 M_\odot \, km \, s^{-1}$ kpc.

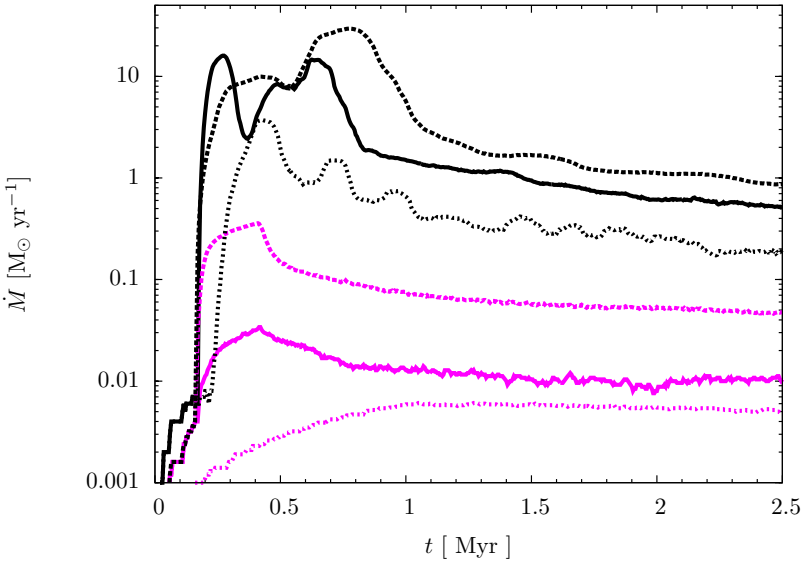

Figure 10: Inflow rate (in units of $M_\odot\,yr^{-1}$) versus time (in Myr) for each case of this study. The lines, from bottom to top, represent the following cases of initial (v_{rot}, θ_{tilt}) : $(0.7, 60°)$ short dashed magenta line; $(0.3, 60°)$ magenta solid line; $(0.2, 60°)$ long dashed magenta line; $(0.7, 150°)$ short dashed black line; $(0.3, 150°)$ black solid line; $(0.2, 150°)$ long dashed black line.

Figure 9 shows the angular momentum of each constituent of the system at the beginning and at the end of the interaction. It makes clear how dramatically the angular momentum is altered for the cases in which the shell and the disc have the same amount of angular momentum ($v_{rot} = 0.3$). In these cases the interaction succeeds in significantly modifying the angular momentum modulus and orientation of both the shell and the disc. In the rest of the cases, the angular momentum of each component does not suffer a significant evolution, although in the case in which the shell is counter-rotating with smaller angular momentum ($v_{rot} = 0.2, \theta_{tilt} = 150°$) the moduli of the angular momentum of the shell and the disc are perceptively reduced. For the cases with higher angular momentum ($v_{rot} = 0.7$), the impact of the interaction on the angular momentum of each flow is negligible. However, as we will see in the next section, even when the bulk of the gas remains unaffected in these cases, this situation does not prevent the inflow rates from being boosted by several orders of magnitude, thus effectively catalysing the inflow.

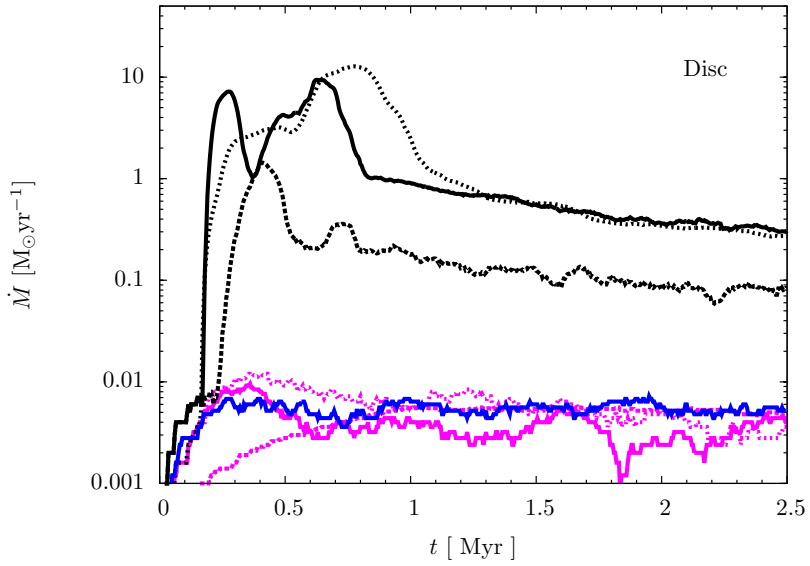

Figure 11: Inflow rate (in units of $M_\odot\ yr^{-1}$) versus time (Myr) for disc particles only. Magenta lines and black lines correspond to cases with $\theta_{tilt} = 60°$ and 150°, respectively. Long dashed lines correspond to $v_{rot} = 0.2$, continuous lines correspond to $v_{rot} = 0.3$ and short dashed lines correspond to $v_{rot} = 0.7$. A control case is also shown (blue line) where the disc is let evolve with no infalling, perturbing shell.

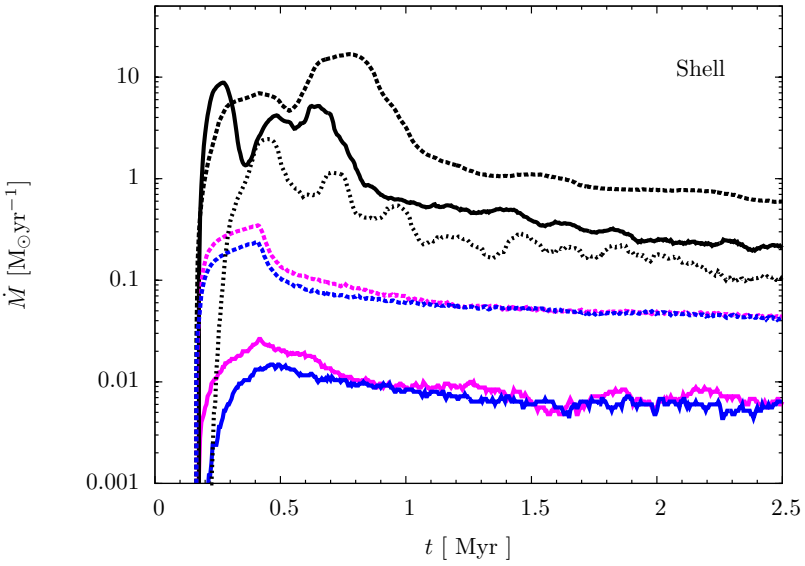

Figure 12: Inflow rate (in units of $M_\odot\ yr^{-1}$) versus time (Myr) for shell particles only. Magenta lines and black lines correspond to cases with $\theta_{tilt} = 60°$ and $150°$ respectively. Long dashed lines correspond to $v_{rot} = 0.2$, continuous lines correspond to $v_{rot} = 0.3$ and short dashed lines correspond to $v_{rot} = 0.7$. Control cases are also shown (blue lines) where the shells evolve with no primitive disc present ($\dot{M} < 10^{-5}$ for the $v_{rot} = 0.7$ case).

4.5 GAS INFLOWS

We have studied the hydrodynamics of a rotating gaseous shell falling towards a black hole surrounded by a previously formed $\sim$ 10 pc accretion disc. The particular problem we have been addressing here concerns how the presence of the disc, formed during a previous accretion event, affects the evolution of the shell, and whether the interaction is able to effectively boost or halt the inflow rate. Although the inflow rate which we compute for each system cannot be taken at face value due to the resolution employed, a comparative analysis does give us some insight into the problem.

Figure 10 compares the inflow rates corresponding to the six cases under study. It shows that counter-rotation between the interacting systems can effectively boost the inflow rate by more than two orders of magnitude at the peak of accretion, and sustain inflow rates $>$ 10 times higher than that obtained in the co-rotating cases at later times.

In order to be on more solid grounds, we have calculated the inflow rate associated to the disc and shell particles, separately, as a function of time (Figures 11 and 12 respectively). In each figure we have further introduced, for seek of clarity, control runs in which there is no infalling shell to perturb the primitive disc (Figure 11), or there is only an infalling shell with initial $v_{rot} = 0.2$, 0.3 and 0.7 not being perturbed by the primitive disc (Figure 12).

Accretion of disc particles is effectively boosted by $\sim 2-3$ orders of magnitude when the shell infalls in counter-rotation, while it is almost unaffected, or even slowed down, when the shell infalls in co-rotation (see figure 11). This is due to the fact that particles falling with high angular momentum kick lower angular momentum disc particles to higher orbits, preventing them from flowing in. Similarly, shell particles are accreted at a higher rate in the counter-rotating events.

Attention is drawn to the fact that even in the case in which the angular momentum distribution and modulus of each constituent of the system is mildly affected by the interaction, the inflow rate can be still highly enhanced. In the case $v_{rot} = 0.7$ and $\theta_{tilt} = 150°$, the angular momentum of each component of the system remained practically unaffected, as shown by Figures 8 and 9, thus we could think that this event would produce a negligible enhancement of the accretion rate, however, Figure 11 and Figure 12 tell otherwise. In this case, the primitive disc has boosted the accretion of the shell by up to 3 orders of magnitude, while the disc itself has lost mass to the black hole at a rate $\sim 10-100$ times greater than it would have done if the shell infall had not occurred. Thus, misaligned and uncorrelated nested accretion events are, in this way, capable of driving an important amount of gas inflow, acting as catalysts.

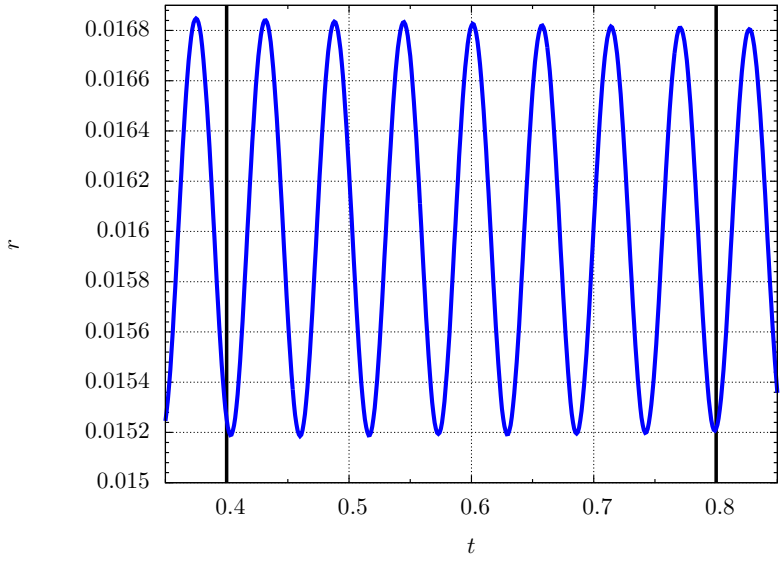

Figure 13: Mean radial distance of the gas particles (in code units) forming the primitive disc to the centre of the potential (i.e. to the black hole) as a function of time (in code units).

After the interaction has finished, the inflow rate damps and a stationary state of sustained residual accretion is established.

4.5.1 *Equilibrium State*

The analysis of the evolution of the primitive disc reveals that even when equilibrium is reached, the disc wobbles in the radial direction, this being a common behaviour throughout all the nested accretion events of this study.

Figure 13 shows the oscillation of the mean radius of the particles forming the disc in the absence of the infalling shell. The wobbling of the disc is due to the presence of residual ellipticity in the orbits of the gas particles with a periodicity which is consistent with near Keplerian motion. This dynamical state of the gas causes perturbations that lead to a constant inflow of particles through the inner boundary, giving rise to the sustained long term inflow observed in Figures 10, 11 and 12.

4.5.2 *Inner evolution*

Figure 14 shows the orientation of the angular momentum of the gas in the inner region close to the accretion radius, i.e. within $r_{acc} < r < r_{inner} = 0.005$, sampled at regular intervals of time ($\Delta t = 10^{-3}$).

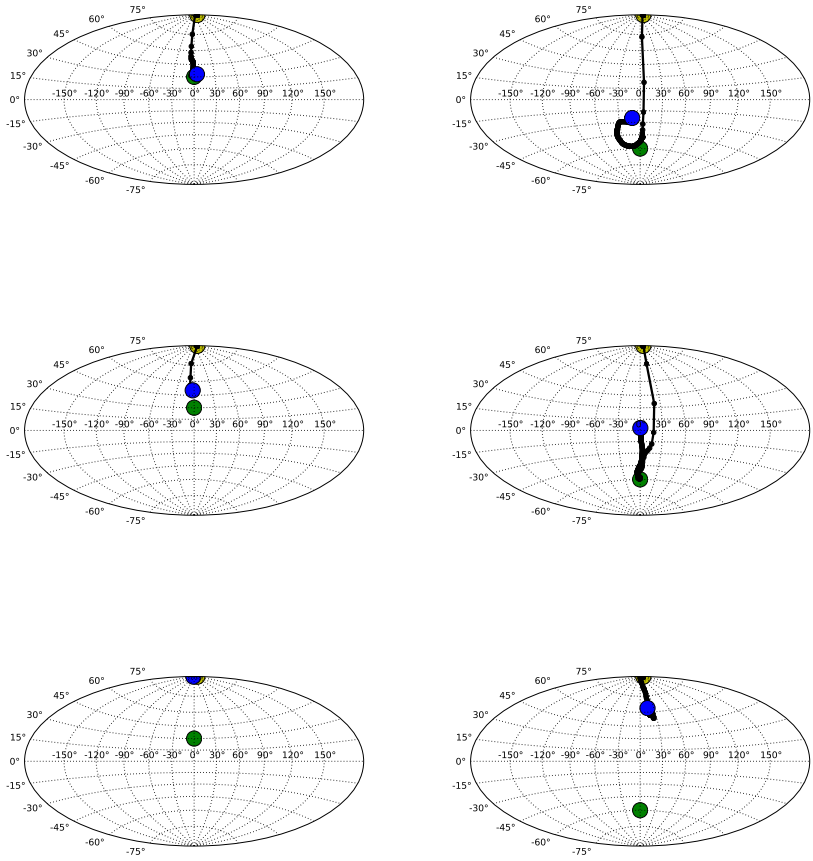

Figure 14: Angular momentum direction in the region between $r_{acc} < r < 0.005$ (corresponding to the inner 5 pc). The yellow dot marks the start of the interaction when the angular momentum points in the z direction, while the blue dot denotes the final state and the green dot the angular momentum direction of the shell, initially. From top to bottom, $v_{rot} = 0.2, 0.3, 0.7$. The left and right columns correspond to $\theta_{tilt} = 60°$ and $150°$ respectively.

The first column refers to co-rotating events, the second to counter-rotating events. Yellow dots refer to the initial orientation of the primitive disc; the blue dots refer to the final, equilibrium state, and green dots mark the orientation of the shell at the onset of the dynamical interaction. The angular momentum orientation which initially coincides with the orientation of the disc angular momentum soon shifts toward that of the shell, the final size of the shift being in proportion to the level of mixing that drove the inflow. For $J_{shell} > J_{disc}$, the weakness of the interaction leads to a final orientation which is closer to that of the disc, even in the case of counter-rotation. For $J_{shell} = J_{disc}$, when the shell falls in co-rotation, the direction of the innermost flow is at an angle $\theta_{acc} \sim 3\,\theta_{tilt}/4$ while in the counter-rotating case, it passes through θ_{tilt} but soon recedes to $\theta_{acc} \sim \theta_{tilt}/2$. For $J_{shell} < J_{disc}$, in the co-rotating case the direction of the inflow is at an angle $\theta_{acc} \sim \theta_{tilt}$ while in the counter-rotating case θ_{acc} at some moment reaches θ_{tilt} for later converging to a value $\theta_{acc} \sim 4\,\theta_{tilt}/5 \sim 120°$.

Figure 14 indicates that if a boost in the black hole feeding occurs through the collision of gas clumps on the scale probed in this simulations, the inner accretion flow would have to be changing orientation on the Myr time scale. The small scale flow does not preserve full memory of the larger scale orientation of the feeding events.

5

WARPED DISCS AS RELICS OF ANGULAR MOMENTUM CANCELLATION

In this chapter, numerical simulations are presented similar to those discussed in chapter 4. A wider distribution of angular momentum in the initial conditions is achieved by means of a turbulent kick to the initial velocity field in the shell. As the initial velocity field is more realistic, forming spread-out discs (as opposed to narrow rings), it allows us to better study the remnant morphologies of the gas after the disc-shell interaction has finished. Warped discs are clearly formed with $r_{disc} \simeq 10 - 20$ pc.

5.1 INITIAL CONDITIONS

The initial conditions for the simulations presented in this section are very similar to those presented in section 4.1, this time giving the shell an additional turbulent velocity field superimposed to the rotational one in the way described by Hobbs et al. (2011). The initial conditions for this set of simulations thus consist of a disc-like structure which spreads from the accretion radius $r_{acc} = 1$ pc out to $r \simeq 20$ pc, and a spherical shell with uniform density which extends from $r_{in} = 30$ pc to $r_{out} = 100$ pc. The shell is given a cylindrical velocity profile $v_\phi = v_{rot} = \text{const.}$, which takes the values $v_{rot} \simeq \{42, 63, 146\}\,\mathrm{km\,s^{-1}}$. In addition to the rotational velocity, the particles forming the shell are given a turbulent kick spectrum. The mean turbulent velocity is not a free parameter and is tied to the rotation velocity: $v_{turb} = v_{rot}$.

The disc is always generated from a shell like the one just described having initially $v_{rot} = v_{turb} = 63\,\mathrm{km\,s^{-1}}$. This single shell (i.e. without having a disc interior to it) evolves as it is not in equilibrium initially. Gas falls towards the centre and angular momentum mixing due to shocks combined with the turbulent velocity field, leads to the formation of an extended disc (as opposed to the narrow ring in section 4.1). After a time $t \simeq 1.5\,\mathrm{Myr}$ the disc reaches a stationary angular momentum distribution and the accretion rate is almost constant in time. At this time, we stop the simulation and surround the disc by a new uniform-density shell like the one from which the disc was born. The new shell, apart from having a different rotation and turbulent velocity, has its rotation axis tilted with respect to the axis of rotation of the primitive disc. The latter defines the z axis in all our simulations, so the primitive disc initially lies in the xy plane.

As in section 4.1, an isothermal equation of state has been assumed, $P = c_s^2 \rho$, with a constant temperature of $T = 10^3$K. The mass of the

shell is always the same as the mass of the disc, $M_{shell} = M_{disc}$ and the gas is considered to be non self-gravitating. Nevertheless we performed six additional simulations of single shells taking into account the self gravity of the gas to asses its effects and the validity of the non-self-gravity approximation. The units of mass, length and time remain the same as those defined in Section 4.1.

The turbulent velocity spectrum was given as a Gaussian random field with a Kolmogorov-like power spectrum (Kolmogorov, 1941),

$$P_v(k) \sim k^{-11/3}, \tag{45}$$

where k is the wave number, since this is still the simplest description that we have of a turbulent fluid (see however Federrath (2013) and references therein). The key assumption here is that the velocity field is homogeneous and incompressible, so we can define $\vec{v}$ in terms of a vector potential $\vec{A}$ such that $\vec{v} = \nabla \times \vec{A}$. As such, $\vec{A}$ is also described by a Gaussian random field with an associated power spectrum,

$$P_A(k) \sim k^{-17/3}. \tag{46}$$

To avoid a divergence in the variance of $|A|$ at small k, we introduce a small-scale cut-off k_{min}, so that

$$P_A(k) = C(k^2 + k_{min}^2)^{-17/6}, \tag{47}$$

where C is a normalization constant given to ensure that, given a box of volume $8\,r_{shell}^3$ containing the shell,

$$\frac{8\pi\, r_{shell}^3}{(2\,\pi)^3} \int_{k_{min}}^{k_{max}} P_A(k)\, k^2\, dk = \frac{3}{2} v_{turb}. \tag{48}$$

Physically the small-scale cut-off k_{min} can be interpreted as the scale $\lambda_{max} = 2\pi/k_{min} \sim r_{shell}$, the largest scale on which the turbulence is likely to be driven and $k_{max} = 10^4 k_{min}$ was introduced to cut the integral when convergence has been reached.

To generate the statistical realisation of the turbulent velocity field we first sample the vector potential $\vec{A}$ in Fourier space using a periodic cubic grid of dimension 256^3. We draw the amplitudes of the components of $\vec{A}_k$ at each point (k_x, k_y, k_z) from a Rayleigh distribution with a variance given by $|A_k|^2$ and assign phase angles that are uniformly distributed between 0 and 2π. We then Fourier-transform the vector potential to real space and take its curl to obtain the components of the velocity field. Finally, for estimating the turbulent velocity field at the position of each SPH particle, we use tricubic interpolation. The parameters of each simulation are given in Table 2.

Table 2: Parameters of the simulations: 4 simulations of single shells with the same specific angular momentum content (given by v_{rot}) and varying mass (M_{shell}) to asses the impact of self-gravity, 6 simulations of single shells of the same M_{shell} with varying v_{rot} and turbulent velocity (v_{turb}) to quantify the relevance of turbulence for dragging mass towards the central parsec, 12 more simulations of overlapping inflow events in near co- and counter-rotation ($\theta_{tilt} = 60°$ and 150° respectively) with and without turbulent velocity field to isolate the boost to the inflow rates produced by the overlapping of the inflows.

run	v_{rot}	v_{turb}	θ_{tilt}	M_{shell}/M_{BH}
v03-M2	0.3	0.3	–	0.01
v03-5M2	0.3	0.3	–	0.05
v03-M1	0.3	0.3	–	0.1
v03-M0	0.3	0.3	–	1.0
v02-nt	0.2	–	–	0.1
v03-nt	0.3	–	–	0.1
v07-nt	0.7	–	–	0.1
v02	0.2	0.2	–	0.1
v03	0.3	0.3	–	0.1
v07	0.7	0.7	–	0.1
v02t060-nt	0.2	–	60°	0.025
v02t150-nt	0.2	–	150°	0.025
v03t060-nt	0.3	–	60°	0.025
v03t150-nt	0.3	–	150°	0.025
v07t060-nt	0.7	–	60°	0.025
v07t150-nt	0.7	–	150°	0.025
v02t060	0.2	0.2	60°	0.025
v02t150	0.2	0.2	150°	0.025
v03t060	0.3	0.3	60°	0.025
v03t150	0.3	0.3	150°	0.025
v07t060	0.7	0.7	60°	0.025
v07t150	0.7	0.7	150°	0.025

5.2 SELF GRAVITY

By varying the mass of the gaseous inflowing shell we aim to sample the effects produced by self-gravity on the inflow. At very low masses as compared to that of the black hole, $m = M_{shell}/M_{BH} << 1$, we expect that the inflow proceeds cleanly as if the fluid were non self-gravitating. With increasing m, we expect the formation of clumps due to local gravitational instabilities. By doing this exercise we determine the mass threshold below which self-gravity is negligible and at the same time we assess the role of self-gravity in altering the values of the inflow rate onto the SMBH.

We performed 4 simulations of single turbulent inflows in which the total mass in the gaseous shell was varied, taking into consideration the self-gravity of the shell. The initial conditions were the same as those described in section 5.1, in these specific cases with an initial rotation velocity of $v_{rot} = v_{turb} = 0.3$ and a mass $M_{shell} = s \times M_{BH}$, for $s = 0.01, 0.05, 0.1, 1.0$.

5.2.1 *The development of clumps following the infall of a single shell*

Clumps developed in all the simulations of this section with the exception of the lowest mass run $m = 0.01$. In the left-panel of Figure 15 we show clump formation for the case $m = 0.1$ at the time of disc formation ($t = 0.3$)[1]. The clumps develop within a narrow ring at a circularization radius, $r_{circ} \simeq 16$ pc. The clumps grow gravitationally bound and revolve around the SMBH in quasi-Keplerian orbits. They barely interact among themselves, and when they do, they merge into bigger and denser clumps, but no scattering occurs that can bring mass towards the SMBH. Tidal tails develop among them but not strong enough to disrupt the dynamics of the disc outside their vicinities. In the right-panel of Figure 15 we show the smooth disc that forms when $m = 0.01$ corresponding to the case of negligible self-gravity.

5.2.2 *Inflow Rates*

We now compare the specific inflow rates, $\dot{M}/M_{shell}$, toward the central parsec, produced by varying the mass of the inflow. By doing this we can have a grasp of how relevant is self-gravity in either helping or preventing gas from falling from scales of $10 - 100$ pc down to the central parsec. The specific inflow rates for the four cases are compared in Figure 16. It appears that the specific accretion rates are independent of the mass of the inflow when the masses are low enough, $M_{shell} < 0.05 M_{BH}$. Even in the cases with $M_{shell} = 0.05 - 0.1\, M_{BH}$, in which self-gravity starts playing an important dynamical role by

1 The snapshots of our simulated discs were done using SPLASH (Price 2007)

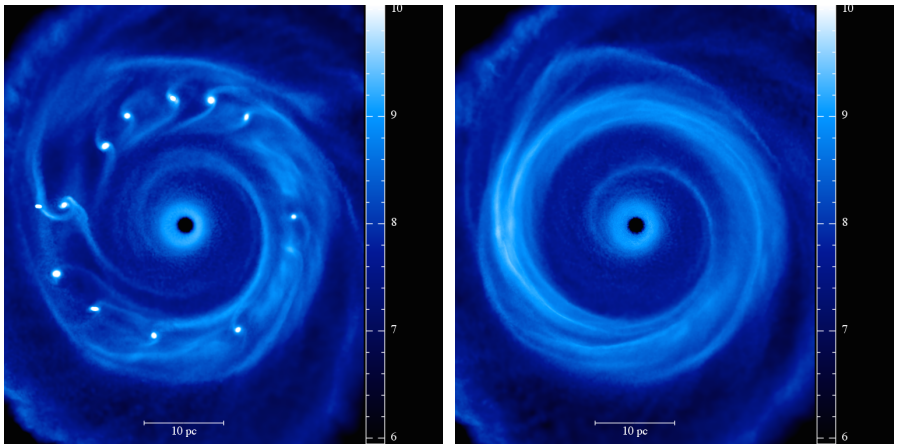

Figure 15: Projected $\log(\Sigma/M_{shell})$ in the xy plane when a disc form ($t = 0.3$ expressed in time units $T_u = 5$ Mry). The left-panel shows self-bound clumps in the $M_{shell} = 0.1\,M_{BH}$ model where self-gravity is important. The right-panel shows the disc in model $M_{shell} = 0.01\,M_{BH}$ where self-gravity is unimportant.

disrupting the inflow into clumps at r_{circ}, the accretion rate during the most active phase, $0.03 \lesssim t \lesssim 0.2$, remains unaffected by self-gravity. Thus we can safely model inflows of single shells as non-self-gravitating whenever $M_{shell} \lesssim 0.1 M_{BH}$ as far as the sub-pc inflow rate is concerned. This threshold must change when speaking about overlapping inflows, as we must have a space-filling gaseous disc for the second inflow with whom to interact. Thus, when treating overlapping inflows, we must have $M_{tot} = M_{disc} + M_{shell} \lesssim 0.05 M_{BH}$.

5.3 OVERLAPPING AND TURBULENCE

5.3.1 *Single shell*

Here we report on the impact turbulence has on the inflow rate towards the central parsec. We will compare the inflow rates when a turbulence velocity field characterized by $v_{turb} = v_{rot}$ is seeded to those obtained in absence of turbulence as reported in Paper I.

The key role of turbulence is that of broadening the structure of the disc by widening the initial angular momentum distribution, which causes more gas to circularise in lower as well as in higher orbits. Some of this gas crosses the accretion radius and some remains at the periphery forming a wide disc with which a second shell can interact to catalyse its inflow.

The inflow rates of turbulent and non-turbulent inflowing gaseous shells when no primitive disc is present are compared in Figure 17. The inflow rates are increased by at least two orders of magnitude by the turbulence and the total mass delivered to the central parsec is

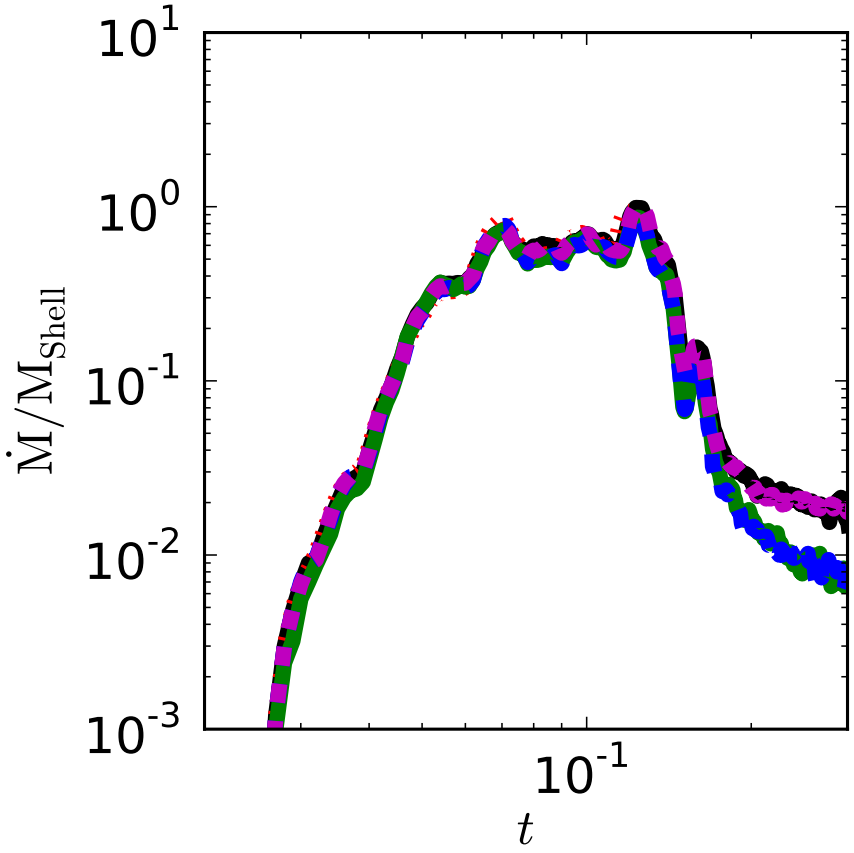

Figure 16: Particle accretion rates as a function of dimensionless time t t = 0.3 for the cases in which the mass of the inflowing shell is $M_{shell} = M_{BH}$ (red dotted), $0.1M_{BH}$ (blue-dashed), $M_{shell} = 0.05M_{BH}$ (green dashed) and $M_{shell} = 0.01M_{BH}$ (magenta-dashed). For comparison, the particle accretion rate of a case in which the non self-gravity approximation was used is also shown (black solid line)

increased from less than $10^{-3} M_{shell}$ to as much as $\sim 0.15 M_{shell}$. These two factors, i.e. widening the disc structure and putting more gas inside the accretion radius, make turbulence a key ingredient to drag gas inwards in our simulations, as also shown in Hobbs et al. (2011).

5.3.2 *Overlapping Inflows: morphology*

In this section we let a second turbulent shell to collapse and interact with a primitive disc widened by the initial turbulent spectrum of its parent shell and describe the morphological outcome of such scenario, as well as the impact of turbulence on the central inflow rate.

We find that the interaction of the shell with the primitive circumnuclear disc leads to the formation of a warped disc surrounded by a more extended and dynamically decoupled disc. In the absence of turbulence, the outcome of such interaction was a set of nested rings, as described in Paper I. The inclusion of turbulence to the velocity field, in this work, has proven to be a critical ingredient for triggering the formation of extended warped nuclear discs, as turbulence widens the angular momentum distribution of the infalling gas. By including turbulence, the cross section of interaction and overlap between the disc and the inflowing material widens, allowing smaller parcels of gas to interact with each other and change their mutual angular momentum in a less violent way.

5.3.2.1 *Counter-rotating flows*

As shown in Paper I, shells rotating in near opposite direction with that of a primitive disc have been particularly efficient in forming small scale dense nested rings and in transfering mass across the inner boundary. Here we examine the effects of turbulence in the case of counter-rotating shells: runs v02t150, v03t150 and v07t150, have shells with initial rotation velocities $v_{rot} = 0.2, 0.3$ and 0.7, and an initial tilt angle $\theta_{tilt} = 150^{\circ}$ relative to the z axis defined by the angular momentum of the primitive disc. Figure 18 shows the complex of nested discs that form after the hydrodynamical interaction.

In the run v02t150, the inflowing shell has a smaller specific angular momentum than that of the primitive disc ($J_{shell} = 2/3\, J_{disc}$). As the gas of the shell *rains* onto the disc, it mixes with the fluid particles of the disc. The encounter leads to an important cancellation of angular momentum, dragging a significant amount of mass within the accretion radius. The fluid particles that still preserve enough angular momentum remain close to the accretion radius, forming an extended *warped* disc comprising both shell and disc particles. This disc extends from $r_{acc} = 1$ pc up to 15 pc as shown in the top panels of Figure 18. Figure 18 shows the angle θ as a function of radius r to quantify the strength of the warp. The angle varies smoothly but not

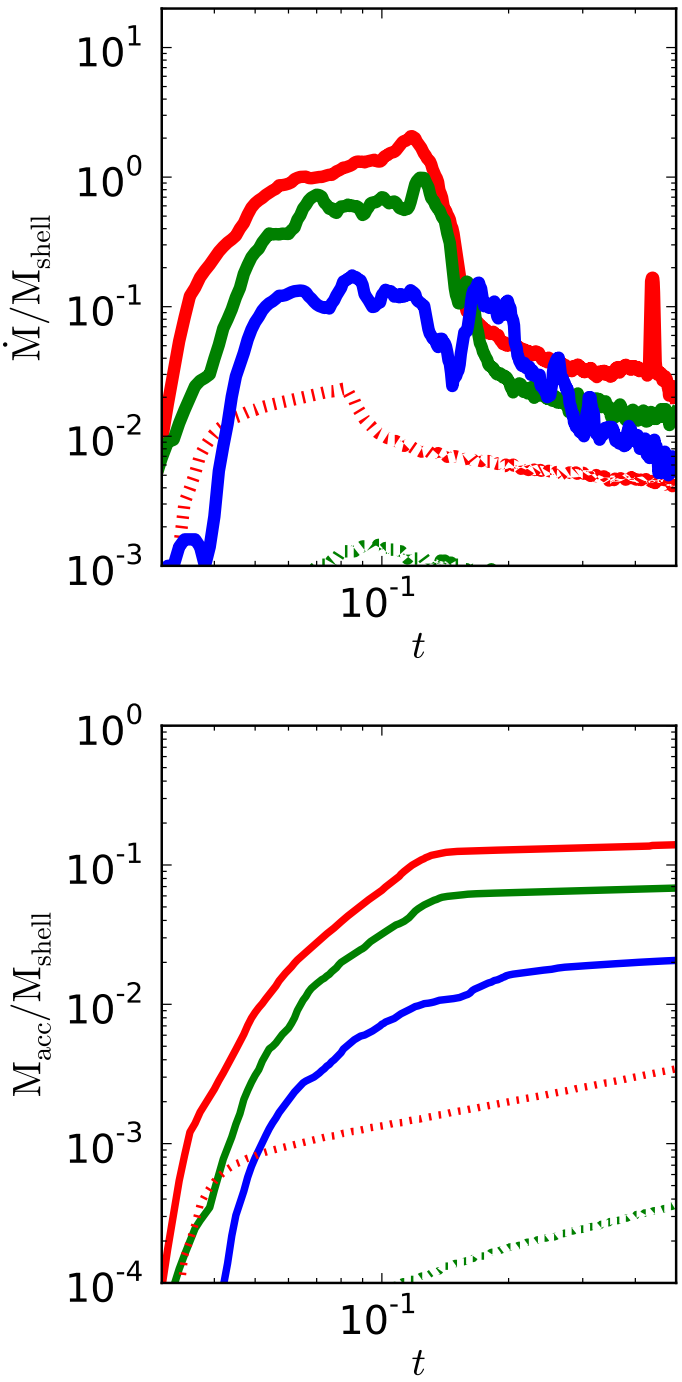

Figure 17: Inflow rate (top panel) and accreted mass (lower panel) across the inner boundary in units of M_{shell} for each run. In each panel colours correspond to different values of the angular momentum of the inflow measured by ν_{rot}. Red, green and blue colours correspond to $\nu_{rot} = (0.2, 0.3, 0.7)$ respectively, while different line styles correspond to the presence (solid) or absence (dotted) of the turbulent velocity field (where we set $\nu_{turb} = \nu_{rot}$ in each run). For the turbulent case with weaker rotational support the accreted mass is $\gtrsim 10\%$ of the total mass. It is evident that turbulence greatly enhances the sub-pc inflow.

monotonically inside the inner 5 pc, with a tilt varying from $\sim 100°$ down to 90° (i.e. with a rotation axis in the xy plane) and up again to $\sim 120°$, but no particles rotate at the initial tilt angle. At a distance of $\gtrsim 5$ pc there is a discontinuity (also in the surface density) and the disc changes the direction of rotation as its angle drops below 90°. At this point most of the gas particles forming the warp come from the primitive disc. Most of the disc mass is in the inner region of counter-rotation. As illustrated in Figure 18, the warped disc is surrounded by an outer disc made of shell particles which preserved their initial tilt angle of 150°, representing the fluid particles with the largest angular momentum. Here the disc is widened by the turbulence seeded initially in the velocity field and is not warped.

The most interesting warped disc structure forms in the run v03t150 (Figure 18, middle panels) corresponding to the case in which the disc and shell angular momenta are equal in modulus. One would naively expect to have all the gas of the shell mixed with all the gas of the disc, thus generating a single massive disc, shrunk and with its angular momentum making an angle $\theta \sim 1/2 \times 150°$ with the z axis. However, as the interaction starts taking place as soon as the first parcels of gas from the shell impact the primitive disc, the formation of the inner warped disc occurs earlier than the time needed for the rest of the shell to make its way down to the place where the primitive disc is. This late fraction of the shell will still interact with the rest of the disc, changing its orientation and shrinking its orbits without producing significant inflow. At this time, because of the shrinkage of the primitive disc, particles of the shell that were on the high tail of the angular momentum distribution will not be able to interact any more, thus remaining in orbit as an outermost less dense disc with the orientation the shell had initially ($\theta_{\rm tilt} = 150°$; see Figure 18, middle right panel). Figure 18 shows the angle θ describing the plane of rotation of the disc at the radial distance r, from which we observe the existence of three main regions: the innermost in co-rotation at $\theta \lesssim 90°$, the middle, also in co-rotation and with significant warping due to the strong perturbation induced by the infalling shell, and the outer region barely affected by the interaction.

The case of a shell with low mixing with the primitive disc is exemplified by the run v07t150, having a specific angular momentum $J_{\rm shell} > 2J_{\rm disc}$. This is illustrated in the bottom panels of Figure 18. The main effect is a gentle warping of the primitive disc perturbed by the interaction of fluid particles having in the shell specific angular momentum lower or comparable to that of the disc. The shell, at outer radii ($r \gtrsim 15$ pc), settles into a planar disc with no signs of warping.

5.3.2.2 *Co-rotating inflows*

When the inflow of a collapsing shell occurs in near co-rotation with the primitive disc, in contrast with the counter-rotating cases, there is no significant cancellation of angular momentum. The interaction leads to the formation of a single warped disc-like structure in which θ changes orientation smoothly with radius, i.e. a larger scale warped disc forms as illustrated in Figure 19. For the cases in which the inflow has lower and higher angular momentum than the primitive disc (i.e. runs v02to060 and v07to060) the warp looks particularly clean, whereas for the case in which the inflow and the primitive disc have the same angular momentum (run v03to060) the disc is more disturbed and the warp more structured.

Notice that θ is never changing monotonically with distance r. For the run v03to060, a large number of particles is concentrated just below and above the circularization radius ($r_{circ} = 16$ pc) whose rotation axes span a wide range of angles *at the same radius* (see bottom middle panel of Figure 19). These are particles whose rotation axis is either tilted by $\theta \simeq 10°$, almost parallel with the z axis of the primitive disc, or tilted by $\theta \sim 50°$, almost aligned with the mean angular momentum of the inflow. This suggests that the interaction has not yet finished, even if most of the accretion has already taken place. Gas at these radius will continue to shock-mix until a state of equilibrium is reached in which at each radius particles rotate around the same axis.

Runs v02to060 and v07to060 are smoother. At each radius particles rotate around a single axis (See Figure 19, left and right lower panels). From the inside to the outside the rotation axes in both cases span almost $\Delta\theta \simeq 60°$. The disc of v02to060 run starts in its inner region at $\simeq 30°$, tilting up to $\simeq 60°$ at $r \simeq 5$ pc and then decreasing its tilt angle down to $\simeq 10°$ at $r \lesssim 20$ pc. In v07to060 the inflow has larger specific angular momentum, and in this case the tilt angles show inverted trends: the inner region of the disc is tilted by $\simeq 10°$ while the outer region preserves the tilt of the mean angular momentum of the inflow, $\simeq 60°$ at $r \gtrsim 20$.

As a general trend, gas at the circularization radius of the primitive disc has its angular momentum aligned with the z axis while gas at the circularization radius of the shell has its angular momentum tilted with respect to the z axis by θ_{tilt}, keeping memory of its original orientation.

5.3.3 *Structure of the discs*

We have shown that counter-rotating inflows generate a warped disc surrounded by an outer less denser and less massive disc, while co-rotating inflows generate larger scale warps without causing a detachment of two separate discs. Figure 20 shows the surface den-

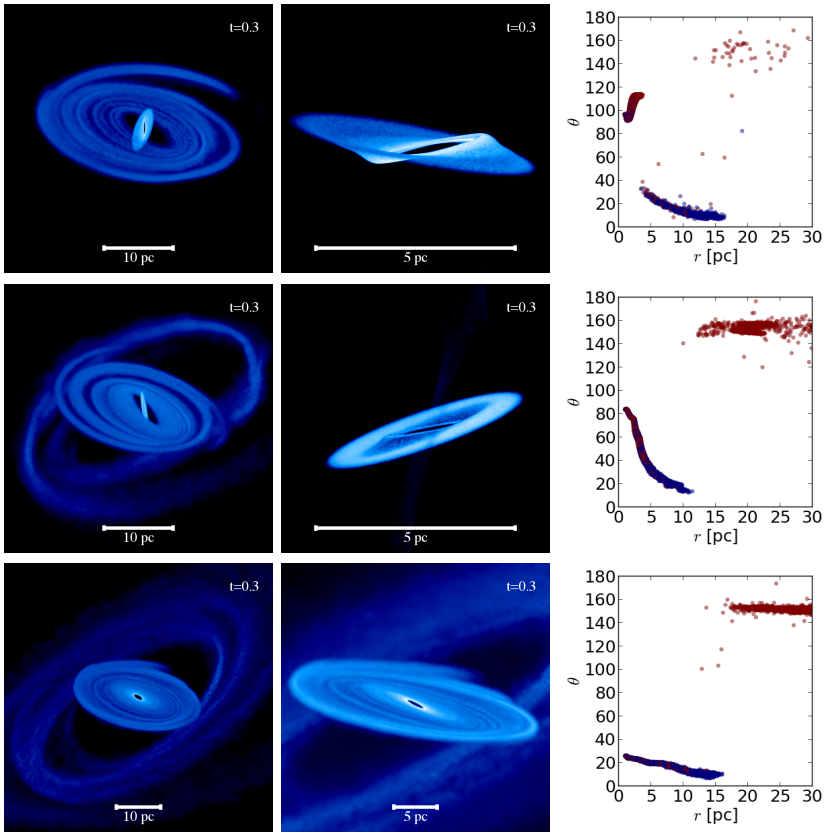

Figure 18: Warped discs formed when an inflow of gas, here modelled as a rotating gaseous turbulent shell, impacts a primitive circumnuclear disc in near counter-rotation ($\theta_{\rm tilt} = 150°$). The left column shows the generic outcome of these events. The central column shows a zoom into the innermost warped disc that forms (note that the disc view has been changed here to highlight better the degree of disc warping). The **right column** shows 10% of the particles selected randomly. For each particle we record its distance r (in units of pc) from the SMBH and its tilt angle θ between the specific angular momentum of he particle and the z axis (representing the rotation axis of the primitive disc). Red particles come from the shell while blue particles come from the primitive disc. We see that the inner and outer disc are always in counter-rotation. From top to bottom, each row corresponds to the cases v02t150, v03t150 and v07t150. The Figure illustrates the high degree of warping of the structure.

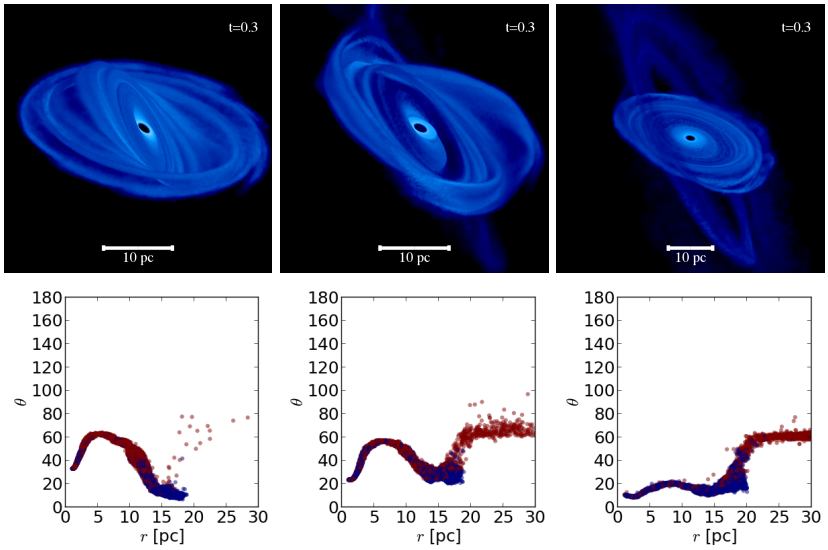

Figure 19: Warped discs formed when an inflow of gas, here modelled as a rotating gaseous turbulent shell, impacts a primitive circumnuclear disc in near co-rotation ($\theta_{\rm tilt} = 60°$). The **upper row** shows the generic outcome of these events: a large-scale warped disc which changes its plane of rotation from the inside to the outside. The **lower row** shows 10% of the particles selected randomly. For each particle we record its distance r (in units of pc) from the SMBH and its tilt angle θ between the specific angular momentum of the particle and the z axis (representing the rotation axis of the primitive disc). Red particles come from the shell while blue particles come from the primitive disc. Notice that these structures are always continuous discs that change their plane of rotation by as much as $\sim 60°$. From left to right, each column corresponds to the cases v02t060, v03t060 and v07t060. Notice that for the case v07t060 it would seem that the inner part of the disc is detached from the outer part, however the $r-\theta$ plot shows otherwise. In all cases there is a continuous mix of shell and primitive disc particles.

sity profiles, the mass profile $M(r)$ in units the total mass $M_{tot} = M_{disc} + M_{inflow}$ present when the structure has settled into equilibrium ($\lesssim 5 \times 10^6 M_\odot$) and the Toomre parameter approximated as

$$Q \simeq \frac{c_s \Omega}{\pi G \Sigma} \simeq \frac{\Omega^2}{2\pi G \langle \rho \rangle}, \tag{49}$$

where c_s, Σ and Ω are the speed of sound, the surface density and the angular frequency of the gas, respectively and $\langle \rho \rangle$ is the mean density related to $\Sigma = \langle \rho \rangle H$, with H the scale hight of the disc. To derive equation 49 we used the relation $(\Omega r)/c_s \simeq 1/2 \times H/r$ for thin discs, and, since the disc is quasi Keplerian, we approximated the epicyclic frequency $\kappa = \Omega$.

Counter-rotating inflows have higher surface densities than co-rotating inflows (at least in the v02t150 and v03t150) and are more bumpy. The mass enclosed in the warped disc increases more rapidly in counter-rotating inflows who also have a smaller and highly variable Toomre parameter within their structure than the co-rotating events. The parameter Q oscillates between $\lesssim$1 and 100 in the v02t150 and v03t150 whereas $Q \propto \Sigma^{-1} \gg 1$ in runs v02t60 and v03t60 since in this case the surface density of the disc is lower.

The evolution of the mass and angular momentum orientation inside the central 5 pc is shown in Figure 21 for the cases in which the shell fell in counter-rotation with the disc. The transient period, during which the angular momentum changes its orientation and the mass of the circum-nuclear disc grows, lasts $\Delta t_{trans} \lesssim 0.3$. During this time, a substantially more massive gas reservoir is left closer to the black hole, with its rotation plane having a completely different orientation from the one it had before the interaction. The mass in the central ~ 5 pc grows by more than one order of magnitude when $J_{shell} \lesssim J_{disc}$: about one half of the total gas mass was dragged down there in these two cases, increasing the initial mass of the gas reservoir by 12 and 20 times respectively. Even in the case in which $J_{shell} > J_{disc}$, the gas budget of the reservoir was doubled, containing $\simeq 10\%$ of the total gas mass. Had the gas mass contained in the inflow been bigger, the non-self gravity approximation would not hold any more. In that case gravitational instabilities would arise, leading to the fragmentation of the inflow.

5.3.4 *Sub-parsec inflow rates*

The inflow rates through the accretion radius $r_{acc} = 1$ pc, for all the overlapping inflows of this work, are shown in the left panel of Figure 22 as function of time (dashed and solid lines). In the same panel, we plot the inflow rate for the case of a single turbulent shell (with no primitive disc; dotted lines). The overlapping between the shell and the disc, in counter-rotation, leads to an increase of the inflow

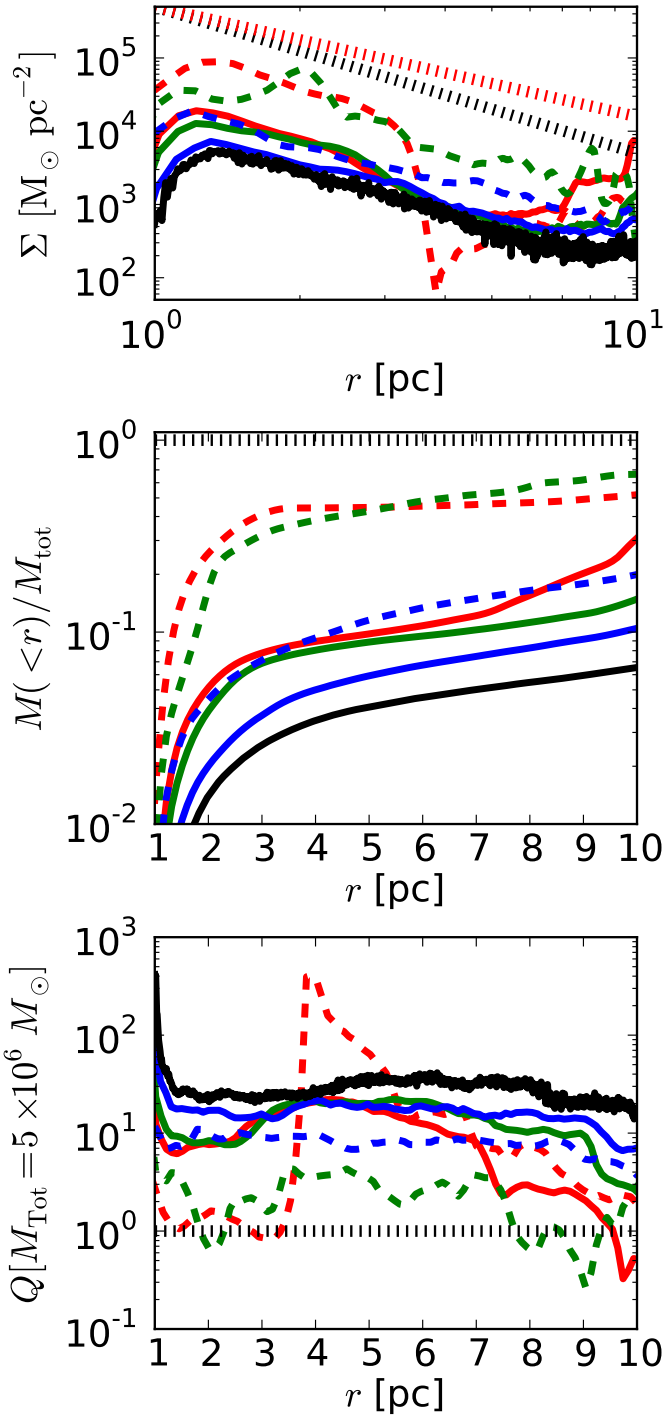

Figure 20: In each of the panels, colours correspond to different initial rotation velocities (different angular momentum of the collapsing shell): red, green, blue correspond to $\nu_{\rm rot} = 0.2, 0.3, 0.7$, respectively, while different line styles correspond to different shell orientation: solid for $\theta_{\rm tilt} = 60°$ and dashed for $\theta_{\rm tilt} = 150°$. All quantities are computed at $t = 0.3$, but black lines which correspond to $t = 0$. The top panel shows the surface density as function of radius. Two representative slopes are drawn as dotted lines: the black corresponding to $\Sigma \propto r^{-2}$ and the red corresponding to $\Sigma \propto r^{-1.5}$. The middle panel shows the cumulative gas mass distribution $M(r)$ in units of the total (disc + shell) mass. The bottom plane shows the Toomre Q parameter. Below $Q \sim 2$ the structure is unstable to fragmentation.

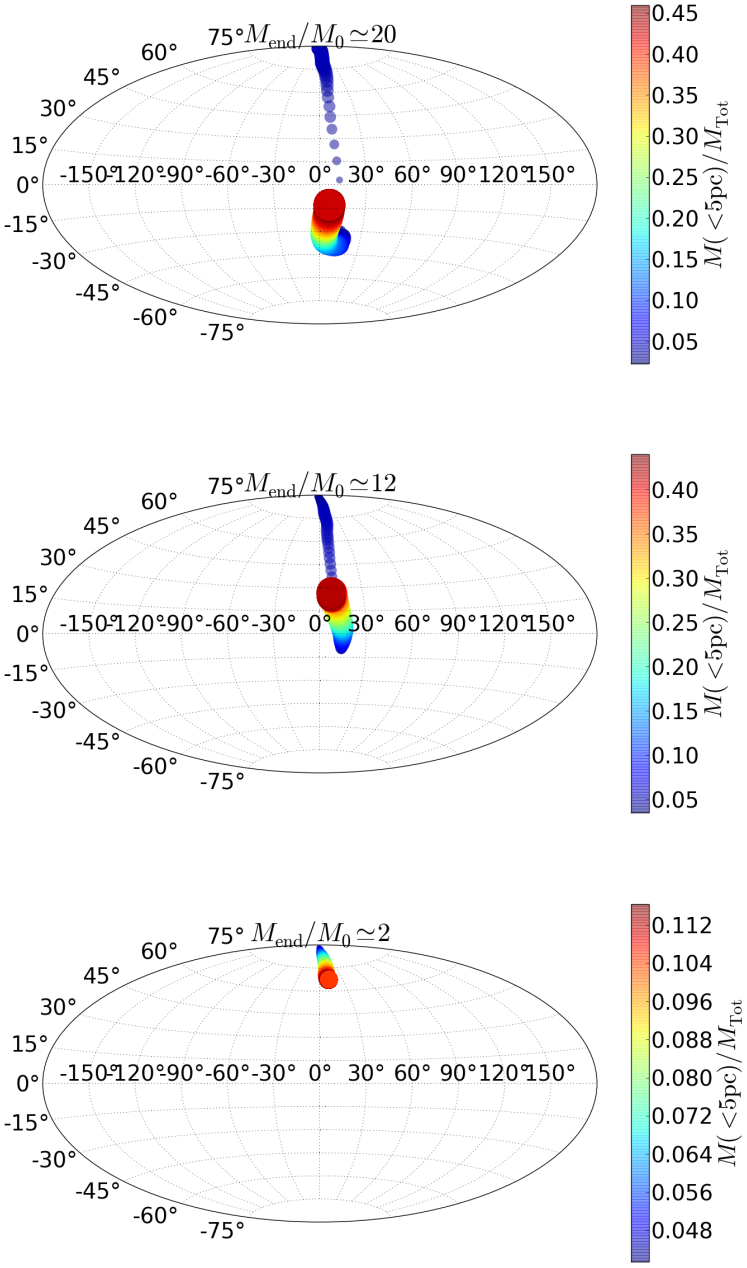

Figure 21: Angular momentum evolution of the gas contained in the inner 5 pc. Each point represents the orientation of the angular momentum at each time, with $\Delta t = 5 \times 10^3$yr. θ, the polar angle, in this figure runs from $\theta = -90°$ corresponding to the negative z direction to $\theta = 90°$ corresponding to the positive z direction. φ, the azimuthal angle, runs from $\varphi = 0°$ corresponding to the positive x axis to $\varphi = \pm 180°$ corresponding to the negative x axis. Colours show the mass contained in the inner 5 pc in units of the total gas mass, as shown by the colour bar. From top to bottom the three counter-rotating cases are shown: v02t150, v03t150, v07t150. Notice that in the first two cases the mass in the central region increases by 20 and 12 times respectively. Even in the last, higher angular momentum case, the mass inside 5 pc is doubled.

rates towards the central parsec as large as one order of magnitude irrespective of the angular momentum of the shell. The fraction of mass dragged toward the central parsec in these cases amounts to as much as 50 % the mass of the shell for the case in the lowest angular momentum case. Even in the highest angular momentum case, the total deliver of gas to the central parsec was no less than 1/10 as massive as the shell.

The right panel of Figure 22 shows the accreted mass as function of time for all the overlapping inflows of this work. In the most active events, v03t150 and v02t150, more than 40% of the mass of the shell falls into the accretion radius, while in the rest of the cases the total mass accreted amounts to less than 10 % of the total. Turbulence alone manages to drive 10 % of the shell gas into the central parsecs at a rate $\dot{M}/M_{shell} \lesssim 2.0$, but just in the lower angular momentum case (run v02). It is clear that counter-rotation between the shell and the primitive disc is more relevant than turbulence in driving gas inwards in our present study.

5.3.5 *Observational signatures*

A comparison between the rotation profiles of a single disc and the set of nested/warped discs that form after the interaction of two inflows can be made by looking at Figures 23 and 24. It is shown in each figure a random sample of 10 % of the particles of two selected simulations: a single disc generated from a turbulent gaseous shell (run v03) and the end state of a shell that fell onto a primitive disc with lower angular momentum and in near counter-rotation (run vrt02t150). Left and right panels in each figure correspond to the gas observed from two perpendicular line of sights (LOS) that coincide with the primitive disc being edge on and face on respectively. In the top panels the LOS velocity of each particle is plotted against its radial distance. In addition to it, a red line showing the eplerian velocity profile, $v_K \propto r^{-1/2}\cos(i)$, expected of a Keplerian disc, is superimposed, where the angle $i = 0$ for an edge on disc and $i = 90°$ for a face on disc. From those panels we immediately notice that the single primitive disc (Figure 23) has a rotation profile consistent with an almost flat Keplerian disc, whereas the case shown in Figure 24, in which the shell fell onto the disc, present a very different profile, not consistent with the rotation of a flat Keplerian disc. In the lower panels of each figure LOS velocity maps are shown with red and blue colours indicating receding and approaching gas. In the single disc case (Figure 23) a very ordered rotation is observed: gas approaching from the left and receding to the right when viewing the disc edge on, and gas with a very tiny almost constant velocity when the disc is face on. Instead, when observing the remnant of the overlap (Figure

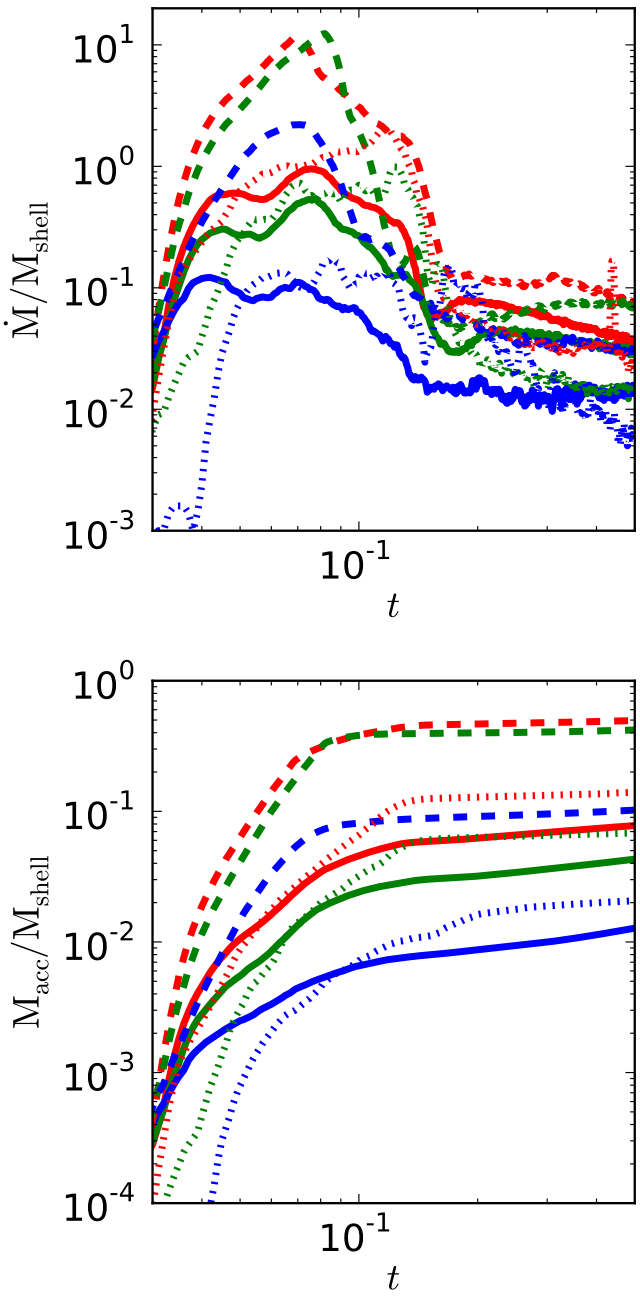

Figure 22: Inflow rate rate (upper panel) and accreted mass (lower panel), in units of M_{shell}, as a function of dimensionless time t (the time unit is $T_u = 5$ Myr). In each panel, colours correspond to different initial rotation velocities for the shell, and thus to different values of the angular momentum of the inflow: red, green, blue correspond to $v_{rot} = 0.2, 0.3, 0.7$, respectively, while different line styles correspond to shell orientation: solid for $\theta_{tilt} = 60°$, dashed for $\theta_{tilt} = 150°$. Dotted lines represent single turbulent inflows with no primitive disc (same colour code for v_{rot}). For the most active cases, 40 - 50 % of the original mass in the inflow has crossed the accretion radius, while for the less active events the accreted mass is $\sim 1\%$. Note that counter-rotating turbulent shells drive more inflow than turbulence alone does, and that turbulence alone drives more inflow than co-rotating turbulent inflows do.

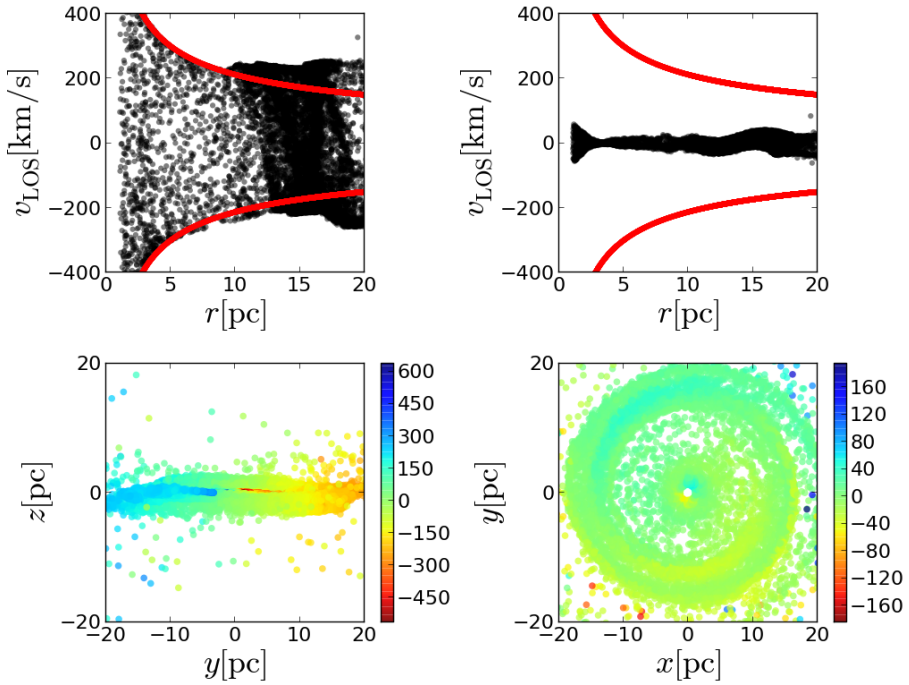

Figure 23: Nuclear primitive disc viewed edge on (left) and face on (right). In the top panels the line of sight (LOS) velocity of each particle is plotted in black against its distance from the black hole. Keplerian LOS velocity profiles are superimposed in red. Notice that in both cases the velocity profiles of the particles are consistent with Keplerian rotation: $v_{\rm LOS} \propto r^{-1/2}\cos(i)$, where $i = 0$ when the disc is edge on and $i = 90$ when it is face on. In the lower panels, we see the LOS velocity map. Bluer colours represent gas approaching the observer while redder colours represents gas receding from her/him. On the edge on case, the LOS velocity goes from being positive on the left side to negative on the right side (with an absolute maximum value of ~ 500 km s^{-1}), while on the face on case the LOS velocity is very small.

24), the ordered pattern just described is not present and it is clear that two kinematically decoupled bodies of gas are present.

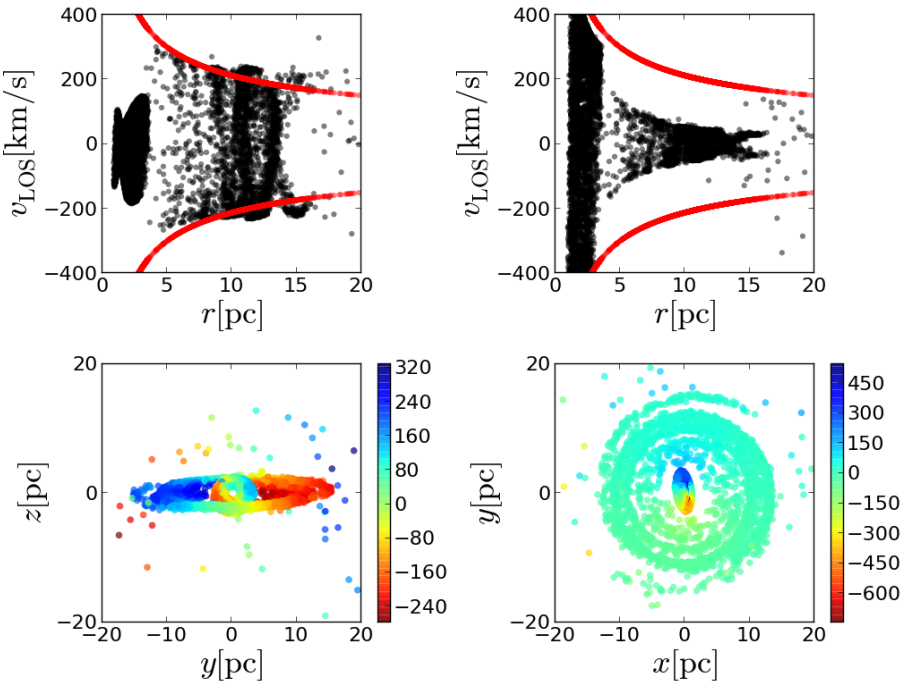

Figure 24: Nuclear discs that form after the interaction for the case vrto2tilt150 (the shell fell with lower angular momentum than the disc and in near counter-rotation). The line of sights are the same as those in Figure 23. In the top panels the line of sight (LOS) velocity of each particle is plotted in black against its distance from the black hole. Keplerian LOS velocity profiles are superimposed in red. Notice that in both cases the velocity profiles of the particles are not consistent with a flat disc in Keplerian rotation: $v_{\rm LOS} \propto r^{-1/2}\cos(i)$, where $i = 0$ when the disc is edge on and $i = 90°$ when it is face on. In the lower panels, we see the LOS velocity map. Bluer colours represent gas approaching the observer while redder colours represents gas receding from her/him. In both bottom panels it is clear that in the central region the is kinnematically detached from the rest.

Part III

CONCLUSIONS

6 SUMMARY AND CONCLUSIONS

We have described the hydro-dynamics of a rotating gas shell falling onto a primitive gaseous disc that rotates around a central black hole in a galactic bulge. The shell mimics a large scale instability in the nuclear region of a galaxy where a relic disc is present from an earlier inflow episode. The simulations are idealised and represent a toy model that helps us to understand how warped discs or nested misaligned rings can form in the interaction of different flows that coexist to possibly feed a central black hole.

6.1 SUMMARY

The infalling shell and the primitive disc perturb each other, causing a cancellation and re-distribution of their angular momentum content via shocks. Considerable mixing between the gas and shell particles occurs when the shell and disc have comparable angular momentum, forming a warped disc orthogonal to the primitive disc when some degree of counter-rotation is present. Co- and counter-rotating events from infalling shells with higher or lower angular momentum than the disc, produce nested ring like structures rotating on disjoint planes. A comparative analysis of the inflow rates onto the central black hole in the models explored shows that the infall of gas is boosted by more than two orders of magnitude relative to cases in absence of interaction. When the perturbation has ceased to act, inflows continue due to wobbling of the disc induced by gas particles in eccentric motion. This idealised representation shows that subsequent accretion episodes provide a viable way to drive major gas inflows toward the central parsec, and make relic discs more susceptible to accretion. Thus, nested inflow episodes possibly triggered by larger scale perturbations act as *catalysts* for the fuelling and growth of the central black hole.

Figure 25 summarises our results; here the specific mass accreted onto the SMBH (i.e. the mass that crossed the inner boundary at $r_{acc} \sim 1$ pc, normalised to the shell mass and computed at $t = 0.3$) is plotted as a function of the initial rotational velocity of the unstable shells ($v_{rot} = 0.2, 0.3$ and 0.7) representing the idealized inflow, for the entire data set in this Thesis.

Starting from the set of parameters that deliver the smallest fraction of gas towards the central parsec, in Figure 25, we have the case in which no turbulence and no primitive disc are present. Right above of it –although not noticeable in the Figure, we have co-rotating shells

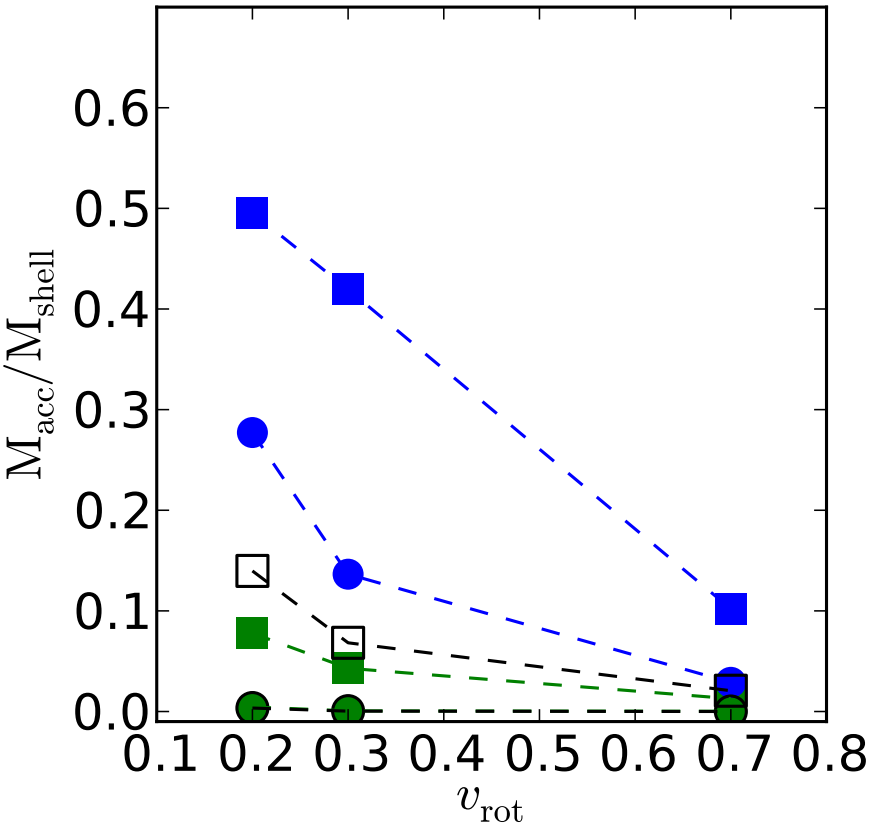

Figure 25: Fraction of mass (in units of M_{shell}) in the central parsec as function of initial rotational velocity for all the simulations in this work and those of Paper I. Colours blue and green refer to shells falling in co- and counter-rotation with the disc; circles and squares refer to the absence or presence of a turbulent kick in the initial conditions; empty symbols refer to shells falling in the absence of a nuclear disc. Thus, from bottom to top, data points joined by lines represent the following: i) single shells with no turbulence (**empty circles**; $< 10^{-2}$), ii) co-rotating overlapping inflows with no turbulence (**green circles**; $< 10^{-2}$), iii) co-rotating overlapping turbulent inflows (**green squares**), iv) turbulent single shells (**empty squares**), v) counter-rotating overlapping inflows with no turbulence (**blue cirlces**), vi) counter-rotating overlapping turbulent inflows (**blue squares**). It is evident that the presence of a nuclear disc severely enhances the mass flowing within the central parsec when the $\sim 10 - 100$ pc scale inflow falls in counter-rotation with it. See text for details.

with $\theta_{tilt} = 60°$ interacting with the primitive disc in absence of turbulence. These two cases (empty and green circles respectively) deliver just $\lesssim 10^{-2} M_{shell}$ worth of gas to the central parsec. The yield is increased to as much as 15% of the mass of the shell when a turbulent velocity field $v_{turb} = v_{rot}$ is seeded in a single shell with no primitive disc. Surprisingly, the interaction with a disc in this case lowers the accreted mass (green squares as compared with empty squares). This may be caused by the denser higher angular momentum gas from the primitive disc accelerating the more rarefied low angular momentum gas from the shell that falls early, impeding it to reach the accretion radius. Finally, the two most efficient sets of parameters to drive gas to the central parsec are those in which a primitive disc is present and the shell flows inward with an orientation $\theta_{tilt} = 150°$ relative to the disc (blue circles and squares), with the non turbulent case pouring almost 1/3 of the shell's worth of gas into the central parsec, and the turbulent case raising the yield up to $\sim 1/2 M_{shell}$ when the angular momentum is low ($v_{rot} = 0.2$). When the angular momentum is the highest in our dataset ($v_{rot} = 0.7$), the yields of counter-rotating overlapping inflows are of $0.1 M_{shell}$ for the turbulent case and $0.03 M_{shell}$ for the non-turbulent one: even if their high angular momentum would intrinsically make them deliver a negligible amount of mass into the central parsec, the interaction with a disc in near counter-rotation raises this number to levels comparable to those produced by lower angular momentum shells. These considerations hold true if the masses involved are low enough for the nuclear discs not to disrupt, as more massive clumpy discs would be expected to evolve into stellar discs and consequently would not exert the required hydrodynamical torques for triggering sub-pc inflows from the 100 pc gaseous shells that fall onto them. It is the presence of the nuclear disc acting as an obstacle that ultimately leads the gas towards the central parsec by cancelling out the angular momentum of the disc and shell gas.

6.2 CONCLUSIONS

Accretion in the very vicinity of massive black holes may occur chaotically, i.e. through a sequence of accretion events that give rise to smaller-scale viscous discs, each with a different and random orientation of their angular momentum relative to the spin of the central massive black hole (e.g. King & Pringle 2006, 2007). Our simulations explored the formation of nuclear warped discs due to hydrodynamical interactions only. The misaligned, nested rings resulting from the disc-shell interaction have no connection with the black hole spin, nor with the warping or breaking of the disc due to Lense-Thirring precession (Lodato & Price 2010; Nixon et al. 2012a), and should not be confused. Instead, this study is in line and extends that of Nixon

et al. (2012b), who simulated the evolution of two misaligned (non-self gravitating) discs in the gravitational (Keplerian) potential of a massive black hole. They showed that the accretion rate is enhanced in a similar way by cancellation of angular momentum at the junction of the two pre-placed discs. What we have shown is that strong misalignment between a ~ 100 pc inflow and an already present ~ 20 pc disc is an effective way of increasing the delivery of gas towards the central parsec, even when gas is flowing inwards with a relatively high angular momentum (e.g. triggered by a minor merger) and would not feed the SMBH by itself. The interaction of inflowing gas with relic structures must therefore be taken into account when studying the path of the gas from galactic scales down to the vicinity of the black hole. Inflows across the inner pc do not necessarily preserve the orientation of the parent flows –especially when the parent flows have some degree of counter-rotation, and this could have important implications on the evolution of the spin of SMBHs.

After the interaction between the inflowing shell and the circumnuclear disc has terminated and the peak of accretion has passed, the morphology of the remaining gas is a warped disc, pointing to a natural connection between the angular momentum cancellation mechanism and the source of misalignment. If nuclear discs with line-of-sight velocity signatures as described in section 5.3.5 were to be observed, and if such signatures were to appear in galaxies showing nuclear activity, they could give us some insight into the validity and importance of the feeding mechanism proposed in this Thesis.

At present we can only speculate, as it is still an open question the fate of the gas that makes its way down to the central $\lesssim 10$ pc of a galaxy, where the black hole starts dominating the potential. However, the results discussed in this Thesis suggest that overlapping inflows could in principle alleviate the problems of i) feeding the SMBH and the formation of a gas reservoir (Lapi et al. 2014); ii) the formation of warps and counter-rotating circumnuclear discs (Bartko et al. 2009; Genzel et al. 2010); and iii) episodic star formation, giving rise to populations of stars of different ages with different rotational axis.

6.3 FUTURE WORK

We have seen that, when the gas mass of the shell becomes comparable to that of the black hole, self gravity's role is that of disrupting the disc into clumps. However, the fate of the gas within those clumps is still uncertain (e.g. Lodato 2007; Begelman & Shlosman 2009). One scenario is that gas, due to the thermal plus turbulent pressure, would settle into a clumpy nuclear disc. Another possible scenario is that stars would be formed within the disc. In each of these cases it still needs to be explored what the outcome of the shell-disc (clumpy or stellar) interaction would be. An additional hypothesis worth explor-

ing is that in which the shell-disc interaction not only cancels out the angular momentum of the gas, but also induces star formation. In fact, observations suggest that young starbursts of ages < 50 Myr are associated with low Eddington ratio AGN, while high accretion rates are only observed in galaxies with older starbursts of 50 - 100 Myr. Modelling the gas behaviour at sub-parsec scales within the overlapping inflows scenario could allow us to discard or retain the model as a good mechanism of AGN fuelling. If viscous-like stresses drove the gas from that scale inwards, gas would still take a Hubble time to make its way to the BH (e.g. Frank et al. 2002; King 2008), we thus need the disc-shell interaction to drive gas further inwards to feed the black hole in the required time, namely, 50-100 Myr after the starburst episode. In this line of reasoning, we need to keep in mind that, even if the idealized scenario studied in this Thesis has served as a proof of concept for our overlapping inflow hypothesis, more realistic initial velocity profiles and configurations need to be tested before the hypothesis can be confronted with observations. Initial conditions taken from larger scale simulations of galaxy mergers or bar-unstable galaxies, *alla-Hopkins & Quataert (2010a)*, are thus desired.

We have also argued that the outcome of BH feeding due to overlapping inflows would leave as relic structures warped discs. This could alleviate the problem of AGN warped discs, for which no source of torque is evident to warp them (See e.g. Tremaine & Davis 2014), even if there is strong circumstantial evidence indicating that AGN discs are indeed warped. Masser discs having modest warps are present in NGC 4258 (Herrnstein et al. 2005) and Circinius (Greenhill et al. 2003) to cite a couple of cases. It has also been proposed that such warping of the discs could play an important role on the AGN unification paradigm based on orientation (Nayakshin 2005), and, when combined with star formation, the interaction between gas clouds could lead to the formation of warped stellar discs as those observed in the Galactic Centre (Nayakshin & Cuadra 2005; Hobbs & Nayakshin 2009; Genzel et al. 2010; Alig et al. 2013; Lucas et al. 2013). Observation and catalogue of warps could then tell us about the inflow and activity of nearby SMBH.

A scenario worth being explored in the near future is that in which the AGN-starburst connection (Davies et al. 2007) arises as a natural consequence of the angular momentum cancellation mechanism –The disc-shell interaction. We would draw the scenario as follows: Some of the gas from the first gaseous shell that forms the primitive disc flows towards the black hole; no star formation takes place. After some time, the secondary inflow, on interacting with the disc triggers a starburst and a huge inflow towards the BH. At this time, gas from the first shell is finally arriving to the BH, feeding a low luminosity AGN. Meanwhile, the second inflow triggered by the shell-disc interaction is on its way towards the black hole. AGN activity will re-

main low until the second inflow reaches the BH. Thus, the starburst formed by the disc-shell interaction is accompanied by a low luminosity AGN while it is young. By the time the inflow triggered by the disc-shell interaction reaches the BH, a high luminosity AGN is seen accompanied by an older starburst. This is a model that would need to be tested with more realistic physics included: star formation, heating, cooling, AGN feedback and more realistic initial conditions.

Part IV

APPENDIX

A

KOLMOGOROV TURBULENCE POWER SPECTRUM

Let us calculate now how the energy is distributed across the different scales in a turbulent velocity field. We first assume that a flow exist in some region of space which is turbulent, statistically homogeneous, and has no mean velocity component. Using Fourier techniques, one can decompose this velocity field in wave normal (i.e. independent of each other) modes. By doing this, the turbulent kinetic energy contained in eddies of a length scale l (within the inertial range) is expressed as the energy contained in waves with wave number $k \sim 2\pi/l$.

We start our analysis by taking the Fourier transform of the velocity field, $\mathcal{F}\{\vec{v}(\vec{x})\}$:

$$\hat{\vec{v}}(\vec{k}) = \frac{1}{(2\pi)^{3/2}} \int_{\infty} \vec{v}(\vec{x}) e^{-i\vec{k}\cdot\vec{x}} d^3\vec{x}, \tag{50a}$$

$$\vec{v}(\vec{x}) = \frac{1}{(2\pi)^{3/2}} \int_{\infty} \hat{\vec{v}}(\vec{k}) e^{i\vec{k}\cdot\vec{x}} d^3\vec{k}. \tag{50b}$$

Notice that, dimensionally, $[\hat{\vec{v}}(\vec{k})] = [\vec{v}(\vec{x})] \times l^3$. We know from Parseval's Theorem[1] that $\|\vec{v}(\vec{x})\| = \|\hat{\vec{v}}(\vec{k})\|$. With this motivation in mind let us take the following product:

$$\hat{\vec{v}}(\vec{k})^* \cdot \hat{\vec{v}}(\vec{k}') = \frac{1}{(2\pi)^3} \int_{\infty}\int_{\infty} \vec{v}(\vec{x'})\, \vec{v}(\vec{x})\, e^{i(\vec{k}\cdot\vec{x} - \vec{k'}\cdot\vec{x'})}\, d^3\vec{x}\, d^3\vec{x}', \tag{51}$$

where $\vec{v}^*$ stands for the complex conjugate of $\vec{v}$. We now change variables, $\vec{r} = \vec{x}' - \vec{x}$, and ensemble-average the equation to arrive to a quadratic form of the velocity spectrum in wave-space. Since the only random term on the right hand side are the velocities, we have:

$$\begin{aligned} &\left\langle \hat{\vec{v}}(\vec{k})^* \cdot \hat{\vec{v}}(\vec{k}') \right\rangle = \\ &\frac{1}{(2\pi)^3} \int_{\infty}\int_{\infty} \langle \vec{v}(\vec{x}+\vec{r})\, \vec{v}(\vec{x}) \rangle\, e^{i(\vec{k}-\vec{k}')\cdot\vec{x}}\, e^{-i\vec{k'}\cdot\vec{r}}\, d^3\vec{x}\, d^3\vec{r}. \end{aligned} \tag{52}$$

Because of homogeneity, the average on the right is independent of x, so we can rearrange the integrals in a more convenient way:

$$\begin{aligned} &\left\langle \hat{\vec{v}}(\vec{k})^* \cdot \hat{\vec{v}}(\vec{k}') \right\rangle = \\ &\frac{1}{(2\pi)^3} \int_{\infty} \langle \vec{v}(\vec{x}+\vec{r}) \cdot \vec{v}(\vec{x}) \rangle\, e^{-i\vec{k'}\cdot\vec{r}} \left[\int_{\infty} e^{i(\vec{k}-\vec{k}')\cdot\vec{x}} d^3\vec{x} \right] d^3\vec{r}. \end{aligned} \tag{53}$$

1 Although the term "Parseval's theorem" is often used to describe the unitarity of any Fourier transform, especially in physics and engineering, the most general form of this property is more properly called the Plancherel theorem.

The integral in square brackets is equivalent to the Dirac delta distribution, so we can rewrite in a more compact and transparent form:

$$\left\langle \hat{\vec{v}}(\vec{k})^* \cdot \hat{\vec{v}}(\vec{k}') \right\rangle = \frac{\delta(\vec{k}-\vec{k}')}{(2\pi)^3} \int_\infty \langle \vec{v}(\vec{x}+\vec{r})\, \vec{v}(\vec{x}) \rangle \; e^{-i\vec{k}'\cdot\vec{r}} \, d^3\vec{r}. \tag{54}$$

We have thus found that, in contrast to what happens in real space, the Fourier amplitudes of the velocity field are uncorrelated unless $\vec{k} = \vec{k}'$ (As expected by decomposing the turbulent field in normal modes). Integrating over $\vec{k}'$ yields, in the right hand side, the Fourier transform of the correlation function $\hat{A}(\vec{k}) = \mathcal{F}\{A(\vec{r})\}$, while the left hand-side defines the *power spectrum* of the velocity field, $P[v]$:

$$\begin{aligned} P[v] &\equiv \int_\infty \left\langle \hat{\vec{v}}(\vec{k})^* \cdot \hat{\vec{v}}(\vec{k}') \right\rangle d^3\vec{k}' = \\ \hat{A}(\vec{k}) &= \frac{1}{(2\pi)^{3/2}} \int_\infty A(\vec{r}) e^{-i\vec{k}\cdot\vec{r}} \, d^3\vec{r}. \end{aligned} \tag{55}$$

By recovering $A(\vec{r})$ using the inverse Fourier transform,

$$A(\vec{r}) \equiv \langle \vec{v}(\vec{x}) \cdot \vec{v}(\vec{x}+\vec{r}) \rangle = \frac{1}{(2\pi)^{3/2}} \int_\infty \hat{A}(\vec{k}) e^{i\vec{k}\cdot\vec{r}} \, d^3\vec{k}, \tag{56}$$

we notice that, at zero lag ($r = 0$), we can compute the mean kinetic energy per unit mass in the turbulent field as:

$$\frac{1}{2} \langle v^2 \rangle = \frac{1}{2} A(0) = \frac{1/2}{(2\pi)^{3/2}} \int_\infty \hat{A}(\vec{k}) \, d^3\vec{k}, \tag{57}$$

where the integral can be simplified for an homogeneous and isotropic turbulent velocity field:

$$\frac{1}{2} \langle v^2 \rangle = \int_0^\infty E(k) \, dk = \frac{1}{(2\pi)^{3/2}} \int_0^\infty 2\pi \hat{A}(k) \; k^2 dk. \tag{58}$$

In this way we define the *energy spectrum* $E(k)$ of an homogeneous and isotropic turbulent velocity field to be:

$$E(k) = k^2 \hat{A}(k)/\sqrt{2\pi}. \tag{59}$$

This expression gives us the energy per wave number k, that is, the energy contained in eddies of size $l \sim 2\pi/k$. We have seen throughout this Appendix that a close relation exists between the energy spectrum and the statistics of the turbulent velocity field. Because of the symmetric way in which we defined the Fourier transform, the normalization constant is different to the one that is customary. Had

we defined the Fourier transform in a different way, with a factor of $1/(2\pi)^3$ in front of the integral that switches from real to spectral space, the normalization would be the customary one:

$$E(k) = 2\pi k^2 \hat{A}(k). \tag{60}$$

We attach to this normalization within the main body of this Thesis.

BIBLIOGRAPHY

Abel, T., Bryan, G. L., & Norman, M. L. 2002, Science, 295, 93

Alexander, D. M., & Hickox, R. C. 2012, New Astro. Rev., 56, 93

Alexander, D. M., Bauer, F. E., Brandt, W. N., et al. 2011, ApJ, 738, 44

Alig, C., Schartmann, M., Burkert, A., & Dolag, K. 2013, ApJ, 771, 119

Aller, M. C., & Richstone, D. O. 2007, ApJ, 665, 120

Aluie, H. 2011, Physical Review Letters, 106, 174502

—. 2013, Physica D Nonlinear Phenomena, 247, 54

Antonucci, R. 1993, ARA&A, 31, 473

Balbus, S. A., & Hawley, J. F. 1998, Reviews of Modern Physics, 70, 1

Balsara, D. S. 1995, Journal of Computational Physics, 121, 357

Balsara, D. S., Kim, J., Mac Low, M.-M., & Mathews, G. J. 2004, ApJ, 617, 339

Banerjee, R., Klessen, R. S., & Fendt, C. 2007, ApJ, 668, 1028

Barai, P., Viel, M., Murante, G., Gaspari, M., & Borgani, S. 2014, MNRAS, 437, 1456

Barnes, J. E., & Hernquist, L. 1992, ARA&A, 30, 705

—. 1996, ApJ, 471, 115

Bartko, H., Martins, F., Fritz, T. K., et al. 2009, ApJ, 697, 1741

Bate, M. R., & Bonnell, I. A. 2005, MNRAS, 356, 1201

Bate, M. R., Bonnell, I. A., & Price, N. M. 1995, MNRAS, 277, 362

Bauer, A., & Springel, V. 2012, MNRAS, 423, 2558

Begelman, M. C., Blandford, R. D., & Rees, M. J. 1984, Reviews of Modern Physics, 56, 255

Begelman, M. C., & Shlosman, I. 2009, ApJL, 702, L5

Beifiori, A., Courteau, S., Corsini, E. M., & Zhu, Y. 2012, MNRAS, 419, 2497

Bender, R., Kormendy, J., Bower, G., et al. 2005, ApJ, 631, 280

Berti, E., & Volonteri, M. 2008, ApJ, 684, 822

Best, P. N., Kauffmann, G., Heckman, T. M., et al. 2005, MNRAS, 362, 25

Bîrzan, L., McNamara, B. R., Nulsen, P. E. J., Carilli, C. L., & Wise, M. W. 2008, ApJ, 686, 859

Blandford, R. D., & Znajek, R. L. 1977, MNRAS, 179, 433

Bonazzola, S., Perault, M., Puget, J. L., et al. 1992, Journal of Fluid Mechanics, 245, 1

Bondi, H. 1952, MNRAS, 112, 195

Booth, C. M., & Schaye, J. 2009, MNRAS, 398, 53

—. 2010, MNRAS, 405, L1

Boroson, T. 2005, AJ, 130, 381

Bournaud, F., & Combes, F. 2002, A&A, 392, 83

Breitschwerdt, D., de Avillez, M. A., Fuchs, B., & Dettbarn, C. 2009, Space Sci. Rev., 143, 263

Burgers, J. M. 1948, Adv. Appl. Mech, 1, 171

Burkert, A., & Tremaine, S. 2010, ApJ, 720, 516

Cao, X. 2007, ApJ, 659, 950

Cappi, M. 2006, Astronomische Nachrichten, 327, 1012

Caramana, E., Shashkov, M., & Whalen, P. 1998, Journal of Computational Physics, 144, 70

Carmona-Loaiza, J. M., Colpi, M., Dotti, M., & Valdarnini, R. 2014, MNRAS, 438, 1698

—. 2015, "Submitted to MNRAS"

Carroll, J. J., Frank, A., & Blackman, E. G. 2010, ApJ, 722, 145

Cavagnolo, K. W., McNamara, B. R., Nulsen, P. E. J., et al. 2010, ApJ, 720, 1066

Chandrasekhar, S. 1949, ApJ, 110, 329

—. 1951a, Royal Society of London Proceedings Series A, 210, 18

—. 1951b, Royal Society of London Proceedings Series A, 210, 26

Chang, P., Murray-Clay, R., Chiang, E., & Quataert, E. 2007, ApJ, 668, 236

Choi, J.-H., Shlosman, I., & Begelman, M. C. 2013, ArXiv e-prints

Chokshi, A., & Turner, E. L. 1992, MNRAS, 259, 421

Choudhuri, A. R. 1998, The physics of fluids and plasmas : an introduction for astrophysicists /

Clarke, C., & Carswell, B. 2007, Principles of Astrophysical Fluid Dynamics

Colpi, M., & Dotti, M. 2009, ArXiv e-prints

Corsini, E. M. 2014, in Astronomical Society of the Pacific Conference Series, Vol. 486, Astronomical Society of the Pacific Conference Series, ed. E. Iodice & E. M. Corsini, 51

Croston, J. H., Kraft, R. P., Hardcastle, M. J., et al. 2009, MNRAS, 395, 1999

Cuadra, J., Nayakshin, S., & Martins, F. 2008, MNRAS, 383, 458

Cuadra, J., Nayakshin, S., Springel, V., & Di Matteo, T. 2006, MNRAS, 366, 358

Cunningham, N. J., Moeckel, N., & Bally, J. 2009, ApJ, 692, 943

Darg, D. W., Kaviraj, S., Lintott, C. J., et al. 2010, MNRAS, 401, 1552

Davies, R. I., Maciejewski, W., Hicks, E. K. S., et al. 2009, ApJ, 702, 114

Davies, R. I., Müller Sánchez, F., Genzel, R., et al. 2007, ApJ, 671, 1388

Di Matteo, T., Colberg, J., Springel, V., Hernquist, L., & Sijacki, D. 2008, ApJ, 676, 33

Di Matteo, T., Springel, V., & Hernquist, L. 2005, in Growing Black Holes: Accretion in a Cosmological Context, ed. A. Merloni, S. Nayakshin, & R. A. Sunyaev, 340–345

Diehl, S., Rockefeller, G., Fryer, C. L., Riethmiller, D., & Statler, T. S. 2012, ArXiv e-prints

Dobbs, C. L., & Bonnell, I. A. 2008, MNRAS, 385, 1893

Dolag, K., Vazza, F., Brunetti, G., & Tormen, G. 2005, MNRAS, 364, 753

Dressler, A. 1989, in IAU Symposium, Vol. 134, Active Galactic Nuclei, ed. D. E. Osterbrock & J. S. Miller, 217

Dressler, A., & Richstone, D. O. 1988, ApJ, 324, 701

Dumas, G., Mundell, C. G., Emsellem, E., & Nagar, N. M. 2007, MNRAS, 379, 1249

Dunn, R. J. H., Fabian, A. C., & Taylor, G. B. 2005, MNRAS, 364, 1343

Elitzur, M. 2008, New Astro. Rev., 52, 274

Elmegreen, B. G. 2008, ApJ, 672, 1006

Elmegreen, B. G., & Burkert, A. 2010, ApJ, 712, 294

Elmegreen, B. G., & Scalo, J. 2004, ARA&A, 42, 211

Elvis, M., Risaliti, G., & Zamorani, G. 2002, ApJL, 565, L75

Fabian, A. C. 1999, MNRAS, 308, L39

Fabian, A. C., & Iwasawa, K. 1999, MNRAS, 303, L34

Fabjan, D., Borgani, S., Tornatore, L., et al. 2010, MNRAS, 401, 1670

Fanidakis, N., Baugh, C. M., Benson, A. J., et al. 2012, MNRAS, 419, 2797

Fathi, K., Storchi-Bergmann, T., Riffel, R. A., et al. 2006, ApJL, 641, L25

Federrath, C. 2013, MNRAS, 436, 1245

Federrath, C., & Klessen, R. S. 2012, ApJ, 761, 156

—. 2013, ApJ, 763, 51

Federrath, C., Roman-Duval, J., Klessen, R. S., Schmidt, W., & Mac Low, M.-M. 2010, A&A, 512, A81

Ferrarese, L., & Ford, H. 2005, Space Sci. Rev., 116, 523

Ferrarese, L., & Merritt, D. 2000, ApJL, 539, L9

Fleck, Jr., R. C. 1996, ApJ, 458, 739

Forman, W., Jones, C., Churazov, E., et al. 2007, ApJ, 665, 1057

Frank, J., King, A., & Raine, D. J. 2002, Accretion Power in Astrophysics: Third Edition

Frisch, U. 1995, Turbulence. The legacy of A. N. Kolmogorov.

Fruscione, A., Greenhill, L. J., Filippenko, A. V., et al. 2005, ApJ, 624, 103

Gallimore, J. F., Axon, D. J., O'Dea, C. P., Baum, S. A., & Pedlar, A. 2006, AJ, 132, 546

Galtier, S., & Banerjee, S. 2011, Physical Review Letters, 107, 134501

García-Burillo, S., Combes, F., Schinnerer, E., Boone, F., & Hunt, L. K. 2005, A&A, 441, 1011

Gaspari, M., Ruszkowski, M., & Oh, S. P. 2013, ArXiv e-prints

Gebhardt, K., Bender, R., Bower, G., et al. 2000, ApJL, 539, L13

Genzel, R., Eisenhauer, F., & Gillessen, S. 2010, Reviews of Modern Physics, 82, 3121

Genzel, R., Schödel, R., Ott, T., et al. 2003, ApJ, 594, 812

Ghez, A. M., Salim, S., Hornstein, S. D., et al. 2005, ApJ, 620, 744

Gingold, R. A., & Monaghan, J. J. 1977, MNRAS, 181, 375

Gofford, J., Reeves, J. N., Turner, T. J., et al. 2011, MNRAS, 414, 3307

Goldbaum, N. J., Krumholz, M. R., Matzner, C. D., & McKee, C. F. 2011, ApJ, 738, 101

González Delgado, R. M., Heckman, T., & Leitherer, C. 2001, ApJ, 546, 845

Goodman, J. 2003, MNRAS, 339, 937

Goulding, A. D., Alexander, D. M., Lehmer, B. D., & Mullaney, J. R. 2010, MNRAS, 406, 597

Graham, A. W. 2007, MNRAS, 379, 711

Green, A. W., Glazebrook, K., McGregor, P. J., et al. 2010, Nature, 467, 684

Greenhill, L. J., Booth, R. S., Ellingsen, S. P., et al. 2003, ApJ, 590, 162

Greenstein, J. L. 1963, Nature, 197, 1041

Greif, T. H., Johnson, J. L., Klessen, R. S., & Bromm, V. 2008, MNRAS, 387, 1021

Guainazzi, M., Matt, G., & Perola, G. C. 2005, A&A, 444, 119

Gültekin, K., Richstone, D. O., Gebhardt, K., et al. 2009, ApJ, 698, 198

Häring, N., & Rix, H.-W. 2004, ApJL, 604, L89

Hazard, C., Mackey, M. B., & Shimmins, A. J. 1963, Nature, 197, 1037

Heller, C., Shlosman, I., & Englmaier, P. 2001, ApJ, 553, 661

Hennebelle, P., & Chabrier, G. 2008, ApJ, 684, 395

—. 2011, ApJL, 743, L29

Henriksen, R. N. 1991, ApJ, 377, 500

Herrnstein, J. R., Moran, J. M., Greenhill, L. J., & Trotter, A. S. 2005, ApJ, 629, 719

Hicks, E. K. S., Davies, R. I., Maciejewski, W., et al. 2013, ApJ, 768, 107

Hirschmann, M., Dolag, K., Saro, A., et al. 2014, MNRAS, 442, 2304

Ho, L. 1999, in Astrophysics and Space Science Library, Vol. 234, Observational Evidence for the Black Holes in the Universe, ed. S. K. Chakrabarti, 157

Hobbs, A., & Nayakshin, S. 2009, MNRAS, 394, 191

Hobbs, A., Nayakshin, S., Power, C., & King, A. 2011, MNRAS, 413, 2633

Hobbs, A., Power, C., Nayakshin, S., & King, A. R. 2012, MNRAS, 421, 3443

Hoffmann, V., & Romeo, A. B. 2012, MNRAS, 425, 1511

Hopkins, P. F. 2013, MNRAS, 430, 1653

Hopkins, P. F., Cox, T. J., Kereš, D., & Hernquist, L. 2008, ApJS, 175, 390

Hopkins, P. F., Hernquist, L., Cox, T. J., et al. 2006a, ApJS, 163, 1

Hopkins, P. F., Hernquist, L., Cox, T. J., Robertson, B., & Krause, E. 2007a, ApJ, 669, 45

—. 2007b, ApJ, 669, 67

Hopkins, P. F., Hernquist, L., Hayward, C. C., & Narayanan, D. 2012, MNRAS, 425, 1121

Hopkins, P. F., Narayan, R., & Hernquist, L. 2006b, ApJ, 643, 641

Hopkins, P. F., & Quataert, E. 2010a, MNRAS, 407, 1529

—. 2010b, MNRAS, 405, L41

—. 2011, MNRAS, 415, 1027

Hunt, L. K., & Malkan, M. A. 2004, ApJ, 616, 707

Igumenshchev, I. V. 2006, ApJ, 649, 361

Jahnke, K., & Macciò, A. V. 2011, ApJ, 734, 92

Jeffreys, H. 1924, The earth: its origin, history and physical constitution (University Press)

Jogee, S. 2006, in Lecture Notes in Physics, Berlin Springer Verlag, Vol. 693, Physics of Active Galactic Nuclei at all Scales, ed. D. Alloin, 143

Jungwiert, B., Combes, F., & Palouš, J. 2001, A&A, 376, 85

Kainulainen, J., Federrath, C., & Henning, T. 2013, A&A, 553, L8

Kawakatu, N., & Wada, K. 2008, ApJ, 681, 73

Keel, W. C. 1980, AJ, 85, 198

King, A. 2003, ApJL, 596, L27

—. 2008, New Astro. Rev., 52, 253

King, A. R., & Pringle, J. E. 2006, MNRAS, 373, L90

—. 2007, MNRAS, 377, L25

King, A. R., Pringle, J. E., & Hofmann, J. A. 2008, MNRAS, 385, 1621

Kinney, A. L., Schmitt, H. R., Clarke, C. J., et al. 2000, ApJ, 537, 152

Kishimoto, M., Hönig, S. F., Antonucci, R., et al. 2011, A&A, 527, A121

Kitsionas, S., Federrath, C., Klessen, R. S., et al. 2009, A&A, 508, 541

Klessen, R. S., & Hennebelle, P. 2010, A&A, 520, A17

Knapen, J. H., Shlosman, I., & Peletier, R. F. 2000, ApJ, 529, 93

Kolmogorov, A. 1941, Akademiia Nauk SSSR Doklady, 30, 301

Kondratko, P. T., Greenhill, L. J., & Moran, J. M. 2005, ApJ, 618, 618

Kormendy, J. 1993, in The Nearest Active Galaxies, ed. J. Beckman, L. Colina, & H. Netzer, 197–218

Kormendy, J., & Gebhardt, K. 2001, in American Institute of Physics Conference Series, Vol. 586, 20th Texas Symposium on relativistic astrophysics, ed. J. C. Wheeler & H. Martel, 363–381

Kormendy, J., & Ho, L. C. 2013, ARA&A, 51, 511

Kormendy, J., & Richstone, D. 1995, ARA&A, 33, 581

Koss, M., Mushotzky, R., Veilleux, S., & Winter, L. 2010, ApJL, 716, L125

Kritsuk, A. G., Norman, M. L., Padoan, P., & Wagner, R. 2007, ApJ, 665, 416

Kritsuk, A. G., Ustyugov, S. D., Norman, M. L., & Padoan, P. 2009, in Astronomical Society of the Pacific Conference Series, Vol. 406, Numerical Modeling of Space Plasma Flows: ASTRONUM-2008, ed. N. V. Pogorelov, E. Audit, P. Colella, & G. P. Zank, 15

Krumholz, M. R., Matzner, C. D., & McKee, C. F. 2006a, ApJ, 653, 361

Krumholz, M. R., & McKee, C. F. 2005, ApJ, 630, 250

Krumholz, M. R., McKee, C. F., & Klein, R. I. 2005, ApJ, 618, 757

—. 2006b, ApJ, 638, 369

Kuo, C. Y., Braatz, J. A., Condon, J. J., et al. 2011, ApJ, 727, 20

Lada, C. J., Lombardi, M., & Alves, J. F. 2010, ApJ, 724, 687

Laine, S., Shlosman, I., Knapen, J. H., & Peletier, R. F. 2002, ApJ, 567, 97

Lapi, A., Raimundo, S., Aversa, R., et al. 2014, ApJ, 782, 69

Larson, R. B. 1981, MNRAS, 194, 809

Latif, M. A., Schleicher, D. R. G., Schmidt, W., & Niemeyer, J. 2013, MNRAS, 433, 1607

Lee, E. J., Murray, N., & Rahman, M. 2012, ApJ, 752, 146

Lesieur, M. 1997, Turbulence in Fluids, Fluid Mechanics and Its Applications (Springer)

Levin, Y. 2007, MNRAS, 374, 515

Levin, Y., & Beloborodov, A. M. 2003, ApJL, 590, L33

Levine, R., Gnedin, N. Y., & Hamilton, A. J. S. 2010, ApJ, 716, 1386

Li, J., Ostriker, J., & Sunyaev, R. 2013, ApJ, 767, 105

Lighthill, M. J. 1955, in IAU Symposium, Vol. 2, Gas Dynamics of Cosmic Clouds, 121

Lintott, C., Schawinski, K., Bamford, S., et al. 2011, MNRAS, 410, 166

Liu, X., Shen, Y., Strauss, M. A., & Hao, L. 2011, ApJ, 737, 101

Livio, M., Ogilvie, G. I., & Pringle, J. E. 1999, ApJ, 512, 100

Lobban, A. P., Reeves, J. N., Miller, L., et al. 2011, MNRAS, 414, 1965

Lodato, G. 2007, Nuovo Cimento Rivista Serie, 30, 293

—. 2012, Advances in Astronomy, 2012, 11

Lodato, G., & Price, D. J. 2010, MNRAS, 405, 1212

Lucas, W. E., Bonnell, I. A., Davies, M. B., & Rice, W. K. M. 2013, MNRAS, 433, 353

Lucy, L. B. 1977, AJ, 82, 1013

Lüst, R. 1952, Zeitschrift Naturforschung Teil A, 7, 87

Lynden-Bell, D. 1969, Nature, 223, 690

Mac Low, M.-M., & Klessen, R. S. 2004, Reviews of Modern Physics, 76, 125

Magorrian, J., Tremaine, S., Richstone, D., et al. 1998, AJ, 115, 2285

Malbon, R. K., Baugh, C. M., Frenk, C. S., & Lacey, C. G. 2007, MNRAS, 382, 1394

Marconi, A., & Hunt, L. K. 2003, ApJL, 589, L21

Marconi, A., Risaliti, G., Gilli, R., et al. 2004, MNRAS, 351, 169

Martini, P., Regan, M. W., Mulchaey, J. S., & Pogge, R. W. 2003, ApJ, 589, 774

Mathews, W. G., & Guo, F. 2012, ApJ, 754, 154

McConnell, N. J., & Ma, C.-P. 2013, ApJ, 764, 184

McKee, C. F. 1989, ApJ, 345, 782

McKee, C. F., & Ostriker, E. C. 2007, ARA&A, 45, 565

McLure, R. J., & Dunlop, J. S. 2002, MNRAS, 331, 795

Merloni, A. 2004, MNRAS, 353, 1035

Merloni, A., & Heinz, S. 2008, MNRAS, 388, 1011

Merloni, A., Heinz, S., & di Matteo, T. 2003, MNRAS, 345, 1057

Merloni, A., Bongiorno, A., Brusa, M., et al. 2014, MNRAS, 437, 3550

Merritt, D., & Ferrarese, L. 2001, MNRAS, 320, L30

Mihos, J. C., & Hernquist, L. 1996, ApJ, 464, 641

Miyoshi, M., Moran, J., Herrnstein, J., et al. 1995, Nature, 373, 127

Moderski, R., & Sikora, M. 1996, A&AS, 120, C591

Monaghan, J., & Gingold, R. 1983, Journal of Computational Physics, 52, 374

Monaghan, J. J. 1997, Journal of Computational Physics, 136, 298

Moraghan, A., Kim, J., & Yoon, S.-J. 2013, MNRAS, 432, L80

Morris, J. P., & Monaghan, J. J. 1997, Journal of Computational Physics, 136, 41

Mortlock, D. J., Warren, S. J., Venemans, B. P., et al. 2011, Nature, 474, 616

Mulchaey, J. S., Regan, M. W., & Kundu, A. 1997, ApJS, 110, 299

Mullaney, J. R., Alexander, D. M., Fine, S., et al. 2013, MNRAS, 433, 622

Narayan, R., & Fabian, A. C. 2011, MNRAS, 415, 3721

Natarajan, P., & Pringle, J. E. 1998, ApJL, 506, L97

Nayakshin, S. 2005, MNRAS, 359, 545

Nayakshin, S., & Cuadra, J. 2005, A&A, 437, 437

Nayakshin, S., Cuadra, J., & Springel, V. 2007, MNRAS, 379, 21

Nayakshin, S., Dehnen, W., Cuadra, J., & Genzel, R. 2006, MNRAS, 366, 1410

Nayakshin, S., & King, A. 2007, ArXiv e-prints

Nayakshin, S., & Sunyaev, R. 2005, MNRAS, 364, L23

Nayakshin, S., Wilkinson, M. I., & King, A. 2009, MNRAS, 398, L54

Nixon, C., King, A., Price, D., & Frank, J. 2012a, ApJL, 757, L24

Nixon, C. J., King, A. R., & Price, D. J. 2012b, MNRAS, 422, 2547

Norman, C., & Silk, J. 1980, ApJ, 238, 158

Oke, J. B. 1963, Nature, 197, 1040

Padoan, P., & Nordlund, Å. 2002, ApJ, 576, 870

—. 2011, ApJ, 730, 40

Panis, J.-F., & Pérault, M. 1998, Physics of Fluids, 10, 3111

Paumard, T., Genzel, R., Martins, F., et al. 2006, ApJ, 643, 1011

Peek, B. M. 1942, J. Brit. Astro. Assoc., 53, 23

Pen, U.-L., Matzner, C. D., & Wong, S. 2003, ApJL, 596, L207

Peng, C. Y. 2007, ApJ, 671, 1098

Piontek, R. A., & Ostriker, E. C. 2007, ApJ, 663, 183

Pizzolato, F., & Soker, N. 2010, MNRAS, 408, 961

Planelles, S., Borgani, S., Fabjan, D., et al. 2014, MNRAS, 438, 195

Pogge, R. W., & Martini, P. 2002, ApJ, 569, 624

Pope, E. C. D. 2011, MNRAS, 414, 3344

Porter, D., Pouquet, A., & Woodward, P. 1994, in Bulletin of the American Astronomical Society, Vol. 26, American Astronomical Society Meeting Abstracts #184, 928

Pounds, K. A., King, A. R., Page, K. L., & O'Brien, P. T. 2003, MNRAS, 346, 1025

Power, C., Nayakshin, S., & King, A. 2011, MNRAS, 412, 269

Prendergast, K. H., & Burbidge, G. R. 1968, ApJL, 151, L83

Price, D. J. 2007, Publ. Astron. Soc. Aust., 24, 159

—. 2012a, Journal of Computational Physics, 231, 759

—. 2012b, Journal of Computational Physics, 231, 759

Price, D. J., & Federrath, C. 2010a, MNRAS, 406, 1659

Price, D. J., & Federrath, C. 2010b, in Astronomical Society of the Pacific Conference Series, Vol. 429, Numerical Modeling of Space Plasma Flows, Astronum-2009, ed. N. V. Pogorelov, E. Audit, & G. P. Zank, 274

Pringle, J. E. 1981, ARA&A, 19, 137

Proga, D., & Begelman, M. C. 2003, ApJ, 592, 767

Quataert, E., & Narayan, R. 2000, ApJ, 528, 236

Raban, D., Jaffe, W., Röttgering, H., Meisenheimer, K., & Tristram, K. R. W. 2009, MNRAS, 394, 1325

Rafferty, D. A., McNamara, B. R., & Nulsen, P. E. J. 2008, ApJ, 687, 899

Ragone-Figueroa, C., Granato, G. L., Murante, G., Borgani, S., & Cui, W. 2013, MNRAS, 436, 1750

Raimundo, S. I., Davies, R. I., Gandhi, P., et al. 2013, MNRAS, 431, 2294

Raimundo, S. I., Fabian, A. C., Bauer, F. E., et al. 2010, MNRAS, 408, 1714

Rees, M. J. 1978, Physica Scripta, 17, 193

Reeves, J. N., O'Brien, P. T., & Ward, M. J. 2003, ApJL, 593, L65

Reynolds, O. 1883, Royal Society of London Philosophical Transactions Series I, 174, 935

Richardson, L. 1922, Weather Prediction by Numerical Process

Riffel, R. A., Storchi-Bergmann, T., Winge, C., et al. 2008, MNRAS, 385, 1129

Risaliti, G., Maiolino, R., & Salvati, M. 1999, ApJ, 522, 157

Rodríguez-Zaurín, J., Arribas, S., Monreal-Ibero, A., et al. 2011, A&A, 527, A60

Roman-Duval, J., Jackson, J. M., Heyer, M., Rathborne, J., & Simon, R. 2010, ApJ, 723, 492

Romeo, A. B., Burkert, A., & Agertz, O. 2010, MNRAS, 407, 1223

Rosswog, S. 2009, New Astro. Rev., 53, 78

Rosswog, S., & Brüggen, M. 2007, Introduction to High-Energy Astrophysics

Salpeter, E. E. 1964, ApJ, 140, 796

Salucci, P., Szuszkiewicz, E., Monaco, P., & Danese, L. 1999, MNRAS, 307, 637

Sandage, A. 1965, ApJ, 141, 1560

Sani, E., Marconi, A., Hunt, L. K., & Risaliti, G. 2011, MNRAS, 413, 1479

Sasao, T. 1973, PASJ, 25, 1

Scannapieco, C., Wadepuhl, M., Parry, O. H., et al. 2012, MNRAS, 423, 1726

Schartmann, M., Burkert, A., Krause, M., et al. 2010, MNRAS, 403, 1801

Schartmann, M., Meisenheimer, K., Klahr, H., et al. 2009, MNRAS, 393, 759

Schawinski, K., Dowlin, N., Thomas, D., Urry, C. M., & Edmondson, E. 2010, ApJL, 714, L108

Schawinski, K., Virani, S., Simmons, B., et al. 2009, ApJL, 692, L19

Scheuer, P. A. G. 1974, MNRAS, 166, 513

Schleicher, D. R. G., Banerjee, R., Sur, S., et al. 2010, A&A, 522, A115

Schmidt, M. 1963, Nature, 197, 1040

Schmitt, H. R., Kinney, A. L., Storchi-Bergmann, T., Antonucci, & Robert. 1997, ApJ, 477, 623

Schnorr Müller, A., Storchi-Bergmann, T., Riffel, R. A., et al. 2011, MNRAS, 413, 149

Schödel, R., Eckart, A., Alexander, T., et al. 2007, A&A, 469, 125

Schulze, A., & Wisotzki, L. 2010, A&A, 516, A87

Sesana, A., Barausse, E., Dotti, M., & Rossi, E. M. 2014, ApJ, 794, 104

Seyfert, C. K. 1943, ApJ, 97, 28

Shakura, N. I., & Sunyaev, R. A. 1973, A&A, 24, 337

Shankar, F., Salucci, P., Granato, G. L., De Zotti, G., & Danese, L. 2004, MNRAS, 354, 1020

Shankar, F., Weinberg, D. H., & Miralda-Escudé, J. 2009, ApJ, 690, 20

Shapiro, S. L., & Teukolsky, S. A. 1983, Black holes, white dwarfs, and neutron stars: The physics of compact objects

Shlosman, I., Begelman, M. C., & Frank, J. 1990, Nature, 345, 679

Shlosman, I., Frank, J., & Begelman, M. C. 1989, Nature, 338, 45

Silk, J., & Rees, M. J. 1998, A&A, 331, L1

Simões Lopes, R. D., Storchi-Bergmann, T., de Fátima Saraiva, M., & Martini, P. 2007, ApJ, 655, 718

Small, T. A., & Blandford, R. D. 1992, MNRAS, 259, 725

Smith, J. E., Robinson, A., Alexander, D. M., et al. 2004, MNRAS, 350, 140

Snyder, G. F., Hopkins, P. F., & Hernquist, L. 2011, ApJL, 728, L24

Soker, N. 2006, New Astro., 12, 38

Soltan, A. 1982, MNRAS, 200, 115

Somerville, R. S., Hopkins, P. F., Cox, T. J., Robertson, B. E., & Hernquist, L. 2008, MNRAS, 391, 481

Springel, V. 2005, MNRAS, 364, 1105

Springel, V., Di Matteo, T., & Hernquist, L. 2005a, MNRAS, 361, 776

Springel, V., & Hernquist, L. 2002, MNRAS, 333, 649

Springel, V., White, S. D. M., Jenkins, A., et al. 2005b, Nature, 435, 629

Steinborn, L. K., Dolag, K., Hirschmann, M., Prieto, M. A., & Remus, R.-S. 2015, MNRAS, 448, 1504

Stokes, G. G. 1851, Transactions of the Cambridge Philosophical Society, 9, 8

Stoklasová, I., Ferruit, P., Emsellem, E., et al. 2009, A&A, 500, 1287

Storchi-Bergmann, T., Dors, Jr., O. L., Riffel, R. A., et al. 2007, ApJ, 670, 959

Storchi-Bergmann, T., Lopes, R. D. S., McGregor, P. J., et al. 2010, MNRAS, 402, 819

Tamburro, D., Rix, H.-W., Leroy, A. K., et al. 2009, AJ, 137, 4424

Taylor, P., & Kobayashi, C. 2015, MNRAS, 448, 1835

Teyssier, R., Moore, B., Martizzi, D., Dubois, Y., & Mayer, L. 2011, MNRAS, 414, 195

Thompson, T. A., Quataert, E., & Murray, N. 2005, ApJ, 630, 167

Tombesi, F., Cappi, M., Reeves, J. N., et al. 2010, A&A, 521, A57

Toomre, A. 1964, ApJ, 139, 1217

Toro, E. 1997, Riemann Solvers and Numerical Methods for Fluid Dynamics: A Practical Introduction (Springer)

Tozzi, P., Gilli, R., Mainieri, V., et al. 2006, A&A, 451, 457

Tremaine, S., & Davis, S. W. 2014, MNRAS, 441, 1408

Tristram, K. R. W., Meisenheimer, K., Jaffe, W., et al. 2007, A&A, 474, 837

Tristram, K. R. W., Raban, D., Meisenheimer, K., et al. 2009, A&A, 502, 67

Tueller, J., Baumgartner, W. H., Markwardt, C. B., et al. 2010, ApJS, 186, 378

Ulvestad, J. S., & Wilson, A. S. 1984, ApJ, 285, 439

Valdarnini, R. 2011, A&A, 526, A158

Vázquez-Semadeni, E., Cantó, J., & Lizano, S. 1998, ApJ, 492, 596

Vogelsberger, M., Genel, S., Springel, V., et al. 2014, MNRAS, 444, 1518

Vollmer, B., Beckert, T., & Davies, R. I. 2008, A&A, 491, 441

Volonteri, M., Capelo, P. R., Netzer, H., et al. 2015, ArXiv e-prints

Volonteri, M., Madau, P., Quataert, E., & Rees, M. J. 2005, ApJ, 620, 69

Volonteri, M., & Rees, M. J. 2005, ApJ, 633, 624

von Weizsäcker, C. F. 1943, Zeits. Astrophys., 22, 319

—. 1948, Zeitschrift Naturforschung Teil A, 3, 524

—. 1951, ApJ, 114, 165

Vonneumann, J., & Richtmyer, R. D. 1950, Journal of Applied Physics, 21, 232

Wada, K., Papadopoulos, P. P., & Spaans, M. 2009, ApJ, 702, 63

Wild, V., Heckman, T., & Charlot, S. 2010, MNRAS, 405, 933

Willott, C. J., Rawlings, S., Blundell, K. M., & Lacy, M. 2000, MNRAS, 316, 449

Wise, J. H., Turk, M. J., & Abel, T. 2008, ApJ, 682, 745

Young, S. 2000, MNRAS, 312, 567

Young, S., Axon, D. J., Robinson, A., Hough, J. H., & Smith, J. E. 2007, Nature, 450, 74

Zel'dovich, Y. B. 1965, Soviet Astronomy, 9, 221

COLOPHON

This document was typeset using the typographical look-and-feel `classicthesis` developed by André Miede. The style was inspired by Robert Bringhurst's seminal book on typography "*The Elements of Typographic Style*". `classicthesis` is available for both LaTeX and LyX:

http://code.google.com/p/classicthesis/

Happy users of `classicthesis` usually send a real postcard to the author, a collection of postcards received so far is featured here:

http://postcards.miede.de/